ISSN 1997-308X
eISSN 2412-8767

ИЗВЕСТИЯ ВУЗОВ
ПОРОШКОВАЯ МЕТАЛЛУРГИЯ И ФУНКЦИОНАЛЬНЫЕ ПОКРЫТИЯ

POWDER METALLURGY AND FUNCTIONAL COATINGS

2023
Том / Vol. 17 № / No. 2
powder.misis.ru

ISSN 1997-308X
eISSN 2412-8767

POWDER METALLURGY AND FUNCTIONAL COATINGS

Scientific and Technical Journal
Founded in 2007
Four issues per year

2023
Vol. 17 No. 2
Том 17 № 2

ИЗВЕСТИЯ ВУЗОВ ПОРОШКОВАЯ МЕТАЛЛУРГИЯ И ФУНКЦИОНАЛЬНЫЕ ПОКРЫТИЯ

Научно-технический журнал
Основан в 2007 г.
Выходит 4 раза в год

POWDER METALLURGY AND FUNCTIONAL COATINGS

SCIENTIFIC AND TECHNICAL JOURNAL
FOUNDED IN 2007
FOUR ISSUES PER YEAR

http://powder.misis.ru

ISSN 1997-308X
eISSN 2412-8767

Founder: MISIS UNIVERSITY OF SCIENCE AND TECHNOLOGY

National University of Science and Technology "MISIS"
Address: 4 bld. 1 Leninskiy Prosp., Moscow 119049, Russian Federation
http://www.misis.ru

Editor-in-Chief

Evgeny A. Levashov
Prof., Dr. Sci. (Eng.), Acad. of the RANS, NUST MISIS, Moscow, Russian Federation

Journal is included into the List of peer-reviewed scientific publications recommended by the Highest Attestation Commission of the Ministry of Education and Science of the Russian Federation for publishing the results of doctoral and candidate dissertations.
Abstracting/Indexing: Scopus, Russian Science Citation Index (RSCI), Ulrich's Periodicals Directory, VINITI Database (Abstract Journal).

Editorial Board

M. I. Alymov – Dr. Sci. (Eng.), Corresponding Member of the RAS, Merzhanov Institute of Structural Macrokinetics and Materials Sciences of the RAS, Chernogolovka, Russia
A. P. Amosov – Prof., Dr. Sci. (Phys.-Math.), Samara State Technical University, Samara, Russia
G. A. Bagliuk – Prof., Dr. Sci. (Eng.), Acad. of the NASU, IPMS NASU, Kiev, Ukraine
I. V. Blinkov – Prof., Dr. Sci. (Eng.), NUST MISIS, Moscow, Russia
M. V. Chukin – Prof., Dr. Sci. (Eng.), Magnitogorsk State Technical University, Magnitogorsk, Russia
H. Danninger – Prof., Dr. Sci., Vienna University of Technology, Vienna, Austria
B. Derin – Assoc. Prof., Dr. Sci. (Phil.), Istanbul Technical University, Maslak, Istanbul, Turkey
V. Yu. Dorofeyev – Prof., Dr. Sci. (Eng.), South-Russian State Polytechnical University (NPI), Novocherkassk, Russia
Yu. Estrin – Prof., Dr. Sci. (Nat.), Monash University, Clayton, Australia
A. Ph. Ilyushchanka – Prof., Dr. Sci. (Eng.), Acad. of the NAS of Belarus, State Research and Production Powder Metallurgy Association, Minsk, Belarus
Yu. R. Kolobov – Prof., Dr. Sci. (Phys.-Math.), Federal Research Center of Problems of Chemical Pfysics and Medicinal Chemistry of the RAS, Chernogolovka, Russia
V. S. Komlev – Prof., Dr. Sci. (Eng.), Corresponding Member of the RAS, Institute of Metallurgy of the RAS, Moscow, Russia
I. Konyashin – Prof., Dr. Sci. (Econ.), Element Six GmbH, Burghaun, Germany
Yu. M. Korolyov – Prof., Dr. Sci. (Eng.), Scientific and Technical Association "Powder Metallurgy", Moscow, Russia
V. I. Kostikov – Prof., Dr. Sci. (Eng.), Corresp. Member of the RAS, NUST MISIS, Moscow, Russia
D. Yu. Kovalev – Dr. Sci. (Phys.-Math.), Merzhanov Institute of Structural Macrokinetics and Materials Sciences of the RAS, Chernogolovka, Russia
S. A. Kulinich – Assoc. Prof., PhD (Chem.), Tokai University, Hiratsuka, Kanagawa, Japan
S. V. Kuzmin – Prof., Dr. Sci. (Eng.), Corresponding Member of the RAS, Volgograd State Technical University, Volgograd, Russia
V. P. Kuznetsov – Prof., Dr. Sci. (Eng.), Ural Federal University, Ekaterinburg, Russia
Yu. V. Levinsky – Prof., Dr. Sci. (Eng.) Merzhanov Institute of Structural Macrokinetics and Materials Sciences of the RAS, Chernogolovka, Russia
A. E. Ligachyov – Prof., Dr. Sci. (Phys.-Math.), Prokhorov General Physics Institute of the RAS, Moscow, Russia
V. Yu. Lopatin – Cand. Sci., NUST MISIS, Moscow, Russia
A. A. Lozovan – Prof., Dr. Sci (Eng.), Moscow Aviation Institute (NRU), Moscow, Russia
V. I. Lysak – Prof., Dr. Sci. (Eng.), Acad. of the RAS, Volgograd State Technical University, Volgograd, Russia
A. V. Makarov – Dr. Sci. (Eng.), Corresponding Member of the RAS, M.N. Mikheev Institute of Metal Physics of the Ural Branch of the RAS, Ural Federal University, Ekaterinburg, Russia
L. L. Mishnaevsky – Dr. Habil. (Eng.), Technical University of Denmark, Roskilde, Denmark
A. S. Mukasyan – Prof., Dr. Sci. (Phys.-Math.), University of Notre Dame College of Engineering, Notre Dame, USA
S. A. Oglezneva – Prof., Dr. Sci. (Eng.), Perm National Research Polytechnical University, Perm, Russia
S. S. Ordanian – Prof., Dr. Sci. (Eng.), St. Petersburg State Technological Institute (Technical University), St. Petersburg, Russia
R. Orrù – Prof., Dr. Sci. (Eng.), University of Cagliari, Cagliari, Italy
I. B. Panteleev – Prof., Dr. Sci. (Eng.), St. Petersburg State Technological Institute (Technical University), St. Petersburg, Russia
F. Peizhong – Prof., Dr. Sci., China University of Mining and Technology, Xuzhou, P.R. China
C. Pengwan – Prof., Dr. Sci., Beijing Institute of Technology, Beijing, P.R. China
M. I. Petrzhik – Dr. Sci. (Eng.), NUST MISIS, Moscow, Russia
Yu. S. Pogozhev – Assoc. Prof., Cand. Sci. (Eng.), NUST MISIS, Moscow, Russia
V. V. Polyakov – Prof., Dr. Sci. (Phys.-Math.), Altai State University, Barnaul, Russia
A. A. Popovich – Prof., Dr. Sci. (Eng.)., Corresp. Member of the RANS, St. Petersburg State Polytechnical University (National Research University), St. Petersburg, Russia
S. E. Porozova – Dr. Sci. (Eng.), Perm National Research Polytechnical University, Perm, Russia
A. A. Rempel – Prof., Dr. Sci. (Eng.), Acad. of the RAS, Institute of Metallurgy of the Ural Branch of the RAS, Ekaterinburg, Russia
F. Rustichelli – Prof., Dr. Sci. (Phys.), University of Marches, Ancona, Italy
S. D. Shlyapin – Prof., Dr. Sci. (Eng.), Moscow Aviation Institute (NRU), Moscow, Russia
D. V. Shtansky – Dr. Sci. (Phys.-Math.), NUST MISIS, Moscow, Russia
P. A. Vityaz' – Prof., Dr. Sci. (Eng.), Acad. of the NAS of Belarus, Minsk, Belarus
A. A. Zaitsev – Assoc. Prof., Cand. Sci. (Eng.), NUST MISIS, Moscow, Russia
Zh. YongTing – Prof., Dr. Sci., Harbin Institute of Technology, Harbin, P.R. China
F. Zhengyi – Prof., Dr. Sci., Wuhan University of Technology, Wuhan, P.R. China

Editorial Staff

Address: NUST MISIS,
4 bld. 1 Leninskiy Prosp., Moscow 119049, Russian Federation

Phone: +7 (495) 638-45-35. *E-mail:* izv.vuz@misis.ru

Certificate of registration **No. FS77-27955** (12.04.2007)
Re-registration **PI No. FS77-79230** (25.09.2020)

PM & FC © NUST MISIS, Moscow, 2023

Articles are available under Creative Commons Attribution Non-Commercial No Derivatives

Leading Editor: O.V. Sosnina
Executive Editor: A.A. Kudinova
Layout Designer: V.V. Rasenets

Signed print 14.03.2023. Format 60×90 $^1/_8$
Offset paper No. 1. Digital printing. Quires 9.75
Order 17520. Free price
Printed in the printing house of the MISIS Publish House
4 bld. 1 Leninskiy Prosp., Moscow, 119049 Russian Federation
Phone/fax: +7 (499) 236-76-17

ИЗВЕСТИЯ ВУЗОВ ПОРОШКОВАЯ МЕТАЛЛУРГИЯ И ФУНКЦИОНАЛЬНЫЕ ПОКРЫТИЯ

Научно-технический журнал
Основан в 2007 г.
Выходит 4 раза в год

http://powder.misis.ru

ISSN 1997-308X
eISSN 2412-8767

Учредитель:

ФГАОУ ВО Национальный исследовательский технологический университет «МИСИС»
Адрес: 119049, Москва, Ленинский пр-т, 4, стр. 1
https://www.misis.ru

Главный редактор

Евгений Александрович Левашов
д.т.н., академик РАЕН, профессор, НИТУ МИСИС, г. Москва

Журнал включен в Перечень рецензируемых научных изданий, рекомендованных ВАК Минобрнауки РФ для публикации результатов диссертаций на соискание ученых степеней.
Журнал включен в базы данных: Scopus, Russian Science Citation Index (RSCI), Ulrich's Periodicals Directory, РИНЦ, БД/РЖ ВИНИТИ.

Редакционная коллегия

М. И. Алымов – д.т.н., чл.-корр. РАН, проф., ИСМАН, г. Черноголовка
А. П. Амосов – д.ф.-м.н., проф., СамГТУ, г. Самара
Г. А. Баглюк – д.т.н., акад. НАНУ, проф., ИПМ НАН Украины, г. Киев
И. В. Блинков – д.т.н., проф., НИТУ МИСИС, г. Москва
П. А. Витязь – д.т.н., акад. НАНБ, проф., НАН Беларуси, г. Минск
В. Ю. Дорофеев – д.т.н., проф., ЮРГПУ (НПИ), г. Новочеркасск
А. А. Зайцев – к.т.н., доц., НИТУ МИСИС, г. Москва
А. Ф. Ильющенко – д.т.н., акад. НАН Беларуси, проф., ГНПО ПМ НАН Беларуси, г. Минск
Д. Ю. Ковалев – д.ф.-м.н., ИСМАН, г. Черноголовка
Ю. Р. Колобов – д.ф.-м.н., проф., ФИЦ ПХФ и МХ РАН, г. Черноголовка
В. С. Комлев – д.т.н., чл.-корр. РАН, проф., ИМЕТ РАН, г. Москва
Ю. М. Королев – д.т.н., проф., НТА «Порошковая металлургия», г. Москва
В. И. Костиков – д.т.н., чл.-корр. РАН, проф., НИТУ МИСИС, г. Москва
В. П. Кузнецов – д.т.н., проф., УрФУ, г. Екатеринбург
С. В. Кузьмин – д.т.н., чл.-корр. РАН, проф., ВолгГТУ, г. Волгоград
Ю. В. Левинский – д.т.н., проф., ИСМАН, г. Черноголовка
А. Е. Лигачев – д.ф.-м.н., проф., ИОФ РАН, г. Москва
А. А. Лозован – д.т.н., проф., МАИ (НИУ), г. Москва
В. Ю. Лопатин – к.т.н., доц., НИТУ МИСИС, г. Москва
В. И. Лысак – д.т.н., акад. РАН, проф., ВолгГТУ, г. Волгоград
А. В. Макаров – д.т.н., чл.-корр. РАН, ИФМ УрО РАН, УрФУ, г. Екатеринбург
С. А. Оглезнева – д.т.н., проф., ПНИПУ, г. Пермь
С. С. Орданьян – д.т.н., проф., СПбГТИ (ТУ), г. Санкт-Петербург
И. Б. Пантелеев – д.т.н., проф., СПбГТИ (ТУ), г. Санкт-Петербург
М. И. Петржик – д.т.н., проф., НИТУ МИСИС, г. Москва
Ю. С. Погожев – к.т.н., доц., НИТУ МИСИС, г. Москва
В. В. Поляков – д.ф.-м.н., проф., АлтГУ, г. Барнаул
А. А. Попович – д.т.н., чл.-корр. РАЕН, проф., СПбГПУ, г. Санкт-Петербург
С. Е. Порозова – д.т.н., проф., ПНИПУ, г. Пермь
А. А. Ремпель – д.т.н., акад. РАН, проф., ИМЕТ УрО РАН, г. Екатеринбург
М. В. Чукин – д.т.н., проф., МГТУ, г. Магнитогорск
С. Д. Шляпин – д.т.н., проф., МАИ (НИУ), г. Москва
Д. В. Штанский – д.ф.-м.н., проф. НИТУ МИСИС, г. Москва
C. Pengwan – Dr. Sci., Prof., Beijing Institute of Technology, Beijing, P.R. China
H. Danninger – Dr. Sci., Prof., Vienna University of Technology, Vienna, Austria
B. Derin – Dr. Sci. (Phil.), Assoc. Prof., Istanbul Technical University, Maslak, Istanbul, Turkey
Yu. Estrin – Dr. Sci. (Nat.), Prof., Monash University, Clayton, Australia
F. Peizhong – Dr. Sci., Prof., China University of Mining and Technology, Xuzhou, P.R. China
F. Zhengyi – Dr. Sci., Prof., Wuhan University of Technology, Wuhan, P.R. China
I. Konyashin – Dr. Sci. (Econ.), Prof., Element Six GmbH, Burghaun, Germany
S. A. Kulinich – PhD (Chem.), Associate Prof., Tokai University, Hiratsuka, Kanagawa, Japan
L. L. Mishnaevsky – Dr. Habil. (Eng.), Technical University of Denmark, Roskilde, Denmark
A. S. Mukasyan – Dr. Sci. (Phys.-Math.), Prof., University of Notre Dame College of Engineering, Notre Dame, USA
R. Orrù – Dr. Sci. (Eng.), Prof., University of Cagliari, Cagliari, Italy
F. Rustichelli – Dr. Sci. (Phys.), Prof., University of Marches, Ancona, Italy
Zh. YongTing – Dr. Sci., Prof., Harbin Institute of Technology, Harbin, P.R. China

Редакция журнала

Адрес: 119049, Москва,
Ленинский пр-т, 4, стр. 1. НИТУ МИСИС

Тел.: +7 (495) 638-45-35. ***Эл. почта:*** izv.vuz@misis.ru

Свидетельство о регистрации № **ФС77-27955** от 12.04.2007 г.
Перерегистрация 25.09.2020 г. **ПИ № ФС77-79230**

Ведущий редактор: О.В. Соснина
Выпускающий редактор: А.А. Кудинова
Дизайн и верстка: В.В. Расенець

Подписано в печать 20.05.2023. Формат 60×90 $^1/_8$
Бум. офсетная № 1. Печать цифровая. Усл. печ. л. 9,75
Заказ 17520. Цена свободная
Отпечатано в типографии Издательского Дома МИСИС
119049, г. Москва, Ленинский пр-т, 4, стр. 1
Тел./факс: +7 (499) 236-76-17

ПМ и ФП ИЗВЕСТИЯ ВУЗОВ © НИТУ МИСИС, Москва, 2023

Статьи доступны под лицензией Creative Commons Attribution Non-Commercial No Derivatives

Contents

Theory and Processes of Formation and Sintering of Powder Materials

Korosteleva E.N., Knyazeva A.G., Anisimova M.A., Nikolaev I.O.
The impact of impurities on the Al–Fe–C system phase composition changes during sintering 5

Refractory, Ceramic and Composite Materials

Didenko A.A., Astapov A.N., Terentieva V.S.
Effects of alloying $ZrB_2(HfB_2)$–SiC with tantalum on the structure and resistance to high-temperature oxidation and ablation: A review 14

Gudyma T.S., Krutskii Yu.L., Maksimovskiy E.A., Cherkasova N.Yu., Lapekin N.I., Larina T.V.
Synthesis of B_4C–TiB_2 composition powder mixtures by carbidobor reduction using nanofibrous carbon for ceramic fabrication 35

Grigorov I.G., Zhilyaev V.A.
Core/rim microstructure of Ti(C, N) cermets with low nickel-molybdenum binder content 46

Nanostructured Materials and Functional Coatings

Shcherbakov I.N., Gasanov B.G.
Effect of modifiers on the structure formation and properties of nickel-phosphorus coatings applied to powder steels 53

Sytchenko A.D., Vakhrushev R.A., Kiryukhantsev-Korneev Ph.V.
Investigation of the tribological characteristics of Ta–Zr–Si–B–C–N coatings 62

Application of Powder Materials and Functional Coatings

Sosnin M.D., Shorstkii I.A.
The influence of magnetic fields on the strength of modified epoxy resin composites 71

Содержание

Теория и процессы формования и спекания порошковых материалов

Коростелева Е.Н., Князева А.Г., Анисимова М.А., Николаев И.О.
Роль примесей в изменении фазового состава в системе Al–Fe–C при спекании 5

Тугоплавкие, керамические и композиционные материалы

Диденко А.А., Астапов А.Н., Терентьева В.С.
Влияние легирования танталом на структуру и стойкость к высокотемпературному окислению и абляции композиций в системе $ZrB_2(HfB_2)$–SiC. Обзор 14

Гудыма Т.С., Крутский Ю.Л., Максимовский Е.А., Черкасова Н.Ю., Лапекин Н.И., Ларина Т.В.
Синтез композиционных порошковых смесей B_4C–TiB_2 методом карбидоборного восстановления с использованием нановолокнистого углерода для изготовления керамики 35

Григоров И.Г., Жиляев В.А.
Микроструктура ядро/обод в керметах Ti(C, N) при дефиците никель-молибденовой связки 46

Наноструктурированные материалы и функциональные покрытия

Щербаков И.Н., Гасанов Б.Г.
Влияние модификаторов на структурообразование и свойства никель-фосфорных покрытий, нанесенных на порошковые стали 53

Сытченко А.Д., Вахрушев Р.А., Кирюханцев-Корнеев Ф.В.
Исследование триботехнических характеристик покрытий Ta–Zr–Si–B–C–N 62

Применение порошковых материалов и функциональных покрытий

Соснин М.Д., Шорсткий И.А.
Исследование влияния магнитных воздействий на прочностные характеристики модифицированных эпоксидных композиционных материалов 71

Theory and Processes of Formation and Sintering of Powder Materials
Теория и процессы формования и спекания порошковых материалов

UDC 536.425 + 621.762

https://doi.org/10.17073/1997-308X-2023-2-5-13

Research article
Научная статья

The impact of impurities on the Al–Fe–C system phase composition changes during sintering

E. N. Korosteleva, A. G. Knyazeva ✉, M. A. Anisimova, I. O. Nikolaev

Institute of Strength Physics and Materials Science of the Siberian Branch of the Russian Academy of Sciences
2/4 Akademicheskii Prosp., Tomsk 634055, Russia

✉ anna-knyazeva@mail.ru

Abstract. Manufacturing waste can be not only recycled but also utilized as a source of chemical elements and as a component of powder materials. Steel swarf are a complex multicomponent material with a high iron content, while impurities such as carbon can affect the diffusion interaction in the chip and metal powder mixture. In this study, we investigate the diffusion interaction between aluminum and steel swarf using temperature-controlled vacuum sintering. We analyzed the resulting mixture's microstructure and phase composition, and observed that sintering creates a multiphase structure in which FeAl iron aluminide occupies at least 30 vol. %. Despite the high sintering temperature, we also observed residual aluminum and iron. Incomplete transformation may result form refractory products that inhibit diffusion or impurities that influence the magnitude and direction of the diffusion fluxes. To confirm the impurities' role in the diffusion interaction kinetics, we developed simulation models of the intermetallic phase growth for a flat and spherical particle embedded in aluminum. The model consider cross-diffusion fluxes in the emerging phase regions and possible effects of impurities on the concentration limit for the new phase's existence. We derived approximate analytical solutions to analyze the emerging phase growth trends under various model parameters.

Keywords: metal swarf, reaction sintering, diffusion interaction, intermetallide phase, tests, simulation

Acknowledgements: This study is supported by the Russian Science Foundation and the Tomsk Oblast Administration, Grant No. 22-13-20031, https://rscf.ru/project/22-13-20031/

For citation: Korosteleva E.N., Knyazeva A.G., Anisimova M.A., Nikolaev I.O. The impact of impurities on the Al–Fe–C system phase composition changes during sintering. *Powder Metallurgy and Functional Coatings*. 2023;17(2):5–13. https://doi.org/10.17073/1997-308X-2023-2-5-13

Роль примесей в изменении фазового состава в системе Al–Fe–C при спекании

Е. Н. Коростелева, А. Г. Князева ✉, М. А. Анисимова, И. О. Николаев

Институт физики прочности и материаловедения Сибирского отделения РАН
Россия, 634055, г. Томск, Академический пр-т, 2/46

✉ anna-knyazeva@mail.ru

Аннотация. Эффективное использование материальных ресурсов заставляет активнее обращать внимание на отходы производства с целью не только простой их утилизации, но и их использования в качестве источника некоторых элементов и как компонентов порошковых материалов. Стальная стружка – сложный многокомпонентный материал на основе железа. Наличие примеси, например углерода, может оказывать влияние на диффузионное взаимодействие смеси стружки с порошком другого металла. В данной работе рассмотрен один из возможных вариантов диффузионного взаимодействия алюминия и стальной стружки в условиях вакуумного спекания с регулируемым нагревом. После спекания был проведен микроанализ структуры и определен фазовый состав продуктов взаимодействия. Выявлено, что в процессе спекания формируется многофазная структура, в которой не менее 30 % объема занимает алюминид железа FeAl. Несмотря на достаточно высокие температуры, фиксируются остатки алюминия и железа. Среди причин неполного превращения могут быть тугоплавкие продукты взаимодействия, тормозящие диффузию, а также примеси, влияющие на величину и направленность диффузионных потоков. Для подтверждения важной роли примесей в кинетике диффузионного взаимодействия рассмотрены модельные задачи роста интерметаллидной фазы между частицей плоской или сферической формы с окружающим ее алюминием. Учитывается появление перекрестных диффузионных потоков в области растущей фазы и, возможно, влияние примеси на концентрационный предел существования новой фазы. Найдены приближенные аналитические решения, которые позволяют проанализировать динамику роста области, занимаемой растущей фазой, в зависимости от параметров модели.

Ключевые слова: металлическая стружка, реакционное спекание, диффузионное взаимодействие, интерметаллидная фаза, эксперимент, моделирование

Благодарности: Исследование выполнено при финансовой поддержке Российского научного фонда и субсидии администрации Томской области, грант № 22-13-20031, https://rscf.ru/project/22-13-20031/

Для цитирования: Коростелева Е.Н., Князева А.Г., Анисимова М.А., Николаев И.О. Роль примесей в изменении фазового состава в системе Al–Fe–C при спекании. *Известия вузов. Порошковая металлургия и функциональные покрытия*. 2023;17(2):5–13. https://doi.org/10.17073/1997-308X-2023-2-5-13

Introduction

Steels and other iron alloys remain the most widely used and cost-effective material in the manufacturing industry. Materials scientists design new and more efficient materials to replace conventional alloys, while also seeking ways to recycle and reuse retired products, components, and waste [1–4]. The largest source of manufacturing waste is generated by machining, which produces metal swarf [5; 6]. It should be noted that steel swarf are complex, multicomponent materials containing iron and carbon [7].

The swarf may also contain other alloying elements in varying concentrations. For example, lowest steel grades (e.g., steel 45 [ANSI analog: 1045]) contain 0.42 to 0.5 wt. % of carbon. Other most significant alloying elements are manganese (up to 0.8 %) and silicon (up to 0.37 %). The steel specification allows for the presence of chromium, copper, and nickel (up to 0.3 % each), as well as a low amount of phosphorus and sulfur (up to 0.035 %). Steel swarf are formed by the high-speed cutting of the metal workpiece resulting in an activated, highly defective structure of the chip surface [8].

Swarf are typically remelted, following cleaning to remove oxidation products and coolant [9], and then compacted into briquettes. However, steel swarf can be used as a component of powder mixtures with other elements [10]. Given that fragmented steel swarf contain multiple elements, understanding their diffusion interaction with other components of the mixture under heating is of interest. a better understanding of this process will contribute to the development of new materials and metal waste recycling technologies.

The objective of this study is to analyze the effects of impurities on the diffusion interaction between the components of the Al–Fe–C system.

Materials and methods

Aluminum was used as the primary component of our mixture, which interacted with fragmented steel swarf. The Al–Fe system has been extensively studied [11–16], and aluminum is utilized both as a matrix and as an alloying element. The Al–Fe phase diagram [17] reveals that aluminum has high solubility in α-Fe, forming large areas of solid solutions (up to 32 at. %). Its solubility in γ-Fe drops to 1.285 at. % at high temperatures. The solubility of iron in aluminum is very low, with a maximum of 0.03 at. % at the 654 °C eutectic temperature. The system produces five stable intermetallic compounds (Fe_3Al, FeAl, $FeAl_2$, Fe_2Al_5 и $FeAl_3$) and their temperature range for existence is 552 to 1170 °C.

We studied a mixture of fragmented steel swarf (75 wt. %) created by machining a steel 45 grade workpiece and the PA-4 aluminum powder (25 wt. %). The mixture was heated to 1000 °C in a vacuum furnace, and the phase composition of the powder was examined by analyzing the microstructure after sintering.

Figure 1 displays the surface of a steel chip fragment and its microstructure after sintering. Our analysis indicated that the carbon component concentration did not exceed 1.5 %. Jäger S. et al. [18] conducted a detailed investigation of steel chip sintering.

As aluminum was added to the steel swarf, intermetallic compound s were synthesized, resulting in a multiphase structure (Figure 2) in which at least 30 vol. % is occupied by the FeAl iron aluminide. Despite the exothermic nature of the Al and Fe interaction, residual Al (at least 15 vol. %), and Fe were discovered by XRD in the vacuum sintering products. This indicate that the reactions between Al and Fe (the base element of the steel 45 grade swarf) were not completed even at the sintering temperature of 1000 °C when Al was in liquid state.

In the contact area between interacting particles where diffusion interaction occurs, there are various factors that can affect the flux dynamics and completeness of phase transformations. These factors may include:

– refractory interaction products that inhibit diffusion;

– impurities that affect the magnitude and direction of the diffusion fluxes;

– structural imperfections that affect diffusion and reactions at the micro level.

Although the impurities may not directly contribute to the formation of new phases, they can significantly impact the kinetics of phase formation.

In order to confirm the impact of the impurities, we proposed a simulation model.

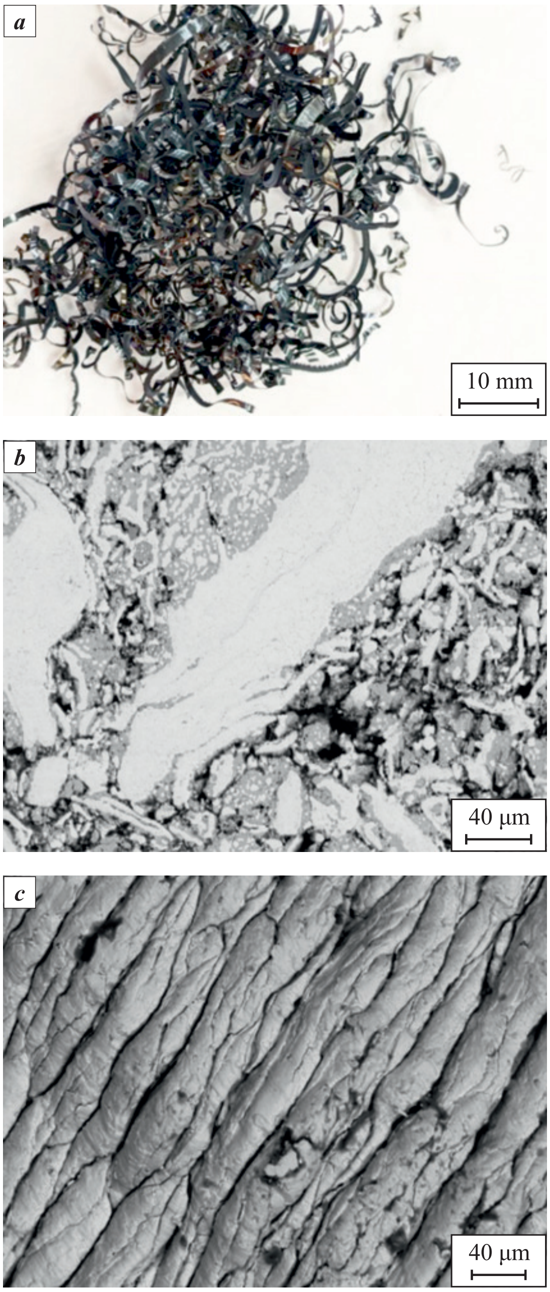

Fig. 1. Appearance (***a***) and surface morphology (***b***) of the steel 45 grade swarf. Chip microstructure after fragmenting and sintering at 1000 °C (***c***)

Рис. 1. Общий вид (***a***) и морфология поверхности (***b***) стальной стружки из стали 45, а также ее микроструктура после измельчения и спекания при 1000 °С (***c***)

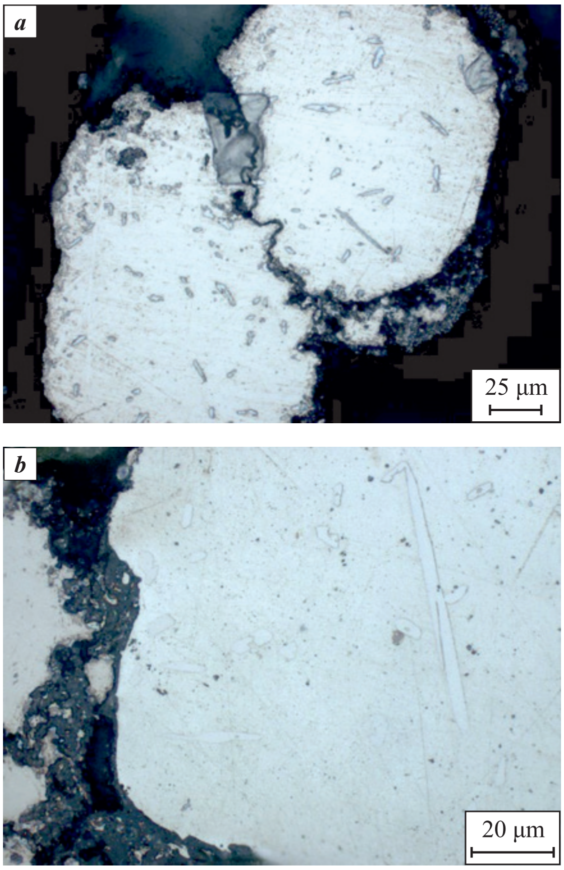

Fig. 2. Microstructure of the synthesized powders (25 % Al + 75 % steel 45)
a – appearance, ***b*** – intraparticle distribution of iron aluminide needle-like grains

Рис. 2. Микроструктура синтезированных порошковых продуктов состава 25 % Al + 75 % сталь 45
a – общий вид, ***b*** – внутричастичное распределение зерен-игл из алюминидов железа

Simulation model

The problem statement assumes that iron, as the primry component of the steel ships, has low solubility in Al. However, the solubility of aluminum in iron,although also limited, should be considered, with a value of 1.285 % at $t = 1150$ °C, which is the high-temperature solubility in γ-Fe. It is also assumed that each phase contains an area of homogeneity. Additionally, the steel swarf obtained by machining steel workpieces contain carbon as an impurity, with a maximum content of 1.5 %, accounting for possible contamination. It should be noted that the model for Fe and Al diffusion interaction in the presence of a third component can vary depending on the known diffusion path variations and higher phase competition in systems with more than two components [19; 20]. Cross-diffusion fluxes can result in an irregular concentration distribution in such systems [21–23].

1. The first version of the proposed model assumes a flat body for the chip, as shown in Fig. 1, *a*. Aluminum reacts with the iron at the surface, leading to the formation of intermetallic phases. Carbon influences diffusion by facilitating cross-diffusion fluxes. At any given moment, each phase may contain Fe, C, and Al. The model incorporates two moving boundaries, separating three regions that contain the three phases: (Fe + C)–(Fe_xAl_y)–(Al) (Figure 3). The intermetallic phases are located between the moving boundaries.

The sum of the three mass concentrations in each phase is always equal to 1 at any given point. Typically, two diffusion equations for each region are abequate:

$$\frac{\partial C_{1,k}}{\partial t}=\frac{\partial}{\partial x}\left(D_{11}^{(k)}\frac{\partial C_{1,k}}{\partial x}\right)+\frac{\partial}{\partial x}\left(D_{12}^{(k)}\frac{\partial C_{2,k}}{\partial x}\right), \qquad (1)$$

$$\frac{\partial C_{2,k}}{\partial t}=\frac{\partial}{\partial x}\left(D_{21}^{(k)}\frac{\partial C_{1,k}}{\partial x}\right)+\frac{\partial}{\partial x}\left(D_{22}^{(k)}\frac{\partial C_{2,k}}{\partial x}\right), \qquad (2)$$

where the k superscript can be p, ph, m and represent the Fe + C, Fe_xAl_y and Al(C, Fe) regions; $C_{1,k}$ is the iron concentration; $C_{2,k}$ is the carbon concentration in each region; $D_{ij}^{(k)}$ are the partial diffusion coefficients.

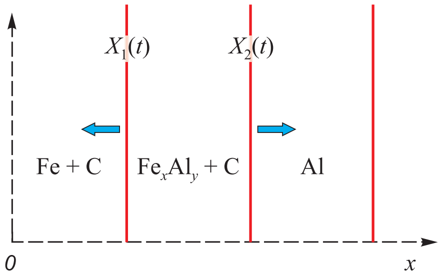

Fig. 3. Phase regions and moving boundaries

Рис. 3. Иллюстрация к математической постановке задачи

The symmetry condition is fulfilled at the center of the particle:

$$x=0:\frac{\partial C_{1,p}}{\partial x}=0;\ \ \frac{\partial C_{2,p}}{\partial x}=0. \qquad (3)$$

The conditions at the phase interfaces are as follows:

$$\begin{gathered}x=x_1(t):C_{1,p}=C_{10},\ C_{2,p}=C_{20},\ C_{1,ph}=\varphi_1,\\ C_{2,ph}=\gamma_1C_{2,p}\equiv\gamma_1C_{20},\\ \left(C_{1,p}-C_{1,ph}\right)\frac{dx_1}{dt}=-J_{1,ph}\ \text{ or }\ \left(C_{10}-\varphi_1\right)\frac{dx_1}{dt}=-J_{1,ph},\end{gathered} \qquad (4)$$

where C_{10}, C_{20} are the initial concentrations of iron and carbon, respectively, in the mixture particles; φ_1 is the iron solubility limit in the transition region containing Fe_3Al;

$$\begin{gathered}x=x_2(t):C_{1,ph}=\varphi_2,\ C_{1,m}=0,\\ \left(C_{1,ph}-C_{1,m}\right)\frac{dx_2}{dt}=J_{1,ph}\ \text{ or }\ \varphi_2\frac{dx_2}{dt}=J_{1,ph},\end{gathered} \qquad (5)$$

$$-D_{21}\frac{\partial C_{1,ph}}{\partial x}-D_{22}\frac{\partial C_{2,ph}}{\partial x}=-D_m\frac{\partial C_{2,m}}{\partial x}, \qquad (6)$$

$$C_{2,ph}\gamma_2=C_{2,m}, \qquad (7)$$

where φ_2 is the iron solubility limit in the transition region containing $FeAl_3$. It depends on the carbon concentration as follows:

$$\varphi_2=\varphi_{20}\left(1-\beta C_{2,ph}\right).$$

The impermeability condition applies to the outer boundary:

$$x=R_m:\frac{\partial C_{2,m}}{\partial x}=0. \qquad (8)$$

The equations for the diffusion fluxes in the region where a new phase emerges are given below

$$J_{1,ph}=-D_{11}\frac{\partial C_{1,ph}}{\partial x}-D_{12}\frac{\partial C_{2,ph}}{\partial x}, \qquad (9)$$

$$J_{2,ph}=-D_{21}\frac{\partial C_{1,ph}}{\partial x}-D_{22}\frac{\partial C_{2,ph}}{\partial x}. \qquad (10)$$

At the initial moment

$$\begin{gathered}t=0:C_{1,p}=C_{1,p0}=0.995,\ C_{2,p}=C_{2,p0}=0.005,\\ C_{1,m}=0,\ C_{2,m}=0,\ C_{1,ph}=0,\ C_{2,ph}=0,\\ x_1=x_{10}=R_0,\ x_2=x_{20}=R_0.\end{gathered}$$

Assuming the low solubility of aluminum in iron and iron in aluminum, we made an assumption that the concentrations of iron and carbon are constant in the Fe + C region i.e., to the left of the moving boundary $X_1(t)$, and only carbon is allowed to diffuse into the Al region to the right of $X_2(t)$. Therefore, the concentrations to the left of the $X_1(t)$ moving boundary can be expressed as

$$C_{1,p} = C_{1,p0}, \quad C_{2,p} = C_{2,p0}, \tag{11}$$

and to the right of $X_2(t)$

$$\frac{\partial C_{2,m}}{\partial t} = D_m \frac{\partial^2 C_{2,m}}{\partial x^2}. \tag{12}$$

Hereinafter, we omit the k superscript at the diffusion coefficients of the emerging phase.

To obtain an analytical solution, we used the quasi-static approximation and assume for equations (1), (2) and (12)

$$\frac{\partial C_{1,ph}}{\partial t} = 0, \quad \frac{\partial C_{2,ph}}{\partial t} = 0, \quad \frac{\partial C_{2,m}}{\partial t} = 0.$$

Then Eq. (1) and (2) take the form

$$\frac{d}{dx}\left(D_{11}\frac{dC_{1,ph}}{dx}\right) + \frac{d}{dx}\left(D_{12}\frac{dC_{2,ph}}{dx}\right) = 0,$$

$$\frac{d}{dx}\left(D_{21}\frac{dC_{1,ph}}{dx}\right) + \frac{d}{dx}\left(D_{22}\frac{dC_{2,ph}}{dx}\right) = 0.$$

These equations are equivalent to the following:

$$\frac{d}{dx}\left(\frac{dC_{1,ph}}{dx}\right) = 0, \quad \frac{d}{dx}\left(\frac{dC_{2,ph}}{dx}\right) = 0.$$

The solution is

$$C_{1,ph}(x) = A_1 x + B_1 \text{ и } C_{2,ph}(x) = A_2 x + B_2, \tag{13}$$

where A_1, A_2, B_1, B_2 are the integration constants.

By substituting Eq. (13) into the concentration boundary conditions, we obtained the following system of linear algebraic equations:

$$x = x_1(t): \varphi_1 = A_1 x_1 + B_1, \ \gamma_1 C_{20} = A_2 x_1 + B_2, \tag{14}$$

$$x = x_2(t): \left(\varphi_{20} - \varphi_{20}\beta_2\left[A_2 x_2 + B_2\right]\right) = A_1 x_2 + B_1, \tag{15}$$

$$D_{21} A_1 + D_{22} A_2 = 0. \tag{16}$$

The solution is:

$$A_1 = D_{22}\alpha\frac{1}{x_2 - x_1}, \ B_1 = \varphi_1 - D_{22}\alpha\frac{x_1}{x_2 - x_1},$$

$$A_2 = -D_{21}\alpha\frac{1}{x_2 - x_1}, \ B_2 = \gamma_1 C_{20} + D_{21}\alpha\frac{x_1}{x_2 - x_1},$$

where

$$\alpha = \frac{\varphi_1 - \varphi_{20}\left(1 - \beta\gamma_1 C_{20}\right)}{\varphi_{20}\beta D_{21} + D_{22}}. \tag{17}$$

Then flux equation (9) is

$$J_{1,ph} = -D_{11}A_1 - D_{12}A_2 = -\frac{\alpha\Delta}{x_2 - x_1}, \tag{18}$$

where $\Delta = D_{11}D_{22} - D_{12}D_{21}$.

Then we found the equations for the moving boundaries from diffusion flux conditions (4) and (5):

$$\left(C_{10} - \varphi_1\right)\frac{dx_1}{dt} = \frac{\alpha\Delta}{x_2 - x_1},$$
$$\varphi_{20}\left(1 - \beta C_{2,ph}\right)\frac{dx_2}{dt} = -\frac{\alpha\Delta}{x_2 - x_1}. \tag{19}$$

By substituting the integration constant expressions into (13), we obtained $C_{2,ph}$:

$$C_{2,ph}(x_2) = -D_{21}\alpha\frac{1}{x_2 - x_1}x_2 + \gamma_1 C_{20} + $$
$$+ D_{21}\alpha\frac{x_1}{x_2 - x_1} = \gamma_1 C_{20} - D_{21}\alpha.$$

It follows that

$$\varphi_{20}\left(1 - \beta\left[\gamma_1 C_{20} - D_{21}\alpha\right]\right)\frac{dx_2}{dt} = -\frac{\alpha\Delta}{x_2 - x_1}. \tag{20}$$

It follows from (19) and (20) that

$$\chi\frac{dx_1}{dx_2} = -1,$$

where $\chi = \dfrac{C_{10} - \varphi_1}{\varphi_{20}\left(1 - \beta\left[\gamma_1 C_{20} - D_{21}\alpha\right]\right)}$, therefore

$$x_2 = -\chi x_1 + F'. \tag{21}$$

At the initial moment, both boundaries are at R_0:

$$R_0 = -\chi R_0 + F',$$

then

$$F' = R_0(1 + \chi), \ x_2 = -\chi x_1 + R_0(1 + \chi),$$

$$\left(C_{10} - \varphi_1\right)\frac{dx_1}{dt} = \frac{\alpha\Delta}{\left(R_0 - x_1\right)\left(\chi + 1\right)}.$$

Therefore the equation for the x_1 boundary is

$$\frac{(x_1 - R_0)^2}{2} = -\frac{\alpha \Delta t}{(C_{10} - \varphi_1)(1+\chi)} + F'', \qquad (22)$$

where F'' is the integration constant. It follows from the initial conditions that $F'' = 0$.

The positions of the boundaries are governed by the parabolic law and are influenced by the cross-diffusion fluxes. These velocities vary due to the modifications in the homogeneity region of the intermetallic phase, as illustrated in Figure 4. It shows the boundary positions vs. time curves (top curves: x_2 boundary; bottom curves: x_1 boundary).

We assumed the following: $D_{11} = 3.63 \cdot 10^{-10}$, $D_{12} = 2.47 \cdot 10^{-12}$, $D_{22} = 3.32 \cdot 10^{-11}$, $D_{21} = 1.84 \cdot 10^{-12}$ m^2/s, $R_0 = 100$ µm.

Note that if there are cross fluxes only, it follows from (22) that

$$\frac{(x_1 - R_0)^2}{2} = -\frac{\varphi_1 - \varphi_{20}}{D_{22}} \varphi_{20} \frac{D_{11}D_{22} - D_{12}D_{21}}{(C_{10} - \varphi_1)(C_{10} - \varphi_1 + \varphi_{20})} t,$$

and if there are no impurities, then

$$\frac{(x_1 - R_0)^2}{2} = -\frac{D_{11}(\varphi_1 - \varphi_{20})\varphi_{20} t}{(C_{10} - \varphi_1)(C_{10} - \varphi_1 + \varphi_{20})}.$$

The presence of cross-diffusion fluxes can lead to both acceleration and deceleration of the boundary movement (faster or slower phase formation) depending on the sign of the $D_{12}D_{21}$ product. The expansion of the phase homogeneity region is always unidirectional. It means that the first option ($D_{12}D_{21} > 0$) is more likely observed in the tests.

If we consider the φ_1 vs. carbon concentration relationship, the solution is similar.

2. The second version of the model simulates spherical particles.

The diffusion equations for the transition layer in the spherical coordinate system take the form

$$\frac{\partial C_{1,ph}}{\partial t} = \frac{1}{r^2}\frac{\partial}{\partial r}\left(r^2 D_{11}\frac{\partial C_{1,ph}}{\partial r}\right) + \frac{1}{r^2}\frac{\partial}{\partial r}\left(r^2 D_{12}\frac{\partial C_{2,ph}}{\partial r}\right),$$

$$\frac{\partial C_{2,ph}}{\partial t} = \frac{1}{r^2}\frac{\partial}{\partial r}\left(r^2 D_{21}\frac{\partial C_{1,ph}}{\partial r}\right) + \frac{1}{r^2}\frac{\partial}{\partial r}\left(r^2 D_{22}\frac{\partial C_{2,ph}}{\partial r}\right),$$

where r is the radial coordinate.

A quasi-stationary approximation is

$$\frac{1}{r^2}\frac{d}{dr}\left(r^2 D_{11}\frac{dC_{1,ph}}{dr}\right) + \frac{1}{r^2}\frac{d}{dr}\left(r^2 D_{12}\frac{dC_{2,ph}}{dr}\right) = 0,$$

$$\frac{1}{r^2}\frac{d}{dr}\left(r^2 D_{21}\frac{dC_{1,ph}}{dr}\right) + \frac{1}{r^2}\frac{d}{dr}\left(r^2 D_{22}\frac{dC_{2,ph}}{dr}\right) = 0.$$

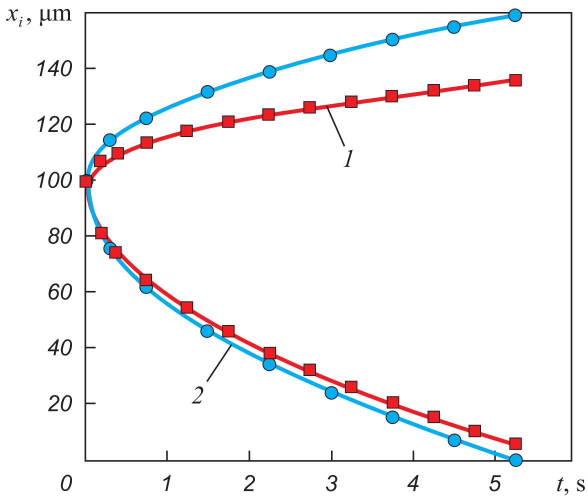

Fig. 4. Boundary positions vs. time curves (for flat particles)
1 – $\beta = 1$; ***2*** – $\beta = 10$ ($\gamma_1 = 1$)

Рис. 4. Положение границ в условиях плоской частицы
1 – $\beta = 1$; ***2*** – $\beta = 10$ ($\gamma_1 = 1$)

The boundary conditions and solution are similar to the previous case. The distribution of concentration is

$$C_{1,ph}(r) = -\frac{A_1}{r} + B_1, \; C_{2,ph}(r) = -\frac{A_2}{r} + B_2, \qquad (23)$$

where

$$\begin{aligned} A_1 &= -\alpha D_{22}\frac{x_1 x_2}{x_1 - x_2}, \; B_1 = -\alpha D_{22}\frac{x_2}{x_1 - x_2} + \varphi_1, \\ A_2 &= \alpha D_{21}\frac{x_1 x_2}{x_1 - x_2}, \; B_2 = \alpha D_{21}\frac{x_2}{x_1 - x_2} + \gamma_1 C_{20}. \end{aligned} \qquad (24)$$

The expression for the flux is similar to (9). By accounting for solutions (23), (24), it takes the form

$$\begin{aligned} J_{1,ph} &= -\left(D_{11}\frac{A_1}{r^2} + D_{12}\frac{A_2}{r^2}\right) = \\ &= -\frac{1}{r^2}\alpha\frac{x_1 x_2}{x_1 - x_2}(-D_{11}D_{22} + D_{12}D_{21}) = \\ &= \Delta\alpha\frac{x_1 x_2}{x_1 - x_2}\frac{1}{r^2}. \end{aligned} \qquad (25)$$

Consequently, we derived the equation for moving boundaries and the boundary ratio from the conditions similar to (4) and (5):

$$\chi \frac{dx_1}{dx_2} = -\frac{x_2^2}{x_1^2} \text{ and } x_2 = -\sqrt[3]{\chi} x_1 + F',$$

where

$$F' = R_0\left(1 + \sqrt[3]{\chi}\right),$$

$$\chi = \frac{C_{10} - \varphi_1}{\varphi_{20}\left(1 - \beta\left[\gamma_1 C_{20} - D_{21}\alpha\right]\right)}.$$

We again came to the parabolic law. It differs from the previous one only by the impact of its variables:

$$\frac{\left(R_0 - x_1\right)^2}{2} = -\frac{\alpha\Delta t}{\left(C_{10} - \varphi_1\right)\left(1 + \sqrt[3]{\chi}\right)}.$$

Figure 5 shows the difference in interphase velocities for particles of different shapes.

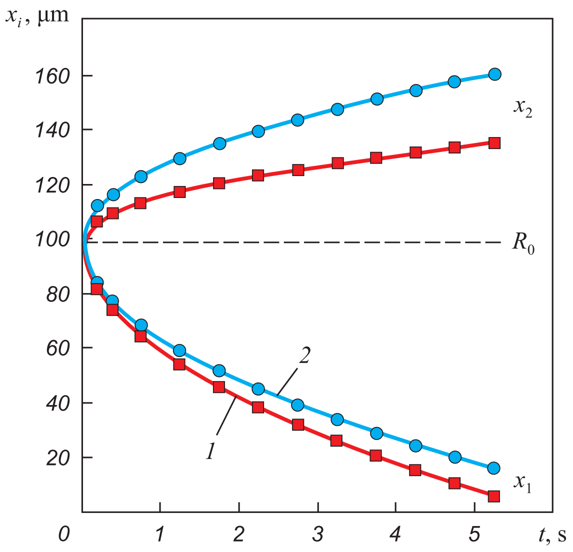

Fig. 5. Boundary position vs. time curves for flat (***1***) and spherical (***2***) particles. Assumptions:
$\gamma_1 = 1$, $\beta = 1$, $\varphi_1 = 0.85$, $\varphi_{20} = 0.4$,
$C_{10} = 0.995$, $C_{20} = 0.005$

Рис. 5. Изменение положения границ со временем для плоской (***1***) и сферической (***2***) частиц при следующих условиях:
$\gamma_1 = 1$, $\beta = 1$, $\varphi_1 = 0{,}85$, $\varphi_{20} = 0{,}4$,
$C_{10} = 0{,}995$, $C_{20} = 0{,}005$

Conclusions

The study revealed that the vacuum sintering of fragmented steel swarf with powdered aluminum does not achieve complete phase transformations, despite the exothermic nature of the intermetallic synthesis reaction. The initial phases were observed in the final product.

Our findings suggest that impurities in the swarf can affect the phase growth rate by inducing cross-diffusion fluxes and altering the size of the emerging phase homogeneity region. This effect was observed in both flat and spherical particles.

References / Список литературы

1. Rovin S.L., Kalinichenko A.S., Rovin L.E. The return of the dispersed metal waste into production. *Litiyo i metallurgiya*. 2019;(1):45–48. (In Russ.).
https://doi.org/10.21122/1683-6065-2019-1-45-48

Ровин С.Л., Калиниченко А.С., Ровин Л.Е. Возвращение дисперсных металлоотходов в производство. *Литье и металлургия*. 2019;(1):45–48.
https://doi.org/10.21122/1683-6065-2019-1-45-48

2. Chang J.I., Lin J.J., Huang J.S., Chang Y.M. Recycling oil and steel from grinding swarf. *Resources, Conservation and Recycling*. 2006;49(2):191–201.
https://doi.org/10.1016/j.resconrec.2006.03.014

3. Djakonov O.M. Production of metallurgical briquettes on the basis of chips-powder compositions by hot press molding. *Litiyo i metallurgiya*. 2011;(4):129–137. (In Russ.).

Дьяконов О.М. Получение металлургических брикетов на основе стружко-порошковых композиций горячим прессованием. *Литье и металлургия*. 2011;(4):129–137.

4. Andersson A., Gullberg A., Kullerstedt A., Sandberg E., Andersson M., Ahmed H., Sundqvist-Ökvist L., Björkman B. A holistic and experimentally-based view on recycling of off-gas dust within the integrated steel plant. *Metals*. 2018;8(10):760.
https://doi.org/10.3390/met8100760

5. Rovin S.L., Rovin L.E., Zayac T.M., Valickaya O.M. Recycling of ferrous metal shavings. *Litiyo i metallurgiya*. 2017;89(4):94–101. (In Russ.).
https://doi.org/10.21122/1683-6065-2017-4-94-101

Ровин С.Л., Ровин Л.Е., Заяц Т.М., Валицкая О.М. Переработка стружки черных металлов. *Литье и металлургия*. 2017;89(4):94–101.
https://doi.org/10.21122/1683-6065-2017-4-94-101

6. Hankel J., Jager S., Weber S. Development of a recycling strategy for grinding sludge using supersolidus liquid phase sintering. *Journal of Cleaner Production*. 2020;263:121501.
https://doi.org/10.1016/j.jclepro.2020.121501

7. Dyakonov O.M. Investigation of physicochemical and mechanical characteristics of steel and cast iron chips. *Litiyo i metallurgiya*. 2009;(4):161–173. (In Russ.).

Дьяконов О.М. Исследование физико-химических и механических свойств стальной и чугунной стружки. *Литье и металлургия*. 2009;(4):161–173.

8. Loginov Yu.N., Zagirov N.N., Ivanov E.V. Evaluation of the level of hardening of aluminum alloy chips intended for subsequent pressure treatment. *Obrabotka metallov (tekhnologiya, oborudovanie, instrumenty)*. 2021;23(1):45–55. (In Russ.).

Логинов Ю.Н., Загиров Н.Н., Иванов Е.В. Оценка уровня упрочнения стружки из алюминиевого сплава, предназначенной для последующей обработки давлением. *Обработка металлов (технология, оборудование, инструменты)*. 2021;23(1):45–55.

9. Mahmooda K., Ul Haq Syed W., Pinkerton A.J. Innovative reconsolidation of carbon steel machining swarf by laser metal deposition. *Optics and Lasers in Engineering*. 2011;49(2):240–247.
https://doi.org/10.1016/j.optlaseng.2010.09.014

10. Gnatko M., Li C., Arnold A., Freidrich B. Purification of aluminium cast alloy melts through precipitation of Fe-containing intermetallic compounds. *Metals*. 2018;8(10):796. https://doi.org/10.3390/met8100796

11. Shahid R.N., Scudino S. Strengthening of Al–Fe$_3$Al composites by the generation of harmonic structures. *Scientific Reports*. 2018;8:6484.
https://doi.org/10.1038/s41598-018-24824-y

12. Tomida S., Nakata K. Fe–Al composite layers on aluminum alloy formed by laser surface alloying with iron powder. *Surface and Coatings Technology*. 2003;174-175:559–563.
https://doi.org/10.1016/S0257-8972(03)00698-4

13. Minamino Y., Koizumi Y., Tsuji N., Hirohata N., Mizuuchi K., Ohkanda Y. Microstructures and mechanical properties of bulk nanocrystalline Fe–Al–C alloys made by mechanically alloying with subsequent spark plasma sintering. *Science and Technology of Advanced Materials*. 2004;5(1-2):133–143.
https://doi.org/10.1016/j.stam.2003.11.004

14. Najafi A., Movahedi M., Yarandi A.S. Properties–microstructure relationship in Al–Fe in situ composite produced by friction stir processing. *Proceedings of the Institution of Mechanical Engineers, Part L: Journal of Materials: Design and Applications*. 2019;233(10):1955–1965.
https://doi.org/10.1177/1464420718803752

15. Kopec M., Jóźwiak S., Kowalewski Z. Fe–Al based composite reinforced with ultra-fine Al$_2$O$_3$ oxides for high temperature applications. *Journal of Theoretical and Applied Mechanics*. 2021;59(3):509–513.
https://doi.org/10.15632/jtam-pl/138322

16. Kostov A., Friedrich B., Zivković D. Thermodynamic calculations in alloys Ti–Al, Ti–Fe, Al–Fe and Ti–Al–Fe. *Journal of Mining and Metallurgy, Section B: Metallurgy*. 2008;44(1):49–61.
https://doi.org/10.2298/JMMB0801049K

17. State Diagrams of Double Metal Systems: Handbook. In 3 vol. T. 1 / Ed. by N.P. Lyakishev. Moscow: Mashinostroenie, 1996. 991 p. (In Russ).

Диаграммы состояния двойных металлических систем: справочник. В 3 т. Т. 1 / Под ред. Н.П. Лякишева. М: Машиностроение, 1996. 991 с.

18. Jäger S., Weber S. Upcycling strategy of grinding swarf by super solidus liquid phase sintering. *Procedia CIRP*. 2020;90:546–551.
https://doi.org/10.1016/j.procir.2020.01.079

19. Wierzba B. Phase competition in ternary Ti–Ni–Al system. *Physica A: Statistical Mechanics and its Applications*. 2016;454:110–116.
https://doi.org/10.1016/j.physa.2016.02.068

20. Ji Y., Abernathy H.W., Chen L.-Q. Thermodynamic models of multicomponent nonstoichiometric solution phases using internal process order parameters. *Acta Materialia*. 2022;223:117462.
https://doi.org/10.1016/j.actamat.2021.117462

21. Knyazeva A.G. Difusion following the vacancy mechanism in materials with large number of internal surfaces. *Chemistry for Sustainable Development*. 2005;13(2):233–242.

22. Belova I.V., Murch G.E. Analysis of interdiffusion data in multicomponent alloys to extract fundamental diffusion information. *Journal of Phase Equilibria and Diffusion*. 2006;27(6): 629–637.
https://doi.org/10.1007/BF02736565

23. Svoboda J., Fischer F.D., Abart R. Modeling of diffusional phase transformation in multi-component systems with stoichiometric phases. *Acta Materialia*. 2010;58(8):2905–2911. https://doi.org/10.1016/j.actamat.2010.01.019

Information about the Authors

Elena N. Korosteleva – Cand. Sci. (Eng.), Senior Research Scientist, Institute of Strength Physics and Materials Science of the Siberian Branch of the Russian Academy of Sciences (ISPMS SB RAS)
ORCID: 0000-0002-4363-3604
E-mail: elenak@ispms.ru

Anna G. Knyazeva – Dr. Sci. (Phys.-Math.), Professor, Chief Research Scientist, ISPMS SB RAS
ORCID: 0000-0002-9765-7695
E-mail: anna-knyazeva@mail.ru

Maria A. Anisimova – Cand. Sci. (Phys.-Math.), Junior Research Scientist, ISPMS SB RAS
ORCID: 0000-0002-5312-2496
E-mail: anmariia@ispms.ru

Ivan O. Nikolaev – Engineer, ISPMS SB RAS
ORCID: 0000-0003-4529-6477
E-mail: rmkast97@gmail.com

Сведения об авторах

Елена Николаевна Коростелева – к.т.н., ст. науч. сотрудник, Институт физики прочности и материаловедения Сибирского отделения РАН (ИФПМ СО РАН)
ORCID: 0000-0002-4363-3604
E-mail: elenak@ispms.ru

Анна Георгиевна Князева – д.ф.-м.н., проф., гл. науч. сотрудник ИФПМ СО РАН
ORCID: 0000-0002-9765-7695
E-mail: anna-knyazeva@mail.ru

Мария Александровна Анисимова – к.ф.-м.н., мл. науч. сотрудник ИФПМ СО РАН
ORCID: 0000-0002-5312-2496
E-mail: anmariia@ispms.ru

Иван Олегович Николаев – инженер ИФПМ СО РАН
ORCID: 0000-0003-4529-6477
E-mail: rmkast97@gmail.com

Contribution of the Authors

E. N. Korosteleva – goal and objectives of the study, conducting the experiments, analysis of the research results, correction of the text, formulation of the conclusions.
A. G. Knyazeva – model formulation, analytical solutions, analysis of the research results, writing the text, correction of the conclusions.
M. A. Anisimova – conducting the calculations, preparation of illustrations.
I. O. Nikolaev – preparation and management of the experiments, conducting the experiments.

Вклад авторов

Е. Н. Коростелева – постановка цели и задачи исследования, проведение экспериментов, анализ результатов исследований, корректировка текста, формулировка выводов.
А. Г Князева – формулировка моделей, построение аналитических решений, анализ результатов исследований, подготовка текста статьи, корректировка выводов.
М. А. Анисимова – проведение расчетов, подготовка иллюстраций.
И. О. Николаев – подготовка эксперимента, проведение экспериментов.

Received 25.11.2022
Revised 02.12.2022
Accepted 05.12.2022

Статья поступила 25.11.2022 г.
Доработана 02.12.2022 г.
Принята к публикации 05.12.2022 г.

UDC 55.09.35 + 55.22.23

https://doi.org/10.17073/1997-308X-2023-2-14-34

Research article
Научная статья

Effects of alloying $ZrB_2(HfB_2)$–SiC with tantalum on the structure and resistance to high-temperature oxidation and ablation: A review

A. A. Didenko, A. N. Astapov, V. S. Terentieva

Moscow Aviation Institute (National Research University)
4 Volokolamskoe Shosse, Moscow 125993, Russia

lexxa1985@inbox.ru

Abstract. This review presents a comprehensive analysis of the impact of tantalum alloying on the structure, heat resistance, and ablation resistance of $ZrB_2(HfB_2)$–SiC ultra-high-temperature composites. The influence of the primary phase content on the effects on the structural and morphological features of the oxide layers and their protective efficiency is analyzed. It is shown that alloying positively affects the composite's behavior by enhancing the viscosity and thermal stability of the glass phase, decreasing anionic conductivity, partially stabilizing the $ZrO_2(HfO_2)$ lattice, and forming temperature-resistant complex oxides, such as $Zr_{11}Ta_4O_{32}$ or $Hf_6Ta_2O_{17}$ on the surface. It has been established that the alloying can have negative effects, including an increase in the liquid phase content, oxide film discontinuity, $ZrO_2(HfO_2)$ grain damage due to TaB_2 oxidation, or a significant amount of gas release due to TaC oxidation, as well as the formation of oxygen diffusion channels during the verticalization of $Zr_{11}Ta_4O_{32}$ or $Hf_6Ta_2O_{17}$ platelets. It is essential to note that the oxidation and ablation resistance, as well as the mechanisms driving composite behavior, differ depending on the alloying compounds and test conditions. Overall, this study sheds light on the role of tantalum alloying in enhancing the performance of $ZrB_2(HfB_2)$–SiC UHTC and highlights the importance of understanding the underlying mechanisms that govern their behavior.

Keywords: ultrahigh-temperature ceramics (UHTC), heat resistance, oxidation, ablation resistance, oxide film, borosilicate glass, tantalum, alloying

Acknowledgements: This study is supported by the Russian Science Foundation grant No. 22-29-01476, https://rscf.ru/project/22-29-01476/.

For citation: Didenko A.A., Astapov A.N., Terentieva V.S. Effects of alloying $ZrB_2(HfB_2)$–SiC with tantalum on the structure and resistance to high-temperature oxidation and ablation: A review. *Powder Metallurgy and Functional Coatings*. 2023;17(2):14–34. https://doi.org/10.17073/1997-308X-2023-2-14-34

Влияние легирования танталом на структуру и стойкость к высокотемпературному окислению и абляции композиций в системе $ZrB_2(HfB_2)$–SiC. Обзор

А. А. Диденко, А. Н. Астапов, В. С. Терентьева

Московский авиационный институт (национальный исследовательский университет)
Россия, 125993, г. Москва, Волоколамское шоссе, 4

lexxa1985@inbox.ru

Аннотация. Обзор посвящен изучению состояния вопроса в области влияния легирования соединениями тантала на эволюцию структуры, жаростойкость и стойкость к абляции ультравысокотемпературных композиций на основе системы $ZrB_2(HfB_2)$–SiC. Проанализировано влияние содержания первичных фаз на структурно-морфологические особенности образующихся оксидных слоев и эффективность их защитного действия. Показано, что положительный эффект от легирования прежде всего связан с увеличением вязкости и термической устойчивости формирующейся стеклофазы, снижением анионной проводимости, частичной стабилизацией решетки $ZrO_2(HfO_2)$ и образованием на поверхности температуроустойчивых комплексных оксидов типа $Zr_{11}Ta_4O_{32}$ или $Hf_6Ta_2O_{17}$. Установлено, что основными причинами отрицательного влияния легирования являются увеличение доли жидкой фазы, снижение сплошности структуры оксидной пленки в результате повреждения зерен $ZrO_2(HfO_2)$ при окислении TaB_2 или образования значительного количества газов при окислении TaC, а также появление дополнительных каналов для диффузии кислорода при вертикализации плоских частиц $Zr_{11}Ta_4O_{32}$ или $Hf_6Ta_2O_{17}$. Отмечено, что характеристики стойкости к окислению и абляции, а также механизмы, определяющие поведение композиций, неодинаковы для разных легирующих добавок и условий испытаний.

Ключевые слова: ультравысокотемпературная керамика (УВТК), жаростойкость, окисление, стойкость к абляции, оксидная пленка, боросиликатное стекло, тантал, модифицирование

Благодарности: Исследование выполнено за счет гранта Российского научного фонда № 22-29-01476, https://rscf.ru/project/22-29-01476/.

Для цитирования: Диденко А.А., Астапов А.Н., Терентьева В.С. Влияние легирования танталом на структуру и стойкость к высокотемпературному окислению и абляции композиций в системе $ZrB_2(HfB_2)$–SiC. Обзор. *Известия вузов. Порошковая металлургия и функциональные покрытия*. 2023;17(2):14–34.
https://doi.org/10.17073/1997-308X-2023-2-14-34

Introduction

Ultra-high-temperature ceramics (UHTC) and composites have been intensively studied as materials suitable for operating under extreme conditions [1–6]. Searching for effective compositions that ensure the operability of products made of them is an urgent problem of modern materials science. Zirconium and hafnium UHTCs have excellent thermomechanical properties, high melting points, and good oxidation resistance when alloyed with SiC. They can operate under extreme temperatures (>2000 °C) and in monatomic-oxygen-rich environments [4; 5]. The heterogeneous structure with a refractory crystal oxide matrix and viscous borosilicate glass make this materials extremely heat resistant. Many studies have found that such a structure efficiently withstands the exposure to high-speed, high-enthalpy flows so such materials are the mainstream now [7].

However, work on the modification of $ZrB_2(HfB_2)$––SiC UHTCs is ongoing and there are several reasons for this. In the crystal lattice of refractory ZrO_2 or HfO_2 oxides during oxidation under conditions of oxygen's low partial pressure, as well as when modified with lower valence cations (for example, Y^{3+}, La^{3+}), oxygen vacancies are formed, providing rapid anion transfer through the oxide film [8]. Another problem is ZrO_2 and HfO_2 polymorphism: at high temperatures, the oxides have a tetragonal or cubic lattice, which transforms into a monoclinic lattice upon cooling, leading to volumetric expansion. This phase transformation, combined with the high coefficient of thermal expansion and low thermal conductivity of the oxides can easily lead to cracking and delamination, especially under thermal cycling loads [8].

To solve this problems, the oxide film can be alloyed with higher valence cations, such as Ta^{5+} or Nb^{5+}. It results in an excess of anions in the lattice and increases film adhesion due to phase stabilization. In addition, the immiscibility of Ta_2O_5 or Nb_2O_5 oxides and borosilicate glass causes phase separation in the surface layer [8], which contributes to the higher viscosity and thermal stability of the glass. Alloying with tantalum is preferable, since the partial pressures of vapors over Ta_2O_5 are significantly lower when compared to Nb_2O_5 at high and ultra-high temperatures. Tantalum can be added in the form of a pure element, boride, silicide, or carbide. Some properties of these substances are listed in Table 1.

This review aims to analyze the available studies of tantalum alloying effects on the structure and behavior of materials based on $ZrB_2(HfB_2)$–SiC in the oxidizing atmosphere, as well as to identify the mechanisms of their impact on the oxidation and ablation resistance. We considered various types of materials:

Table 1. **Ta composition properties [9–14]**

Таблица 1. **Свойства Ta-содержащих соединений [9–14]**

Property	Ta	TaB_2	TaB	$TaSi_2$	Ta_5Si_3	TaC
Density, g/cm^3	16.40–16.65	11.20–12.62	14.00–14.29	8.80–9.14	12.50–13.06	14.30–14.80
Melting point, °C	2996–3020	3037–3200	2040–3090	2040–2299	2499–2550	3800–3880
Thermal expansion coefficient, 10^{-6}/K	6.3–6.6	8.2–8.8	–	7.4–8.5	–	6.64–8.4
Specific heat capacity, J/(kg·K)	140.00	237.55	246.85	–	–	190.00
Thermal conductivity, W/(m·K)	57.5	10.9–16.0	–	37.0	–	22.2

bulk UHTC, heat-resistant UHTC coatings on graphite and carbon-carbon composites, and carbon-ceramic composites with a UHTC matrix.

1. Bulk tantalum-alloyed $ZrB_2(HfB_2)$–SiC ultrahigh-temperature ceramics

In oxidizing environments, the structure of zirconium and hafnium diboride UHTCs alloyed with SiC becomes layered, including a continuous glass layer, a sublayer of the ZrO_2 and HfO_2 refractory oxides containing heat-resistant particles $ZrSiO_4$ and $HfSiO_4$, respectively, a layer of ZrB_2 and HfB_2 depleted in SiC, and a layer of unreacted ceramic [15–17]. Temperatures above the silicon dioxide melting point (1723 °C [18]) intensify the evaporation and mechanical removal of the glass by the high-speed flows [19], so the purpose of alloying with tantalum compounds is mostly connected with an increase in the UHTC oxidation and ablation resistance. Most studies do confirm the positive effects of Ta alloying. However, the results are inconsistent and are highly dependent on the test conditions.

1.1. Tantalum borides effects on ZrB_2–SiC structure and oxidation resistance

The Ta–B system has five intermediate phases: TaB_2, Ta_3B_4, TaB, Ta_2B, and Ta_3B. Only TaB and TaB_2 are stable in the room temperature to melting point range [14] and can be used as UHTC alloying components. Talmy I. et al. [20] reported that alloying the ZrB_2–SiC ceramics with tantalum diboride (10 mol. %) significantly increases its oxidation resistance at 1300 °C. The oxide film on the TaB_2 containing samples was less than a half of that on the reference UHTC samples. It was also found that adding even 2 mol. % TaB_2 results in a significant oxidation resistance growth when the sample is heated in a furnace at $t = 1200 \div 1400$ °C for 2 h. The morphology of the resulting heterogeneous surface layer indicates the spinodal decomposition of the SiO_2–Ta_2O_5 phases [20]. However, at $t = 1500$ °C no pronounced positive effect of TaB_2 additions on the ZrB_2–SiC heat resistance was observed. This may be associated with exceeding the miscibility limit of the multicomponent SiO_2–Ta_2O_5–ZrO_2 oxide system.

Lee S. et al. [15] studied the effects of adding tantalum to the ZrB_2–SiC system and the oxidation resistance of the $(Zr_{0.7}Ta_{0.3})B_2$ ceramic composite containing 30 vol. % SiC at temperatures up to 1500 °C and low partial oxygen pressure (~10^{-8} Pa). The weight gain of the Ta-containing samples, mostly attributed to the oxidation of ZrB_2 and TaB_2 to ZrO_2 and Ta_2O_5 occurs starting at 1000 °C, which is above the oxidation start temperature in UHTCs without Ta (800 °C). Lee S. et al. attributed the higher oxidation resistance in the material alloyed with TaB_2 over the entire temperature range primarily to the formation of a less porous oxide sublayer under the SiO_2-containing film. This was explained by the high viscosity of the liquid phase in the SiO_2–Ta_2O_5 system which is less susceptible to upwelling to the amorphous surface layer [15; 21]. Also, they observed a decrease in the $(Zr_{0.7}Ta_{0.3})B_2$ particle size, higher modulus of elasticity, hardness, and fracture toughness of the UHTC.

Peng F. et al. [22] studied the oxidation resistance of ZrB_2–B_4C–SiC–TaB_2 containing B_4C as a sintering additive [21] in the $1200 \div 1500$ °C temperature range. Increasing the TaB_2 concentration from 3.32 to 16.61 mol. % results in slightly better heat resistance at $t = 1200$ and 1400 °C. At $t = 1500$ °C, small

(3.32 mol. %) amounts of TaB_2 also improve the oxidation resistance [22]. Alloying with TaB_2 reduces the thickness of the oxide sublayers, but has no significant effect on the thickness of the amorphous surface layer. The researchers explained the higher heat resistance by the better sealing of oxide sublayers as their microstructure branches, since dispersed TaC particles are formed (it is a thermodynamically possible product of TaB_2 and SiC oxidation) [22] and also due to a larger surface wetted by the liquid phase. This contributes to reduced upwelling of the glass phase into the surface layer [23]. The higher TaB_2 concentration decreases the oxidation resistance at $t = 1500$ °C (and accelerates the weight gain after 60 and 120 min for 16.61 and 13.29 mol. % TaB_2 concentrations, respectively) [22], due to easier dissolution and deposition of zirconium dioxide in the glass surface layer [20].

The oxidation of ZrB_2–B_4C–SiC–TaB_2 containing 3.32 mol. % TaB_2 was also studied in the 1500–1900 °C temperature range [23]. The samples after oxidation feature thinner oxide passivation layers compared to TaB_2-free samples, and have a high oxidation resistance.

The effect of TaB monoboride on the oxidation of ZrB_2–SiC UHTC was also investigated at $t = 1800$ °C [24]. Ta adding greatly influences oxidation resistance, due to the evolution of the oxide film structure and the oxygen transport pathway during exposure. However, the effect on the UHTC oxidation resistance is significantly different from that at lower temperatures. For instance, ceramics alloyed with TaB show the lowest heat resistance at $t = 1800$ °C among CrB_2, HfB_2 and TaB alloying compounds [24].

1.2. Structure and oxidation resistance of $ZrB_2(HfB_2)$–SiC with tantalum carbides additions

Tantalum carbide has one of the highest melting points and can also be used as an additive [25], thus increasing the oxidation resistance of ZrB_2–SiC and HfB_2–SiC ceramic materials. However, Opila E. et al. [26] discovered that adding 20 vol. % TaC to ZrB_2–SiC does not increase the heat resistance. The TaC-containing samples at $t = 1627$ °C form a non-gastight film, presumably due to the porous microstructure formed by the CO and/or CO_2 release during oxidation.

The oxidation patterns of ZrB_2–SiC–TaC samples with different TaC contents (10 and 30 vol. %) in the $t = 1200{\div}1500$ °C temperature range indicate [27] that low TaC concentrations accelerate the oxidation, when compared to ZrB_2–SiC (the oxidation rate at $t = 1500$ °C increases 8-fold). Still, high TaC concentrations significantly improve the resistance to oxidation in air. For example, a sample containing 30 vol. % TaC showed an oxidation rate half as high as that of the initial ceramics under the same conditions. The surface of oxidized UHTCs containing TaC features multilayer oxide films including [27]:

1) a thin top layer of silicon dioxide;

2) a layer containing a mixture of the ZrO_2–SiO_2–Ta_2O_5 (10 vol. % TaC) and ZrO_2–SiO_2–$ZrSiO_4$ (30 vol. % TaC) phases;

3) a layer with a high Ta_2O_5 content.

It should be noted that these layers are porous in UHTCs with low TaC concentrations (in contrast to the samples with high TaC concentrations, where all the three oxide layers are very dense), and the oxide film thickness after oxidation at $t = 1500$ °C for 10 h is 850 μm (vs. 140 μm for ZrB_2–SiC–30 vol. % TaC and 440 μm for ZrB_2–SiC).

Re-oxidation of the same samples at $t = 1500$ °C showed that the oxidation may be caused not only by the inward diffusion of oxygen. For instance, cations diffusing from ceramics into the oxides, according to Wang Y. et al. [27] are also initially involved in mass transfer. The oxidation of ZrB_2–SiC–10 vol. % TaC is governed by the outward diffusion of tantalum resulting in the rapid formation of a porous structure, while the oxidation of ZrB_2–SiC–30 vol. % TaC is governed by the outward diffusion of silicon resulting in the formation of a dense SiO_2 layer and a significant share of the $ZrSiO_4$ heat-resistant phase.

The ZrB_2–20 vol. % SiC material with 5 vol. % TaC [28] also has a multilayer structure after oxidation at $t = 1400$ °C. The four layers that reacted with oxygen were observed:

1) a thin top layer of silicon dioxide containing Ta_2O_5;

2) a layer containing the ZrO_2, $ZrSiO_4$ and SiO_2 phases;

3) a layer enriched in ZrO_2 and depleted in SiC;

4) a ZrB_2-depleted layer containing SiO_2 and Ta_2O_5.

The oxide film on a similar material oxidized at $t = 1700$ °C contains the ZrO_2, Ta_2O_5, SiO_2 and $ZrSiO_4$ phases [28]. It follows that all the UHTC components including the initial ZrB_2, SiC and TaC, as well as the *in situ* formed ZrC and $TaSi_2$ phases, are oxidized under a high-temperature exposure.

Simonenko E. et al. [29] proposed adding the Ta_4HfC_5 complex carbide to HfB_2–SiC (5, 10, 15 vol. %), in order to prevent the HfB_2 grain growth, which improves the mechanical properties of the ceramics (note Ta_4HfC_5 is a nanodisperse phase). The thermogravimetric analysis of the ceramics samples when heated in air flow to 1400 °C showed that the increase of Ta_4HfC_5 content leads to the increase of the sample weight gain due to oxidation. The materials are more sensitive to oxygen than HfB_2–SiC, that can be explained by the high reactivity of the Ta_4HfC_5 ultra-heat-resistant nanocrystalline carbides and significant porosity. The microstructure of the oxidized sample surface depends on the Ta_4HfC_5 content. The UHTC containing 15 vol. % of the complex carbide is most noticeable: the silicon monoxide fibers on the borosilicate glass surface are self-organized into regular, hierarchical 3D nanostructures.

Simonenko E. et al. [30] exposed HfB_2–30 vol. % SiC–10 vol. % Ta_4HfC_5 to a high-enthalpy air jet for 2000 s under conditions of a gradual increase in the plasm generator anode power from 30 to 70 kW, and the heat flux from 363 to 779 W/cm^2. A distinctive feature of the ceramics under heating is a decrease of the surface radiative equilibrium temperature relative to the HfB_2–30 vol. % SiC reference material under identical test conditions. As the authors proposed, it is associated with the higher thermal conductivity of the ceramics alloyed with the Ta_4HfC_5 nanodisperse carbide. The tantalum oxide formed by Ta_4HfC_5 oxidation is a part of the silicate glass [30] and involved in the creation of the $Hf_6Ta_2O_{17}$ orthorhombic complex oxide which has phase stability up to the peritectic transformation point at t ~2250 °C [31]. The lower evaporation rate from the glassy layer surface is attributed to the lower surface temperature and lower vapor pressure over the SiO_2–Ta_2O_5 melt (the total vapor pressure at $t = 1827$ °C over SiO_2 (mostly SiO) and Ta_2O_5 (TaO_2 and TaO) is $9.48 \cdot 10^{-5}$ and $7 \cdot 10^{-7}$ atm, respectively [30]). As the surface temperature reached 1750÷1850 °C, even for the max heat flux, no “temperature jump” characteristic $HfB_2(ZrB_2)$–SiC [32] was observed.

1.3. Effects of tantalum silicides on $ZrB_2(HfB_2)$–SiC structure and oxidation resistance

Tantalum silicides are highly refractory (the melting point exceeds 2000 °C [9; 11]), can be used as sintering additives [33–35] and an additional source of silicon [36; 37], in order to facilitate the formation of protective silicate glass layers of the UHTC surface. Peng F. et al. [21] reported that adding 6.6 mol. % $TaSi_2$ to ZrB_2–B_4C–SiC resulted in higher oxidation resistance in the 1200÷1400 °C temperature range compared with TaB_2. The reason is that the formation of a protective surface glass layer with phase separation is facilitated by both Ta and extra Si, the oxidation of which increases the amount of the liquid phase and changes its composition. However, at $t = 1500$ °C the tantalum disilicide produces an opposite effect: TaSi concentration increase above 3.32 mol. % results in lower heat resistance, although the decrease is not as significant as the one caused by the TaB_2 content increase. Nevertheless, at low concentrations (3.3 mol. %) TaB_2 is more efficient compared to $TaSi_2$ at $t = 1500$ °C [22], and the lowest weight gain was observed in a mixture of TaB_2 and $TaSi_2$ (3.4 and 3.3 mol. %, respectively) over the entire temperature range [21].

The addition of $TaSi_2$ significantly improved the relative density, thermal shock resistance, and antioxidant properties of ZrB_2–SiC at $t = 1000÷1600$ °C [38]. The specific gravity variation over the entire thermal shock temperature range for the $TaSi_2$-containing samples was significantly less than that of the original samples: at $t = 1600$ °C the weight of ZrB_2–5 wt. % SiC–15 wt. % $TaSi_2$ changed by 0.68 %, whereas the weight of ZrB_2–5 wt. % SiC, by 1.6 %. The weight variation decreases as the $TaSi_2$ content increases [38].

Opila E. et al. [39] discovered that adding 5 vol. % $TaSi_2$ to ZrB_2–20 vol. % SiC was not sufficient to induce phase separation in the glass and improve the oxidation resistance in stagnant air at $t = 1627$ °C. On the other hand, the composition containing 20 vol. % $TaSi_2$ has better oxidation resistance compared to the original material. The oxide film thickness on the ZrB_2–20 vol. % SiC–20 vol. % $TaSi_2$ sample decreased about 10-fold when compared to the reference ceramics, and the surface appearance indicated the immiscibility of the glass phases [8; 26]. Under more extreme conditions (holding for 50 min in stagnant air at $t = 1927$ °C), the ceramics containing 20 vol. % $TaSi_2$ showed lower heat resistance compared to the non-alloyed material, as a result of forming a significant amount of the liquid phase [26]. Attempts to reduce its amount by reducing the $TaSi_2$ content to 5 vol. % were unsuccessful. The amount of liquid phase dropped compared to ZrB_2–20 vol. % SiC–20 vol. % $TaSi_2$, but its share was still substantial [39]. The $TaSi_2$ applications at $t = 1927$ °C are limited for several reasons:

1) $TaSi_2$ is unstable in the matrix with respect to ZrB_2;

2) $TaSi_2$ oxidizes intensively in the presence of SiC producing TaC and gaseous SiO which makes gaps in the substrate;

3) During the oxidation, 1.3 at. % or less of tantalum dissolves in ZrO_2, i.e. *in situ* alloying of zirconium dioxide to reduce the rate of oxygen transfer through it is limited;

4) The oxidation forms oxiboride, silicate, and zirconate phases, which leads to the formation of a large amount of liquid phase, and poor oxidation resistance.

Julian-Jankowiak A. et al. [40] also observed an increase of the ZrB_2–20 vol. % SiC–20 vol. % $TaSi_2$ oxidation resistance to 1900 °C and its decrease at higher temperatures (the heat resistance was studied at $t = 1200 \div 2300$ °C in air and water vapor).

With regard to hafnium diboride-based ceramics, the oxidation resistance of HfB_2–20 vol. % SiC in air at $t = 1627$ °C deteriorated after adding 20 vol. % $TaSi_2$ [26]. Monteverde F. et al. [35] obtained similar results for HfB_2–30 vol. % SiC–2 vol. % $TaSi_2$ produced by hot pressing (HP) and spark plasma sintering (SPS): the material heat resistance in air deteriorated in the $t = 1450 \div 1650$ °C range compared to $TaSi_2$-free materials. The microstructure of the oxidized samples was characterized by the presence of a layered oxide film, which thickness increased with temperature [35].

1.4. Metallic tantalum use to control ZrB_2–SiC structure and oxidation resistance

Tantalum in the form of a metal additive is also of interest, since it can be used to reduce sintering temperature, increase density, and improve the machinability, mechanical, and thermal properties of ZrB_2–SiC [41–43]. Thimmappa S. et al. [44; 45] showed that ZrB_2–20 vol. % SiC (2.5–10.0) wt. % Ta contains ZrB_2 cores in (Zr, Ta)B_2 shells, and also contains SiC, ZrO_2 and (Zr, Ta)C phases at the interfaces between the ZrB_2 grains. It was shown that tantalum dissolves in the ZrB_2 matrix, thus building a shell from the solid solution phase [41]. Hu C. et al. [33], Silvestroni L. et al. [37] and Yang Y. et al. [46] observed similar structures. The alloying with tantalum has a positive effect on the heat resistance of ZrB_2–20 vol. % SiC samples [44]. As the Ta content increases, the specific gravity and thickness of the oxide layer after isothermal oxidation at $t = 1500$ °C for 10 h in the air decreases from 22.91 to 18.77 mg/cm^2 and from 401 to 195 μm, respectively. Thimmappa S. et al. [45] observed a similar trend at $t = 1600$ °C (refer to Table 2).

The cross-section microstructure of the ZrB_2––SiC–Ta samples oxidized at $t = 1500$ and 1600 °C consists of three layers:

1) a thick, dense outer SiO_2 layer;

2) an intermediate ZrO_2 sublayer;

3) a ZrB_2 layer, depleted in SiC.

After oxidation, the material contains the ZrO_2, $Zr_{2.75}TaO_8$ crystalline phases, and the SiO_2 amorphous silica [44; 45]. The $Zr_{2.75}TaO_8$ phase formation is thermodynamically feasible at $t = 1500$ °C, and the phase content increases with the Ta concentration resulting in a higher viscosity of the glass phase and higher oxidation resistance [45]. As the Ta content increases, the thickness of the SiC-depleted layer decreases, and this can be attributed to the effects of the SiO_2-based, tantalum-modified top passivation layer [45].

It is assumed that the SiC-depleted layer reduces the overall oxidation resistance of ZrB_2 ceramic materials. However, no defects were found on the surface of ZrB_2–20 vol. % SiC–10 wt. % Ta with a SiC-depleted layer formed by isothermal oxidation at $t = 1600$ °C for 10 h in air. The UHTC showed comparable weight gain, and a significantly lower oxygen penetration depth (255 vs. 476 μm) than ZrB_2–20 vol. % SiC–10 vol. % Si_3N_4 without such a layer [41]. In general, ZrB_2–SiC–Ta ceramics have favorable strength at elevated temperatures [45] and heat resistance due to the protective nature of the formed oxide film. These UHTCs are suitable for high-temperature applications [41].

Table 2. **Oxidation resistance of $ZrB_2(HfB_2)$–SiC alloyed with Ta and Ta compounds**

Таблица 2. **Характеристики окислительной стойкости керамик на основе $ZrB_2(HfB_2)$–SiC, модифицированных танталом и его соединениями**

Composition, vol. %	Manufacturing process	Oxidation properties			Phase composition after oxidation	Reaction layer thickness, μm	Weight change, mg/cm^2	Reference
		t, °C	Time, min	Test conditions				
ZrB_2–20SiC + 2.5 wt. % Ta	SPS (1900 °C, 50 MPa, 3 min)	1500	600	Furnace, stagnant air	SiO_2, ZrO_2, $Zr_{2.75}TaO_8$	401	22.91	[44]
		1600				320	21.04	[45]
ZrB_2–5.6B_4C–27.9SiC + 3.3 mol. % $TaSi_2$	Sintering (2000 °C, Ar, 1 h) HIP (1800 °C, 207 MPa, 30 min)	1500	240	TGA, air (0.1 l/min)	*m,o*-ZrO_2, TaC	~9	~7.9	[22]
ZrB_2–5.6B_4C–27.9SiC + 3.3 mol. % TaB_2						~24	~5.7	
ZrB_2–5.6B_4C–27.9SiC + 3.3 mol. % TaB_2	Sintering (2100 °C, Ar, 1 h) HIP (1800 °C, 207 MPa, 30 min)	1600	75	TGA, air (0.1 l/min)	$Zr_xTa_{1-x}B_2$, ZrC(traces)	~166	~5.9	[23]
		1700	90			~395	~6.8	
		1800	85			~416	~11	
		1900	85			–	~15	
ZrB_2–25SiC + 5 mol. % TaB_2	HP (2100 °C, 20 MPa, 30 min)	1400	120	Furnace, stagnant air	–	–	~4.6	[20]
ZrB_2–20SiC–5TaC	HP (1850 °C, 40 MPa, 60 min)	1400	600	Furnace, stagnant air	SiO_2, Ta_2O_5, ZrO_2, $ZrSiO_4$	~65	–	[28]
ZrB_2–20SiC + 5 wt. % Ta	SPS (1900 °C, 50 MPa, 3 min)	1500	600	Furnace, stagnant air	SiO_2, ZrO_2, $Zr_{2.75}TaO_8$	384	19.15	[44]
		1600				303	17.45	[45]
ZrB_2–20SiC–5$TaSi_2$	HP (1750 °C, 69 MPa, 2 h)	1627	100	Bottom-loading furnace, stagnant air	*m,c*-ZrO_2	–	~5.1	[39]
ZrB_2–5.6B_4C–27.9SiC + 6.6 mol. % TaB_2	Sintering (2000 °C, Ar, 1 h) HIP (1800 °C, 207 MPa, 30 min)	1460	–	TGA, air (0.1 l/min)	ZrB_2–TaB_2(ss), ZrO_2, TaC, TaO (следы)	~25	~2.6	[21]
ZrB_2–5.6B_4C–28SiC + 6.7 mol. % $TaSi_2$						–	~1.0	
ZrB_2–5.6B_4C–27.9SiC + 6.7 mol. % TaB_2	Sintering (2000 °C, Ar, 1 h) HIP (1800 °C, 207 MPa, 30 min)	1500	240	TGA, air (0.1 l/min)	*m,o*-ZrO_2, TaC	~42	~13.2	[22]
ZrB_2–5.6B_4C–27.9SiC + 6.7 mol. % $TaSi_2$					*m,o*-ZrO_2, TaC, ZrB_2–TaB_2(ss)	~10.7	~8.1	
ZrB_2–5.6B_4C–27.9SiC + 10 mol. % TaB_2					*m,o*-ZrO_2, TaC	~45	~17.5	
ZrB_2–5.6B_4C–27.9SiC + 10 mol. % $TaSi_2$					*m,o*-ZrO_2, TaC, ZrB_2-TaB_2(ss)	~13	~10	

Table 2. **Oxidation resistance of $ZrB_2(HfB_2)$–SiC alloyed with Ta and Ta compounds** (*Continuation*)

Таблица 2. **Характеристики окислительной стойкости керамик на основе $ZrB_2(HfB_2)$–SiC, модифицированных танталом и его соединениями** (*продолжение*)

Composition, vol. %	Manufacturing process	Oxidation properties			Phase composition after oxidation	Reaction layer thickness, µm	Weight change, mg/cm^2	Reference
		t, °C	Time, min	Test conditions				
ZrB_2–25SiC + 10 mol. % TaB_2	HP (2100 °C, 20 MPa, 30 min)	1400	300	TGA, Ar/O_2 mixture (125 cm^3/min)	ZrO_2, $Zr_{2.75}TaO_8$	~50	–	[20]
ZrB_2–20SiC + 10 wt. % Ta	SPS (1900 °C, 50 MPa, 3 min)	1500	600	Furnace, stagnant air	SiO_2, ZrO_2, $Zr_{2.75}TaO_8$	195	18.77	[44]
ZrB_2–20SiC–10TaC	HP (1800 °C, 28 MPa, 1 h)	1500	600	Furnace, heating/cooling: Ar, oxidation: air (10 ml/min)	ZrO_2, Ta_2O_5	850	~58	[27]
ZrB_2–20SiC + 10 wt. % Ta	SPS (1900 °C, 50 MPa, 3 min)	1600	600	Furnace, stagnant air	SiO_2, ZrO_2, $Zr_{2.75}TaO_8$	255	16.65	[41; 45]
ZrB_2–20SiC–10TaB	HP (2000 °C, 30 MPa, 1 h)	1800	60	Bottom-loading furnace, stagnant air	–	–	~68	[24]
ZrB_2–5.6B_4C–27.9SiC + 13.3 mol. % TaB_2	Sintering (2000 °C, Ar, 1 h) HIP (1800 °C, 207 MPa, 30 min)	1460	–	TGA, air (0.1 l/min)	ZrB_2–TaB_2(ss), ZrO_2, TaC	–	~0.9	[21]
ZrB_2–5.6B_4C–27.9SiC + 13.3 mol. % TaB_2		1500	240		*m,o*-ZrO_2, TaC, TaB_2	~67	~23.1	[22]
ZrB_2–5.6B_4C–27.9SiC + 13.3 mol. % $TaSi_2$						~12.5	~11.6	
ZrB_2–5SiC + 15 wt. % $TaSi_2$	SPS (1700 °C, 50 MPa, 10 min)	1600	–	Thermal shock test	ZrB_2, ZrO_2, Zr–Ta–B, Zr–Ta–O	–	0.68%	[38]
ZrB_2–20SiC–20TaC	HP (2000 °C, 69 MPa, 2 h)	1627	100	Bottom-loading furnace, stagnant air	*t,m*-ZrO_2	–	~21	[26]
ZrB_2–20SiC–20$TaSi_2$	HP (1600 °C, 69 MPa, 2 h)	1627	100	Bottom-loading furnace, stagnant air	*m,c*-ZrO_2, SiO_2	–	~0,8	[8; 26]
$(Zr_{0.7}Ta_{0.3})B_2$–30SiC	HP (1800 °C, Ar, 32 MPa, 2 h)	1500	60	Furnace, CO and 2000 ppm CO_2 mixture (~10^{-8} Pa)	–	10.1±1.2	–	[15]
			600		–	72.3±2.8	–	
			300	TGA, air	–	–	~0.3	
ZrB_2–20SiC–30TaC	HP (1800 °C, 28 MPa, 1 h)	1500	600	Furnace, heating/cooling: Ar, oxidation: air (10 ml/min)	$ZrSiO_4$, Ta_2O_5, ZrO_2, SiO_2	140	~13	[27]

Table 2. **Oxidation resistance of $ZrB_2(HfB_2)$–SiC alloyed with Ta and Ta compounds** (*Completion*)

Таблица 2. **Характеристики окислительной стойкости керамик на основе $ZrB_2(HfB_2)$–SiC, модифицированных танталом и его соединениями** (*окончание*)

Composition, vol. %	Manufacturing process	Oxidation properties			Phase composition after oxidation	Reaction layer thickness, μm	Weight change, mg/cm^2	Reference
		t, °C	Time, min	Test conditions				
HfB_2–30SiC–2$TaSi_2$	HP (1900 °C, 42 MPa, 35 min)	1450	1200	TGA, dry air (15 cm^3/min)	–	–	4.1	[35]
		1500	60	Furnace, stagnant air	–	–	0.79	
		1650			–	–	6.27	
	SPS (2100 °C, 30 MPa, 3 min)	1450	1200	TGA, dry air (15 cm^3/min)	–	–	3.3	
		1500	60	Furnace, stagnant air	–	–	0.94	
		1650			–	–	2.85	
(HfB_2–30SiC)–5Ta_4HfC_5	HP + reaction (1800 °C, Ar, 30 MPa, 30 min)	1400	–	DSC/TGA, air (250 ml/min)	m-HfO_2, HfB_2	–	2.10 %	[29]
(HfB_2–30SiC)–10Ta_4HfC_5		1400	–			–	2.96 %	
		779 W/cm^2	33.3	Plasma generator, air (3.6 g/s)	m,o-Ta_2O_5, o-$Hf_6Ta_2O_{17}$	–	5.9 %	[30]
(HfB_2–30SiC)–15Ta_4HfC_5		1400	–	DSC/TGA, air (250 ml/min)	m-HfO_2, HfB_2, Ta_2O_5	–	3.27 %	[29]
HfB_2–20SiC–20$TaSi_2$	HP (1700 °C, 69 MPa, 2 h)	1627	100	Bottom-loading furnace, stagnant air	m,c-HfO_2, $HfSiO_4$	–	~2.5	[26]

Abbreviations: (ss) – solid solution; HIP – hot isostatic pressing; TGA – thermogravimetric analysis; DSC – differential scanning calorimetry.

2. Heat-resistant coatings on graphite and C/C composites based on $ZrB_2(HfB_2)$–SiC alloyed with tantalum compounds

An alternative approach is applying UHTC coatings to heat-resistant, carbon-containing composites, and graphite [47–50]. In order to protect carbon-containing materials from oxidation, ceramic coatings should have the following properties [11; 51; 52]:

1) heat resistance in a wide temperature range;

2) high adhesion, and compatibility with the substrate;

3) coating continuity and oxide film gas tightness for erosion resistance and limiting oxygen diffusion to the substrate;

4) self-healing of the coating defects;

5) high manufacturability, process consistency, controlled coating thickness, and coating repairability.

Multilayer ceramic coatings with transition metal diborides and silicon carbide are effective for increasing the oxidation resistance of carbon-containing composites by preventing oxygen penetration to the substrate. They form a silicate glass layer on the surface, and a sublayer based on refractory oxides [53; 54]. However, the protective properties of such coatings are very limited: 265 and 550 h for C/C composites with HfB_2–SiC/SiC and ZrB_2–SiC/SiC coatings at $t = 1500$ °C, respectively.

In real-life applications, the coatings should maintain the long-term performance of the carbon material in oxidizing environments in a wide temperature range, under static and dynamic loads. Therefore, an extremely important is the creation of ultra-high-temperature, durable protective coatings highly resistant to oxidation and erosion. It was proposed that tantalum be added to $ZrB_2(HfB_2)$–SiC compositions, in order to obtain multiphase coatings with good heat and ablation resistance due to the synergistic effect of the two cationic compounds exposed to a high-temperature, oxygen-containing environment [54].

2.1. Tantalum boride-alloyed $ZrB_2(HfB_2)$-SiC coatings

The addition of UHTC borides to SiC-based coatings expands the operating temperature range and improves antioxidation properties by increasing the glassy surface layer viscosity and reducing crack formation. Furthermore, B_2O_3 formed during oxidation can heal coating defects and improve resistance to low-temperature oxidation [55–57]. To protect graphite from oxidation, Jiang Y. et al. [56] applied a single-layer, multi-phase (Zr, Ta)B_2–SiC–Si coating, demonstrating oxidation resistance for 468 h at 1000 °C and for 347 h at 1500 °C. The coating structure after oxidation includes two layers: external Zr–Ta–Si–O (glass), and internal (Zr, Ta)B_2–SiC–Si. The continuous oxide film on the surface has low oxygen permeability and effectively reduces the coating oxidation rate [56].

The $Ta_{0.5}Zr_{0.5}B_2$–Si–SiC dense, single-layer multiphase ceramic coating protects graphite from oxidation at 1650 °C for at least 70 h due to the synergistic effect of the heterogeneous oxide layer formed during oxidation and the dense inner coating [55]. Also, the $Ta_{0.5}Zr_{0.5}B_2$–Si–SiC coating is resistant to ablation when exposed to heat fluxes (2.4÷4.2 MW/m^2). It was found that increasing the heat flux of the oxyacetylene flame resulted in more intense weight loss and thinning of the coating, and its ablation behavior varied from oxidation and evaporation at 2.4 MW/m^2 to mechanical removal at 4.2 MW/m^2 [55]. Note that after ablation for 40 s under a 4.2 MW/m^2 heat flux, a new microstructure consisting of “lath-like” grains ($Ta_4Zr_{11}O_{32}$ solid solution) with few micropores and high erosion resistance was found at the heat flux center. The surface oxide layer contains $Ta_4Zr_{11}O_{32}$, ZrO_2 and Ta_2O_5. These phases provide efficient protection of the material below from ablation. The inner $Ta_{0.5}Zr_{0.5}B_2$–Si–SiC coating protected by the outer oxide layer mostly faces high-temperature oxidation and the release of gaseous SiO and CO.

Jiang Y. et al. [57] manufactured a defect-free, single-layer multi-phase $Hf_{0.5}Ta_{0.5}B_2$–SiC–Si coating on graphite. After oxidation in air at $t = 1500$ °C, the coating surface contained $Ta_{0.5}B_2$, Ta_2O_5, SiO_2 and $HfSiO_4$ (hafnon is the product of the reaction between HfO_2 and SiO_2 [58]), i.e., a complex silicate oxide layer, emerges to prevent oxygen from entering into the coating. The coating is resistant to low- and high-temperature isothermal oxidation for 1320 h at $t = 900$ °C and for 2080 h at $t = 1500$ °C (the weight gains were 0.14 % and 1.74 %, respectively), and also has good ablation resistance [57]. Jiang Y. et al. [57] explained the high resistance to oxidation at $t = 900$ °C by the defect-free coating structure, and at 1500 °C, by the Hf–Ta–Si–O surface layer. Here $HfSiO_4$ and Ta_xO_y increase the oxide film viscosity and create “pinning points”, which change the direction of crack propagation or inhibit it [57].

Ren X. et al. [59] reported that a two-layer $Ta_xHf_{1-x}B_2$–SiC/SiC multiphase coating 120–190 µm thick protects C/C composites from oxidation in air at $t = 1500$ °C for more than 1480 h, and from ablation, for 40 s at the 1927 °C oxyacetylene flame temperature. The number of cracks and holes after oxidation was relatively small, when compared to the SiC/SiC coating, and the glassy layer surface contained Ta and Hf oxidation products indicating the formation of a multiphase silicate glass. The melting point of tantalum and hafnium oxides is higher than that of SiO_2, so adding these components to the glass increases its thermal stability and viscosity for better ablation and oxidation resistance through the synergistic effect of the multiphase oxides [59].

The presence of the $Zr_xTa_{1-x}B_2$ solid solution in the SiC coating significantly improves its oxidation protection properties. Ren X. et al. [60] reported that after oxidation at $t = 1500$ °C for 1412 h, the weight loss of a C/C composite coated with $Zr_xTa_{1-x}B_2$–SiC/SiC was only 0.1 wt. %, while for the ZrB_2–SiC/SiC coating, it was 0.22 wt. % for 550 h. The TGA showed the coating is resistant to oxidation in a wide temperature range (from room temperature to 1500 °C). The coated C/C composite weight gain at the end of the test was 1.8 wt. % (C/C composites with ZrB_2–SiC/SiC and TaB_2–SiC–Si/SiC coatings lost 10.3 and 11.2 wt. %) [60]. Ren X. et al. explained the high oxidation resistance of the $Zr_xTa_{1-x}B_2$–SiC/SiC coating by the formation of a heterogeneous Zr–Ta–Si–O glass layer on its surface (containing evenly distributed Zr and Ta oxides forming an “inlaid structure” providing cracks deflection and elimination), as well as by the synergistic effect of multiple protective mechanisms provided by the coating components.

Tong K. et al. [61] studied the ablation resistance of a multiphase Zr–Ta–B–SiC coating with various Zr/Ta weight ratios on a C/C composite at $t = 2300$ °C. Adding Ta led to the formation of the (Zr, Ta)B_2 solid solution, relieving thermal stress during the synthesis and removes the layer defects. Ta also had a noticeable effect on the composition and morphology of the coating after ablation. Tong K. et al. [61] also reported that the $Zr_{0.7}Ta_{0.3}B_2$–SiC coating has better ablation resistance due to the formation of a thermal barrier and low volatility of the Zr–Ta–O layer. Furthermore, the Ta–O bond stabilizes the high-temperature t-ZrO_2 phase. The samples with low Ta (~10 mol. %) and excessive Zr contents in the solid solution after ablation showed the formation of multiple nanosized Zr–Ta–O nuclei, thus making it impossible to form a homogeneous layer over the glass phase and to increase its viscosity. That is, SiO_2 was still exposed directly to the plasma generator flame and intensively evaporated during the ablation. When Ta is in excess (~70 mol. %), the ablation results in the extensive formation of the liquid Zr–Ta–O phase with low viscosity, rapidly exposing the surface. At the same time, gaseous SiO, CO, CO_2 and B_2O_3 compounds volatilized making numerous pores and holes in the glassy layer as channels for oxygen diffusion [61].

2.2. ZrB_2–SiC coatings alloyed with complex tantalum carbide

The Ta_4HfC_5 complex tantalum-hafnium carbide seems suitable for high-temperature applications with its properties [29; 30]. However, it cannot protect C/C composites from oxygen due to its low heat resistance [62]. Therefore, it was proposed to apply a 2-layer coating. The inner layer is Ta_4HfC_5 and the outer layer is ZrB_2–SiC–Ta_4HfC_5. Such a coating can be efficient to protect C/C composites from oxidation at high temperatures. The weight loss of the coated samples during isothermal oxidation tests at $t = 1500$ °C for 20 h was 3.3 %. The weight loss after ten 1500 °C to 20 °C thermal cycles with a 10 min isothermal holding at the max temperature was 9.5 %, indicating the high heat resistance and thermal stability of the coating.

The gas-tight, continuous silicate glass layer containing ZrO_2, SiO_2, $ZrSiO_4$, Ta_2O_5 and HfO_2 particles has a low oxygen diffusion rate and a relatively high self-healing ability. Nevertheless, the pores and microcracks resulting from the different thermal expansion coefficients of the coating and substrate, and from the gaseous oxidation products release, are the primary cause of weight loss. They also adversely affect the protective performance of the coating.

2.3. $ZrB_2(HfB_2)$–SiC coatings alloyed with tantalum silicides

Since the SiC thermal expansion coefficient is low, replacing it with another stable SiO_2 source would increase the protective performance of $ZrB_2(HfB_2)$–SiC coatings at temperatures above 1700 °C. Adding more components may increase the glass phase viscosity and improve the oxidation resistance of the coating.

When added to HfB_2–SiC–$TaSi_2$ coatings, the passivating power of $TaSi_2$ inhibits the intense oxidation of SiC at $t = 1700$ °C. The expansion caused by the $TaSi_2$ oxidation slows the disintegration of HfB_2 and increases the coatings structural resistance to oxidation. The addition of tantalum disilicide also leads to the formation of a heterogeneous Hf–Ta–B–Si–O high-viscosity glass layer, which reduces the oxygen permeability of the coating from 4.87 % to 0.31 % [63]. It was shown that the optimal $TaSi_2$ content has a positive effect and seems promising for alloying HfB_2–SiC coatings. Adding 20 wt. % of $TaSi_2$ slows down the coating removal rate by improving its gas tightness, while an excessive amount of $TaSi_2$ reduces the oxidation protection performance.

Tantalum disilicide is also used to improve the ablation resistance of ZrB_2–SiC coatings on C/C composites.

Adding 10 vol. % of $TaSi_2$ to a ZrB_2–27 vol. % SiC coating results in the porosity drop from 16.65 to 9.65 %, better mechanical properties, and ablation resistance at $t = 2000$ °C for 10 min [64]. The effect of $TaSi_2$ on the resistance to high-temperature gas corrosion was investigated at $t = 1700$ °C in the air for 30 min. A ZrB_2–20 vol. % SiC–10 vol. % $TaSi_2$ coating on siliconized graphite lasts much longer than a $TaSi_2$-free coating. This indicates a higher heat resistance of the former, due to the formation of a tantalum-containing oxide layer with a significantly lower oxygen permeability [65]. The ZrB_2–20 vol. % SiC–10 vol. % $TaSi_2$ oxide coating layer is significantly thinner than the ZrB_2– 20 vol. % SiC coating. Despite the absence of pores and bubbles (the $TaSi_2$-free coating has multiple defects), cracking was observed.

In order to improve the overall performance of the coating, Ren Y. et al. [66] studied the effect of additional silicon vapor infiltration as the coating is formed. The resulting ZrB_2–SiC–$TaSi_2$–Si coating on siliconized graphite efficiently protects the material from oxidation for 300 h at $t = 1500$ °C in stagnant air. The oxidation did not cause any cracking or delamination. Ren Y. et al attributed this to the modified coating structure with a dense ZrB_2–SiC–$TaSi_2$ primary layer under an additional silicon layer. The coating can withstand severe thermal cycling from 20 to 1500 °C (20 cycles). The area of the cracks per unit of surface area was only $3.8 \cdot 10^{-3}$, which indicates good thermal resistance due to the self-healing of the surface cracks. Tables 3 and 4 list some oxidation and ablation resistance properties of the coatings.

***Table 3.* Oxidation resistance of carbon materials with $ZrB_2(HfB_2)$–SiC coatings alloyed with tantalum compounds**

***Таблица 3.* Характеристики окислительной стойкости углеродных материалов с покрытиями на основе керамики $ZrB_2(HfB_2)$–SiC, модифицированной соединениями тантала**

Coating	Substrate	Manufacturing process	Oxidation conditions	Phase composition after oxidation	Weight change	Reference
ZrB_2–SiC–Ta_4HfC_5/Ta_4HfC_5	2D C/C	Slip molding/pack cementation	1500 °C, 20 h	ZrO_2, Ta_2O_5, $ZrSiO_4$, SiO_2, HfO_2, SiC	–3.3 %	[62]
ZrB_2–SiC–$TaSi_2$–Si/SiC	Graphite	Slip molding + Si vapor infiltration/ pack cementation	1500 °C, 300 h	SiO_2, ZrB_2, SiC	4.76 mg/cm^2	[66]
$(ZrTa)B_2$–SiC–Si	Graphite	Slip molding + Si vapor infiltration	1500 °C, 347 h	$(Zr, Ta)B_2$, SiO_2	0.33 %	[56]
$Zr_xTa_{1-x}B_2$–SiC/SiC	2D C/C	*In situ* reaction synthesis/pack cementation	1500 °C, 1412 h	ZrO_2, Ta_2O_5, $ZrSiO_4$, SiO_2, $Ta_2O_{2.2}$, SiC	–0.1 %	[60]
$Ta_xHf_{1-x}B_2$–SiC/SiC	2D C/C	*In situ* reaction synthesis/pack cementation	1500 °C, 1480 h	HfO_2, TaO_2, $HfSiO_4$, SiO_2, TaO, $Ta_{0.8}O_2$, Ta_2O, SiC	–2,8 mg/cm^2	[59]
$Hf_{0.5}Ta_{0.5}B_2$–SiC–Si	Graphite	Impregnation and pyrolysis + reactive Si gas infiltration	1500 °C, 2080 h	$Hf_{0.5}Ta_{0.5}B_2$, Ta_2O_5, $HfSiO_4$, SiO_2	1.74 %	[57]
$Ta_{0.5}Zr_{0.5}B_2$–Si–SiC	Graphite	Slip molding + *in situ* reactive synthesis	1650 °C, 70 h	SiO_2	–0.56 %	[55]
ZrB_2–20 vol. % SiC– 10 vol. % $TaSi_2$/SiC	Graphite	Slip molding/pack cementation	1700 °C, 30 min	ZrO_2, $ZrSiO_4$, SiO_2, TaC	3.81 mg/cm^2	[65]
HfB_2–20 wt. % SiC– 20 wt. % $TaSi_2$	Graphite	SPS	1700 °C, 100 min	HfO_2, $Ta_2O_{2.2}$, $HfSiO_4$, SiO_2	~15 mg/cm^2	[63]

Table 4. **Ablation resistance of carbon materials coated with $ZrB_2(HfB_2)$–SiC ceramics alloyed with tantalum compounds**

Таблица 4. **Характеристики стойкости к абляции углеродных материалов с покрытиями на основе керамики $ZrB_2(HfB_2)$–SiC, модифицированной соединениями тантала**

Coating	Flame test conditions				Mass ablation rate, mg/s	Linear ablation rate, μm/s	Reference
	t, °C	Time, s	Flow rate, l/s				
			O_2	C_2H_2			
$Ta_xHf_{1-x}B_2$–SiC/SiC	1927	40	0.2–0.3	0.1–0.2	1.590	3.21	[59]
ZrB_2–SiC–$TaSi_2$	2000	600	0.72	0.25	0.114	–	[64]
$Hf_{0.5}Ta_{0.5}B_2$–SiC–Si	2130	60	0.244	0.167	1.050	–10.20	[57]
$(Zr_{0.7}Ta_{0.3})B_2$–SiC	2300	120	0.42	0.31	0.033	3.01	[61]
$Ta_{0.5}Zr_{0.5}B_2$–Si–SiC	2.4 MW/m^{2*}	60	0.24	0.18	0.150	0.35	[55]
	4.2 MW/m^{2*}	40	0.42	0.31	4.900	3.25	

* Heat flux was reported instead of the flame temperature.

3. Carbon-ceramic composites with a (C)–SiC–ZrB_2 matrix alloyed with tantalum compounds

In the last decade, many researchers studied high-temperature composites with a ceramic matrix, since solid UHTCs are inherently brittle and lack sufficient resistance to thermal shock [2]. Reinforcing fibers increase the strength of the composite, and adapt its mechanical and thermal properties to the specific application. Carbon-ceramic composites (C/SiC) reinforced with continuous carbon fibers overcome the inherent brittleness and low thermal resistance of UHTCs offering better thermal performance and increased ablation resistance [1].

Kannan R. et al. [67] showed that adding 20 wt. % of Ta to the C/SiC–ZrB_2 composite leads to the Ta_xC_y formation from the residual carbon and increases the ablation resistance due to stabilization of the *t*-ZrO_2 martensitic phase and the low melting point of Ta_xC_y capable of enveloping the ZrO_2 matrix particles and reducing the anionic conductivity at $t \geq 2000$ °C. Kannan R. et al. [67] also attributed the higher ablation resistance to the low thermal conductivity of the Zr–Ta–Si–O oxide layer which inhibits the heat transfer from the surface inside the composite, and to the relatively high bond strength between the carbon fibers and the matrix due to the presence of residual metallic Ta.

Li L. et al. [68] reported that adding 24 vol. % of tantalum carbides into the matrix also resulted in higher ablation resistance of C/SiC–ZrB_2–TaC 2D composites due to the oxidation and formation of liquid Ta_2O_5 (at $t > 1870$ °C) capable of healing cracks during ablation and retaining the loose ZrO_2, building a gastight layer around the fibers. It was concluded that the TaC content should be increased, and the substance should be more evenly distributed across the matrix to further improve the ablation resistance of such composites.

C/SiC composites alloyed with ZrB_2 and TaC showed higher flexural strength (up to 27 %), Young's modulus (up to 28 %), and interlayer shear strength (up to 22 %). Uhlmann F. et al. [69] attributed the latter to the addition of TaC. The thermochemical stability of the C/SiC–ZrB_2–TaC composites under the combustion chamber conditions (exposure to a hot gas for 15 min, 1725÷1860 °C measured surface temperature) improved, while the oxygen permeability significantly decreased. The reason for this is that the oxide film in the Si–Zr–Ta–O system is a diffusion barrier, preventing the penetration of combustion products into the underlying layers and protecting them from further oxidation [69].

For the C/C–2SiC–1ZrB_2–2TaC composite (the numbers are the relative volumes of the ceramic particles) the ablation properties deteriorated which may be a result of the TaC addition. The higher ablation rate (Table 5) is attributed to the formation of the Ta_2O_5 liquid phase subject to strong mechanical removal and erosion at $t = 2700 \pm 300$ °C [70].

Table 5. **Ablation resistance of the C/SiC composite with the (C)–SiC–ZrB_2 matrix alloyed with tantalum carbide**

Таблица 5. **Характеристики стойкости к абляции УККМ с матрицей на основе (C)–SiC–ZrB_2, легированной карбидом тантала**

C/SiC composite	Manufacturing process	Density, g/cm^3	Porosity, %	Flame test conditions				Mass ablation rate, mg/s	Linear ablation rate, μm/s	Reference
				t, °C	Time, s	Gas pressure/ flow rate				
						O_2	C_2H_2			
C/SiC–ZrB_2–Ta_xC_y	Reactive HP/ impregnation and pyrolysis	2.82	21.0	1600	120	0.4 MPa	0.01 MPa	1.33	0.19	[67]
					600			0.02	0.27	
				1800	120			1.80	0.25	
					600			0.47	0.63	
				2000	120			3.05	0.39	
					600			2.19	1.43	
C/C–2SiC–1ZrB_2–2TaC	Powder infiltration + isothermal vapor infiltration	–	–	2700±300	30	1.36 m^3/h	1.04 m^3/h	~59	–	[70]
2D C/SiC–ZrB_2–TaC	Vapor infiltration + slip molding	2.35	11.5	3000	20	0.4 MPa; 1.51 m^3/h	0.095 MPa; 1.12 m^3/h	–	26	[68]

4. Mechanisms improving the oxidation and ablation resistance of $ZrB_2(HfB_2)$–SiC composites alloyed with tantalum compounds

UHTC oxidation and ablation performance is largely determined by the oxidation product properties, and the surface chemical and physical processes occurring in oxygen-containing environments. Consequently, modifications to the oxide film's chemical composition and structure can improve the resistance to high-temperature oxidation and ablation. Opeka M. et al. [7] noted that UHTC composites during the oxidation of which synthesize relatively refractory glass layers with low oxygen diffusion rates and high self-healing ability are potentially heat-resistant materials. For several reasons discussed below, alloying with tantalum compounds modifies the oxide film and improves the oxidation and ablation resistance.

4.1. Phase separation in the oxide surface layer

Oxidation of tantalum-containing components in UHTC composites can be represented by the following reactions:

$$4TaB_2(s) + 11O_2(g) \rightarrow 2Ta_2O_5(s, l) + 4B_2O_3(l), \tag{1}$$

$$4TaC(s) + 9O_2(g) \rightarrow 2Ta_2O_5(s, l) + 4CO_2(g), \tag{2}$$

$$4TaC(s) + 7O_2(g) \rightarrow 2Ta_2O_5(s, l) + 4CO(g), \tag{3}$$

$$4TaSi_2(s) + 13O_2(g) \rightarrow 2Ta_2O_5(s, l) + 8SiO_2(l), \tag{4}$$

$$x(Hf, Ta)B_2(s) + (2.5x + 0.5y)O_2(g) \rightarrow \\ \rightarrow xHfO_2(s) + Ta_xO_y(s, l) + xB_2O_3(s), \tag{5}$$

$$x(Zr, Ta)B_2(s) + (2.5x + 0.5y)O_2(g) \rightarrow \\ \rightarrow xZrO_2(s) + Ta_xO_y(s, l) + xB_2O_3(s), \tag{6}$$

where s, l and g denote the aggregate state of the phases: solid, liquid, and gaseous.

As can be seen the relatively refractory Ta_2O_5 is formed (t_{melt} = 1882 °C [10]). The presence of group IV–VI transition metal oxides (e.g., tantalum) in borosilicate glass causes intense phase separation (immiscibility) of the glass phase. It increases the heat resistance of $ZrB_2(HfB_2)$–SiC composites by increasing the liquidus temperature and viscosity [20; 21; 27; 38; 44; 55; 56; 59; 60; 65]. Higher viscosity, in turn, reduces the oxygen diffusion rate through the film. According to the Stokes-Einstein relation, the diffusion coefficient is inversely proportional to viscosity [71]:

$$D = \frac{kT}{6\pi\eta r}, \tag{7}$$

where D is the diffusion coefficient, k is the Boltzmann constant, T is the temperature, η is the solution viscosity, and r is the average radius of the diffusing particles.

Zhang M. et al. [63] showed that Hf^{4+}/Ta^{5+} transition metal cations interact with the silica-oxygen tetrahedral lattice [SiO_4] forming 3D ionic clusters. This increases the glass viscosity and reduces the oxygen mass transfer. Zhang M. et al. [63] showed that refractory hafnium and tantalum oxide particles distributed in a viscous-fluid glass layer improve heat resistance by increasing the number of barriers to oxygen movement. This significantly limits its diffusion rate through the oxide film.

Eakins E. et al. [15], Peng F. et al. [21] and Thimmappa S. et al. [44] observed a decrease in the porosity of the oxide layer under the surface glass layer. This was attributed to the higher viscosity of the glass phase containing tantalum, which is less mobile reducing the capillary rise from the lower layers. Borosilicate glass enriched with tantalum also prevents cracking and heals defects [27; 38; 64; 67; 69]. Also, the higher viscosity and liquidus temperature contribute to the partial suppression of boron evaporation from glass [7].

4.2. Formation of refractory solid solutions and complex oxides

Partial dissolution of tantalum in the zirconium or hafnium boride can result in the formation of a solid solutions which oxidizes to Zr–Ta–O and Hf–Ta–O solid solutions when exposed to oxygen [38; 44]. The reaction between the $ZrO_2(HfO_2)$ и Ta_2O_5 phases produces the $Zr_{11}Ta_4O_{32}$ ($Zr_{2.75}TaO_8$) [55] zirconium-tantalum oxides or the $Hf_6Ta_2O_{17}$ [72] hafnium-tantalum oxides, e.g.:

$$11ZrO_2(s) + 2Ta_2O_5(s, l) \rightarrow Zr_{11}Ta_4O_{32}(s), \tag{8}$$

$$6HfO_2(s) + Ta_2O_5(s, l) \rightarrow Hf_6Ta_2O_{17}(s). \tag{9}$$

The refractory solid solutions and/or complex oxides in the films enhance resistance to oxidation and ablation without inducing additional thermal stress. The mechanical and thermophysical properties of solid solutions are easier to control compared to stoichiometric phases [61]. Hu C. et al. [34] proposed that the formation of a solid solution reduces the activation energy of the boride grain boundaries, contributing to the formation of coherent structures. The $Zr_{11}Ta_4O_{32}$ и $Hf_6Ta_2O_{17}$ phases act as barriers in the oxygen-acetylene flame preventing the erosive removal of the internal layers by the high-speed gas flows due to the low thermal conductivity and relatively high refractoriness of these phases [55; 67; 72]. The heterogeneous structure of the oxide film hampers cracking and crack propagation [38].

4.3. Reducing the oxygen vacancies concentration in the $ZrO_2(HfO_2)$ lattice

Compositions that reduce oxygen transport through the ZrO_2 and HfO_2 matrix phases also increase heat resistance [7]. ZrO_2 and HfO_2 oxides become non-stoichiometric as oxygen vacancies are formed in the lattices under the low partial pressure of oxygen (e.g., under a gastight borosilicate glass layer) or due to the addition of lower valence cations (Y^{3+}, La^{3+}, etc.) [8]. The partial replacement of Zr^{4+} and Hf^{4+} with Ta^{5+} decreases the concentration of oxygen vacancies according to the Kreger-Wink reaction [26]. The reaction for the ZrO_2 lattice doping is

$$Ta_2O_5 + V_{\ddot{O}} \xrightarrow{2ZrO_2} 2Ta_{\dot{Zr}} + 5O_O. \tag{10}$$

A decrease in the oxygen vacancy concentration reduces the anionic conductivity and decreases the oxidation rate of $ZrB_2(HfB_2)$–SiC composites [26; 65].

4.4. Inhibition of $ZrO_2(HfO_2)$ polymorphic transformations

The substitution of Zr^{4+} and Hf^{4+} for Ta^{5+} in the $ZrO_2(HfO_2)$ lattice depletes the oxygen vacancies and partially stabilizes the lattice [67]. This reduces the rate of the diffusion-free martensitic tetragonal-to-monoclinic phase transformation. It also decreases the volume expansion associated with the transformation and the possibility of cracking in the oxide film during thermal cycling [8; 21; 66]. This factor improves the performance of composites exposed to high temperatures, reducing the oxide film cracking and increasing its adhesion and cohesion [61].

4.5. Changing the oxide layer microstructure

The effect of tantalum on the oxide particle size in the glass phase also affects the oxidation processes. Peng F. et al. [22] reported that the size of zirconium dioxide particles decreases when TaB_2 is added. The resulting borosilicate glass phase has a greater tendency to be captured by the lower oxide sublayers containing dispersed particles. It makes these layers more impermeable to atmospheric oxygen and improves the overall heat resistance of the material.

Tong K. et al. [61] also found that by increasing the tantalum compound content in UHTCs, the morphology of the synthesized complex oxide in the Zr–Ta–O system changes from dispersed nuclei to sintered rod-like grains. It improves the ablation resistance, since this oxide works as a "pinning" phase for efficient retention of glassy SiO_2 and resistance to mechanical erosion. Similarly, the formation of a heterogeneous oxide film in the Hf–Ta–Si–O system from the immiscible $HfSiO_4$ and Ta_xO_y phases of the silicate glass increases the surface layer viscosity and creates "pinning points", inhibiting or eliminating cracking [57]. It reduces the probability of crack penetration through the oxide film and improves heat resistance [59].

5. Reduction mechanisms of oxidation and ablation resistance in $ZrB_2(HfB_2)$–SiC composites alloyed with tantalum compounds

Along with the noted improvement in heat-resistant and anti-ablation properties when alloying $ZrB_2(HfB_2)$–SiC composites with tantalum compounds, under certain conditions these positive effects are limited, and, in some cases, oxidation and ablation resistance even deteriorates. Some studies report negative effects of tantalum compounds on the HfB_2–SiC system [26; 35], at temperatures above 1700 °C [24; 26; 39], and with improper concentrations [22; 27; 39].

The reasons for the oxidation and ablation resistance deterioration are listed below.

5.1. Formation of low-viscosity liquid phases

Adding tantalum may have a negative effect on the oxidation of $ZrB_2(HfB_2)$–SiC composites at temperatures above 1650 °C, since the presence of Ta_2O_5 in the oxide film reduces its heat resistance due to the formation of liquid phases [8; 24; 37].

High tantalum content (~70 mol. %) results in the extensive formation of the low-viscosity liquid phase during ablation. It causes intensive oxide film removal, holes, and bare areas on the surface [61].

Opila E. et al. [39] also observed the formation of a significant amount of the liquid phase (a mixture of oxiboride, silicate, and zirconate phases) during the oxidation of ZrB_2–20 vol. % SiC–20 vol. % $TaSi_2$ at t = 1927 °C, which was the key reason for the deterioration of its heat resistance [39].

5.2. Damage of frame structures in the oxide layer

The presence of Ta_2O_5 in the film at temperatures above 1700 °C leads to the formation of the $Zr_{11}Ta_4O_{32}$ or $Hf_6Ta_2O_{17}$ complex oxides. It reduces the heat resistance of the mechanical framework based on $ZrO_2(HfO_2)$, accelerating the oxidation and reducing the ablation resistance [22; 24].

Due to the limited solubility of tantalum in the ZrO_2 thermally grown *in situ* its excess forms the low-melting oxide phases, from which zirconium dioxide crystallizes contributing to the formation of dendrites [39]. Dendrite growth from the oxide sublayer to the glass surface increases the overall oxidation rate, since the dendrites act as anion channels. Another reason is the poor wetting of the dendrites with the glass phase, which contributes to increased oxygen penetration through the phase interfaces [22].

5.3. Structural changes in the oxide layer leading to porosity and cracking

The formation of Ta_2O_5 inside the ZrO_2 grains leads to a large volume expansion exceeding 50 % of the initial one. It causes irreversible damage to the ZrO_2

grains, including their cracking from the inside. This disturbs the compactness and continuity of the oxide layers and increases the mass transfer rate across the oxide film [37]. Silvestroni L. et al. [37] also noted that the platelet-shaped formations of the mixed $Zr_{2.75}TaO_8$ oxide turn vertical at $t = 1650$ °C. This configuration has extra channels for oxygen diffusion due to a significant increase in the platelets-glass phase interface surface area, which negatively affects the UHTC heat resistance.

Opila E. et al. [26] reported that adding tantalum carbides to ZrB_2–SiC reduces the oxidation resistance, since a porous oxide layer is formed due to the release of gaseous CO and/or CO_2 oxidation products. The structure discontinuity leads to accelerated oxidation, since the gas phase mass transfer through the cracks and pores (even at the Knudsen diffusion mode) is much easier than diffusion in condensed phases [24].

5.4. Changes to the oxidation mechanism

Alloying ZrB_2–SiC ceramic composites with tantalum may change the processes governing its oxidation. Wang Y. et al. [27] suggested that the mass transfer of tantalum and/or silicon cations diffusing from the substrate to the oxide film during formation of the SiC–TaC depleted layer, is crucial. At low tantalum concentrations (~10 vol. %) most of the Ta_2O_5 dissolves in ZrO_2 forming a solid solution. The remainder is insufficient to seal the porous zirconium dioxide layer, resulting in a loose structure not protected by SiO_2 and/or $ZrSiO_4$ gastight layers, and a significant increase in the UHTC oxidation rate [27].

The estimated activation energy of the silicon diffusion to the surface through the oxide layer is 315 kJ/mol. It is much higher than the previously reported values for the inward oxygen diffusion (120–140 kJ/mol [73]). This indicates the key contribution of the outward tantalum diffusion, than the inward oxygen diffusion.

5.5. Increasing the coating thermal expansion coefficient

Cracks in UHTC coatings may be caused by the difference in the substrate and coating thermal expansion coefficients [65]. The thermal expansion coefficient of tantalum compounds is higher than that of $ZrB_2(HfB_2)$ or SiC [63]. Oxidation induces compression forces in the coating, but rapid cooling leads to tensile stresses and easy cracking in the oxide layer [65]. Increasing the $TaSi_2$ content leads to heat resistance deterioration as penetrating cracks occur [63].

Conclusion

We reviewed the available studies of tantalum alloying effects on the structure and resistance to high-temperature oxidation and ablation of $ZrB_2(HfB_2)$–SiC UHTCs. The studies discuss different materials: bulk ceramics, heat-resistant coatings on C/C composites and graphite, and C/C composites with a UHTC matrix. It is shown that alloying with Ta-containing components may have both positive and negative effects. The increase in heat and ablation resistance is primarily caused by:

– higher viscosity and thermal stability of the borosilicate glass containing zirconium (hafnium) and tantalum cations;

– anionic conductivity reduction and partial stabilization of the $ZrO_2(HfO_2)$ lattice due to tantalum doping;

– compaction and sintering of the oxide sublayer containing $ZrO_2(HfO_2)$ and $ZrSiO_4(HfSiO_4)$ grains;

– formation of temperature-resistant complex oxides like $Zr_{11}Ta_4O_{32}$ or $Hf_6Ta_2O_{17}$ on the surface.

The key reasons for the negative effect of alloying are:

– poor oxide film continuity as the $ZrO_2(HfO_2)$ grains are damaged by the TaB_2 oxidation or a significant gas release during the TaC oxidation;

– the emergence of additional oxygen diffusion channels as the $Zr_{11}Ta_4O_{32}$ or $Hf_6Ta_2O_{17}$ platelets turn vertical;

– an increase of the liquid phase share subjected to mechanical removal by high-speed gas flows.

The effects of alloying are not so unambiguous: there are limitations in terms of concentration, structure, and temperature. The oxidation and ablation resistance and the mechanisms governing the UHTC behaviors are different for various alloying components and ambient conditions. Consequently, both positive and negative aspects should be considered when selecting the type and amount of alloying tantalum, as well as to determine whether one or another factor is decisive under given oxidation/ablation conditions.

References / Список литературы

1. Ni D., Cheng Y., Zhang J., Liu J.X., Zou J., Chen B., Wu H., Li H., Dong S., Han J., Zhang X., Fu Q., Zhang G.J. Advances in ultra-high temperature ceramics, composites, and coatings. *Journal of Advanced Ceramics*. 2022;11(1):1–56. https://doi.org/10.1007/s40145-021-0550-6
2. Binner J., Porter M., Baker B., Zou J., Venkatachalam V., Rubio Diaz V., D'Angio A., Ramanujam P., Zhang T., Murthy T.S.R.C. Selection, processing, properties and applications of ultra-high temperature ceramic matrix composites, UHTCMCs: a review. *International Materials Reviews*. 2020;65(7):389–444. https://doi.org/10.1080/09506608.2019.1652006
3. Ultra-high temperature ceramics: materials for extreme environment applications (Ed. by W.G. Fahrenholtz, E.J.Wuchina, W.E. Lee, Y. Zhou). Hoboken, New Jersey: John Wiley & Sons, Inc., 2014. 464 p.
4. Justin J.-F., Julian-Jankowiak A., Guerineau V., Mathivet V., Debarre A. Ultra-high temperature ceramics developments for hypersonic applications. *CEAS Aeronautical Journal*. 2020;11:651–664. https://doi.org/10.1007/s13272-020-00445-y
5. Simonenko E.P., Sevast'yanov D.V., Simonenko N.P., Sevast'yanov V.G., Kuznetsov N.T. Promising ultra-high-temperature ceramic materials for aerospace applications. *Russian Journal of Inorganic Chemistry*. 2013;58(14): 1669–1693. https://doi.org/10.1134/S0036023613140039
6. Tang S., Hu Ch. Design, preparation and properties of carbon fibers reinforced ultra-high temperature ceramic composites for aerospace applications: a review. *Journal of Materials Science & Technology*. 2017;33(2):117–130. https://doi.org/10.1016/j.jmst.2016.08.004
7. Opeka M.M., Talmy I.G., Zaykoski J.A. Oxidation-based materials selection for 2000 °C + hypersonic aerosurfaces: Theoretical considerations and historical experience. *Journal of Materials Science*. 2004;39:5887–5904. https://doi.org/10.1023/B:JMSC.0000041686.21788.77
8. Levine S.R., Opila E.J. Tantalum addition to zirconium diboride for improved oxidation resistance. *NASA/TM-2003-212483*. 2003.
9. CRC Handbook of Chemistry and Physics 85th edition. (Ed. by D.R. Lide). CRC Press, Boca Raton, FL. 2005. 2661 p.
10. Springer Handbook of condensed matter and materials data (Ed by W. Martienssen, H. Warlimont). Heidelberg: Springer, 2005. 1120 p.
11. Schmidt F.F. Tantalum and tantalum alloys. DMIC Report 133/OTS PB 151091. 1960. 328 p.
12. Mai Z., Zhang X., Liu Y., Yu H., Wang F. Insight into the structure dependence on physical properties of the high temperature ceramics TaB_2 boride. *Vacuum*. 2020;177:109427 https://doi.org/10.1016/j.vacuum.2020.109427
13. Schlesinger M.E. The Si–Ta (silicon-tantalum) system. *Journal of Phase Equilibria*. 1994;15:90–95. https://doi.org/10.1007/BF02667688
14. Zhang X., Hilmas G.E., Fahrenholtz W.G. Synthesis, densification, and mechanical properties of TaB_2. *Materials Letters*. 2008;62(27):4251–4253. https://doi.org/10.1016/j.matlet.2008.06.052
15. Lee S.J., Kim D.K. Effect of TaB_2 addition on the oxidation behaviors of ZrB_2–SiC based ultra-high temperature ceramics. *Korean Journal of Materials Research*. 2010;20(4):217–222. https://doi.org/10.3740/MRSK.2010.20.4.217
16. Eakins E., Jayaseelan D.D., Lee W.E. Toward oxidation-resistant ZrB_2–SiC ultra high temperature ceramics. *Metallurgical and Materials Transactions A*. 2011;42:878–887. https://doi.org/10.1007/s11661-010-0540-8
17. Monteverde F., Savino R. Stability of ultra-high-temperature ZrB_2–SiC ceramics under simulated atmospheric re-entry conditions. *Journal of the European Ceramic Society*. 2007;27:4797–4805. https://doi.org/10.1016/j.jeurceramsoc.2007.02.201
18. Bundschuh K., Schütze M. Materials for temperatures above 1500 °C in oxidizing atmospheres. Part I: Basic considerations on materials selection. *Materials and Corrosion*. 2001;52(3):204–212. https://doi.org/10.1002/1521-4176(200103)52:3<204::AID-MACO204>3.0.CO;2-J
19. Zhang X., Hu P., Hun J., Meng S. Ablation behavior of ZrB_2–SiC ultra high temperature ceramics under simulated atmospheric re-entry conditions. *Composites Science and Technology*. 2008;68(7-8):1718–1726. https://doi.org/10.1016/j.compscitech.2008.02.009
20. Talmy I.G., Zaykosky J.A., Opeka M.M., Dallek S. Oxidation of ZrB_2 ceramics modified with SiC and group IV–VI transition metal diborides. In: *Proceedings of the International Symposium «High Temperature Corrosion and Materials Chemistry III» (Eds. M. McNallan, E. Opila). The Electrochemical Society, Inc., Pennington, NJ*. 2001;12:144–158.
21. Peng F., Speyer R.F. Oxidation resistance of fully dense ZrB_2 with SiC, TaB_2, and $TaSi_2$ additives. *Journal of the American Ceramic Society*. 2008;91(5):1489–1494. https://doi.org/10.1111/j.1551-2916.2008.02368.x
22. Peng F., Berta Y., Speyer R.F. Effect of SiC, TaB_2 and $TaSi_2$ additives on the isothermal oxidation resistance of fully dense zirconium diboride. *Journal of Materials Research*. 2009;24(5):1855–1867. https://doi.org/10.1557/jmr.2009.0216
23. Peng F., Van Laningham G., Speyer R.F. Thermogravimetric analysis of the oxidation resistance of ZrB_2–SiC and ZrB_2–SiC–TaB_2-based compositions in the 1500–1900 °C range. *Journal of Materials Research*. 2011;26(1):96–107. https://doi.org/10.1557/jmr.2010.38
24. Hu P., Zhang X.H., Han J.C., Luo X.G., Du S.Y. Effect of various additives on the oxidation behavior of ZrB_2-based ultra-high-temperature ceramics at 1800 °C. *Journal of the American Ceramic Society*. 2010;93(2):345–349. https://doi.org/10.1111/j.1551-2916.2009.03420.x
25. Mohammadzadeh B., Jung S., Lee T.H., Le Q.V., Cha J.H., Jang H.W., Lee S.H., Kang J., Shokouhimehr M. Manufacturing ZrB_2–SiC–TaC composite: potential application for aircraft wing assessed by frequency analysis through

finite element model. *Materials*. 2020;13(10):2213. https://doi.org/10.3390/ma13102213

26. Opila E., Levine S., Lorincz J. Oxidation of ZrB_2- and HfB_2-based ultra-high temperature ceramics: Effect of Ta additions. *Journal of Materials Science*. 2004;39:5969–5977. https://doi.org/10.1023/B:JMSC.0000041693.32531.d1

27. Wang Y., Ma B., Li L., An L. Oxidation behavior of ZrB_2–SiC–TaC ceramics. *Journal of the American Ceramic Society*. 2012;95(1):374–378. https://doi.org/10.1111/j.1551-2916.2011.04945.x

28. Kakroudi M.G., Alvari M.D., Asl M.S., Vafa N.P., Rabizadeh T. Hot pressing and oxidation behavior of ZrB_2–SiC–TaC composites. *Ceramics International*. 2020;46(3):3725–3730. https://doi.org/10.1016/j.ceramint.2019.10.093

29. Simonenko E.P., Simonenko N.P., Lysenkov A.S., Sevast'yanov V.G., Kuznetsov N.T. Reactive hot pressing of HfB_2–SiC–Ta_4HfC_5 ultra-high temperature ceramics. *Russian Journal of Inorganic Chemistry*. 2020;65:446–457. https://doi.org/10.1134/S0036023620030146

30. Simonenko E.P., Simonenko N.P., Gordeev A.N., Kolesnikov A.F., Chaplygin A.V., Lysenkov A.S., Nagornov I.A., Sevastyanov V.G., Kuznetsov N.T. Oxidation of HfB_2–SiC–Ta_4HfC_5 ceramic material by a supersonic flow of dissociated air. *Journal of the European Ceramic Society*. 2021;41(2):1088–1098. https://doi.org/10.1016/j.jeurceramsoc.2020.10.001

31. McCormack S.J., Tseng K., Weber R.J.K., Kapush D., Ushakov S.V., Navrotsky A., Kriven W.M. In-situ determination of the HfO_2–Ta_2O_5-temperature phase diagram up to 3000 °C. *Journal of the American Ceramic Society*. 2019;102(8):4848–4861. https://doi.org/10.1111/jace.16271

32. Potanin A.Yu., Astapov A.N., Pogozhev Yu.S., Rupasov S.I., Shvyndina N.V., Klechkovskaya V.V., Levashov E.A., Timofeev I.A, Timofeev A.N. Oxidation of HfB_2–SiC ceramics under static and dynamic conditions. *Journal of the European Ceramic Society*. 2021;41(16):34–47. https://doi.org/10.1016/j.jeurceramsoc.2021.09.018

33. Hu C., Sakka Y., Tanaka H., Nishimura T., Guo S., Grasso S. Microstructure and properties of ZrB_2–SiC composites prepared by spark plasma sintering using $TaSi_2$ as sintering additive. *Journal of the European Ceramic Society*. 2010;30(12):2625–2631. https://doi.org/10.1016/j.jeurceramsoc.2010.05.013

34. Hu C., Sakka Y., Gao J., Tanaka H., Grasso S. Microstructure characterization of ZrB_2–SiC composite fabricated by spark plasma sintering with $TaSi_2$ additive. *Journal of the European Ceramic Society*. 2012;32(7):1441–1446. https://doi.org/10.1016/j.jeurceramsoc.2011.08.024

35. Monteverde F. Ultra-high temperature HfB_2–SiC ceramics consolidated by hot-pressing and spark plasma sintering. *Journal of Alloys and Compounds*. 2007;428(1-2):197–205. https://doi.org/10.1016/j.jallcom.2006.01.107

36. Talmy I.G., Zaykoski J.A., Opeka M.M. High-temperature chemistry and oxidation of ZrB_2 ceramics containing SiC, Si_3N_4, Ta_5Si_3, and $TaSi_2$. *Journal of the American Ceramic Society*. 2008;91(7):2250–2257. https://doi.org/10.1111/j.1551-2916.2008.02420.x

37. Silvestroni L., Kleebe H.-J. Critical oxidation behavior of Ta-containing ZrB_2 composites in the 1500–1650 °C temperature range. *Journal of the European Ceramic Society*. 2017;37(5):1899–1908. https://doi.org/10.1016/j.jeurceramsoc.2017.01.020

38. Wang S., Xu C., Ding Y., Zhang X. Thermal shock behavior of ZrB_2–SiC composite ceramics with added $TaSi_2$. *International Journal of Refractory Metals and Hard Material*. 2013;41:507–516. https://doi.org/10.1016/j.ijrmhm.2013.06.010

39. Opila E.J., Smith J., Levine S.R., Lorincz J., Reigel M. Oxidation of $TaSi_2$-containing ZrB_2–SiC ultra-high temperature materials. *The Open Aerospace Engineering Journal*. 2010;3:41–51. https://doi.org/10.2174/1874146001003010041

40. Julian-Jankowiak A., Mathivet V., Justin J.-F., Guérineau V. Development of ultra-high temperature ceramics: from monoliths to composites. *Materials Science Forum*. 2018;941:2041–2046. https://doi.org/10.4028/www.scientific.net/MSF.941.2041

41. Golla B.R., Thimmappa S.K. Comparative study on microstructure and oxidation behaviour of ZrB_2–20vol.% SiC ceramics reinforced with Si_3N_4/Ta additives. *Journal of Alloys and Compounds*. 2019;797:92–100. https://doi.org/10.1016/j.jallcom.2019.05.097

42. Dorner A.N., Werbach K., Hilmas G.E., Fahrenholtz W.G. Effect of tantalum solid solution additions on the mechanical behavior of ZrB_2. *Journal of the European Ceramic Society*. 2021;41(6):3219–3226. https://doi.org/10.1016/j.jeurceramsoc.2020.12.049

43. McClane D.L., Fahrenholtz W.G., Hilmas G.E. Thermal properties of (Zr, TM)B_2 solid solutions with TM = Ta, Mo, Re, V, and Cr. *Journal of the American Ceramic Society*. 2015;98(2):637–644. https://doi.org/10.1111/jace.13341

44. Thimmappa S.K., Golla B.R. Effect of tantalum addition on microstructure and oxidation of spark plasma sintered ZrB_2–20 vol % SiC composites. *Ceramics International*. 2019;45(11):13799–13808. https://doi.org/10.1016/j.ceramint.2019.04.076

45. Thimmappa S.K., Golla B.R., Pitchuka S.B., Prasad B. Nanoindentation and high temperature oxidation behavior of ZrB_2–20SiC–(0–10 wt.%) Ta UHTCs. *Ceramics International*. 2021;47(15):22184–22190. https://doi.org/10.1016/j.ceramint.2021.04.241

46. Yang Y., Qian Y., Xu J., Li M. Effects of TaSi2 addition on room temperature mechanical properties of ZrB_2–20SiC composites. *Ceramics International*. 2018;44(14):16150–16156. https://doi.org/10.1016/j.ceramint.2018.05.075

47. Ren X., Wang L., Feng P., Zhang P., Guo L., Sun X., Mo H., Li Z. Low temperature synthesis of pure phase TaB_2 powders and its oxidation protection modification behaviors for Si-based ceramic coating in dynamic oxidation environments. *Ceramics International*. 2018;44(13):15517–15525. https://doi.org/10.1016/j.ceramint.2018.05.212

48. Ren X., Wang W., Chen P., Chu H., Feng P., Guo L., Li Z. Investigations of TaB_2 on oxidation-inhibition property and mechanism of Si-based coatings in aerobic environment with broad temperature region for carbon materials. *Journal of the European Ceramic Society*. 2019;39(15):4554–4564. https://doi.org/10.1016/j.jeurceramsoc.2019.07.020

49. Yuan J., Song W., Zhang H., Zhou X., Dong S., Jiang J., Deng L., Cao X. $TaZr_{2.75}O_8$ ceramics as a potential thermal

barrier coating material for high-temperature applications. *Materials Letters*. 2019;247:82–85.
https://doi.org/10.1016/j.matlet.2019.03.102

50. Liu Q., Hu X., Zhu W., Guo J., Tan Z. Effects of Ta_2O_5 content on mechanical properties and high-temperature performance of $Zr_6Ta_2O_{17}$ thermal barrier coatings. *Journal of the American Ceramic Society*. 2021;104(12):6533–6544. https://doi.org/10.1111/jace.17990

51. Yurishcheva A., Astapov A., Lifanov I., Rabinskiy L. High temperature coatings for oxidation and erosion protection of heat-resistant carbonaceous materials in high-speed flows. *Key Engineering Materials*. 2018;771:103–117.
https://doi.org/10.4028/www.scientific.net/KEM.771.103

52. Corral E.L., Loehman R.E. Ultra-high-temperature ceramic coatings for oxidation protection of carbon-carbon composites. *Journal of the American Ceramic Society*. 2008;91(5):1495–1502.
https://doi.org/10.1111/j.1551-2916.2008.02331.x

53. Ren X., Li H., Chu Y., Fu Q., Li K. Preparation of oxidation protective ZrB_2–SiC coating by in-situ reaction method on SiC-coated carbon/carbon composites. *Surface & Coatings Technology*. 2014;247:61–67.
https://doi.org/10.1016/j.surfcoat.2014.03.017

54. Ren X., Li H., Chu Y., Fu Q., Li K. Ultra-high-temperature ceramic HfB_2–SiC coating for oxidation protection of SiC-coated carbon/carbon composites. *International Journal of Applied Ceramic Technology*. 2015;12(3):560–567. https://doi.org/10.1111/ijac.12241

55. Jiang Y., Yin S., Li M., Zhang Z., Tang G., Wang N., Ru H. Oxidation and ablation behaviour of multiphase ultra-high-temperature ceramic $Ta_{0.5}Zr_{0.5}B_2$–Si–SiC protective coating for graphite. *Ceramics International*. 2021;47(8):11358–11371.
https://doi.org/10.1016/j.ceramint.2020.12.262

56. Jiang Y., Wang W., Ru H. Oxidation protection of (ZrTa)B_2–SiC–Si coating for graphite materials. *Surface Engineering*. 2019;35(4):317–324.
https://doi.org/10.1080/02670844.2018.1472925

57. Jiang Y., Liu T., Ru H., Wang W., Zhang C., Wang L. Oxidation and ablation protection of multiphase $Hf_{0.5}Ta_{0.5}B_2$–SiC–Si coating for graphite prepared by dipping-pyrolysis and reactive infiltration of gaseous silicon. *Applied Surface Science*. 2018;459:527–536.
https://doi.org/10.1016/j.apsusc.2018.08.042

58. Wang P., Li H., Ren X., Yuan R., Hou X., Zhang Y. HfB_2–SiC–$MoSi_2$ oxidation resistance coating fabricated through in-situ synthesis for SiC coated C/C composites. *Journal of Alloys and Compounds*. 2017;722:69–76.
https://doi.org/10.1016/j.jallcom.2017.06.008

59. Ren X., Li H., Fu Q., Li K. $TaxHf_{1-x}B_2$–SiC multiphase oxidation protective coating for SiC-coated carbon/carbon composites. *Corrosion Science*. 2014;87:479–488.
https://doi.org/10.1016/j.corsci.2014.07.016

60. Ren X., Li H., Li K., Fu Q. Oxidation protection of ultra-high temperature ceramic $Zr_xTa_{1-x}B_2$–SiC/SiC coating prepared by in-situ reaction method for carbon/carbon composites. *Journal of the European Ceramic Society*. 2015;35(3):897–907.
https://doi.org/10.1016/j.jeurceramsoc.2014.09.038

61. Tong K., Zhang M., Su Z., Wu X., Zeng C., Xie X., Fang C., Yang C., Huang Q., Huang D. Ablation behavior of (Zr,Ta)B_2–SiC coating on carbon/carbon composites at 2300 °C. *Corrosion Science*. 2021;188:109545.
https://doi.org/10.1016/j.corsci.2021.109545

62. Zhou C., Qi Y., Cheng Y., Han W. ZrB_2–SiC–Ta_4HfC_5/Ta_4HfC_5 oxidation-resistant dual-layer coating fabricated by spark plasma sintering for C/C composites. *Journal of Materials Engineering and Performance*. 2019;28: 512–518. https://doi.org/10.1007/s11665-018-3807-7

63. Zhang M., Ren X., Chu H., Lv J., Li W., Wang W., Yang Q., Feng P. Oxidation inhibition behaviors of the HfB_2–SiC–$TaSi_2$ coating for carbon structural materials at 1700 °C. *Corrosion Science*. 2020;177:108982.
https://doi.org/10.1016/j.corsci.2020.108982

64. Wang R., Zhu S., Huang H., Wang Z., Liu Y., Ma Z., Qian F. Low-pressure plasma spraying of ZrB_2–SiC coatings on C/C substrate by adding $TaSi_2$. *Surface & Coatings Technology*. 2021;420:127332.
https://doi.org/10.1016/j.surfcoat.2021.127332

65. Ren Y., Qian Y., Xu J., Zuo J., Li M. Ultra-high temperature oxidation resistance of ZrB_2–20SiC coating with $TaSi_2$ addition on siliconized graphite. *Ceramics International*. 2019;45(12):15366–15374.
https://doi.org/10.1016/j.ceramint.2019.05.030

66. Ren Y., Qian Y., Xu J., Jiang Y., Zuo J., Li M. Oxidation and cracking/spallation resistance of ZrB_2–SiC–$TaSi_2$–Si coating on siliconized graphite at 1500 °C in air. *Ceramics International*. 2020;46(5):6254–6261.
https://doi.org/10.1016/j.ceramint.2019.11.095

67. Kannan R., Rangaraj L. Properties of Cf/SiC–ZrB_2–Ta_xC_y composite produced by reactive hot pressing and polymer impregnation pyrolysis (RHP/PIP). *Journal of the European Ceramic Society*. 2019;39(7):2257–2265.
https://doi.org/10.1016/j.jeurceramsoc.2019.02.025

68. Li L., Wang Y., Cheng L., Zhang L. Preparation and properties of 2D C/SiC–ZrB_2–TaC composites. *Ceramics International*. 2011;37(3):891–896.
https://doi.org/10.1016/j.ceramint.2010.10.033

69. Uhlmann F., Wilhelmi C., Schmidt-Wimmer S., Beyer S., Badini C., Padovano E. Preparation and characterization of ZrB_2 and TaC containing Cf/SiC composites via polymer-infiltration-pyrolysis process. *Journal of the European Ceramic Society*. 2017;37(5):1955–1960.
https://doi.org/10.1016/j.jeurceramsoc.2016.12.048

70. Tang S., Deng J., Wang S., Liu W., Yang K. Ablation behaviors of ultra-high temperature ceramic composites. *Materials Science and Engineering: A*. 2007.465(1-2):1–7.
https://doi.org/10.1016/j.msea.2007.02.040

71. Dunstan D.E., Stokes J. Diffusing probe measurements of polystyrene latex particles in polyelectrolyte solutions: deviations from Stokes-Einstein behavior. *Macromolecules*. 2000;33(1):193–198.
https://doi.org/10.1021/ma9908503

72. Li M., Xu Q., Wang L. Thermal conductivity of $(Hf_{1-x}Zr_x)_6Ta_2O_{17}$ (x = 0, 0.1, 0.3 and 0.5) ceramics. *Ceramics International*. 2012;38(5):4357–4361.
https://doi.org/10.1016/j.ceramint.2011.12.080

73. Jacobson N.S. Corrosion of silicon-based ceramics in combustion environments. *Journal of the American Ceramic Society*. 1993;76(1):3–28.
https://doi.org/10.1111/j.1151-2916.1993.tb03684.x

Information about the Authors

Anna A. Didenko – Cand. Sci. (Eng.), Assistant Professor of the Department of Engineering Graphics, Moscow Aviation Institute (National Research University)
ORCID: 0000-0002-2827-8077
E-mail: yurishcheva@yandex.ru

Alexey N. Astapov – Cand. Sci. (Eng.), Assistant Professor of the Department of Advanced Materials and Technologies for Aerospace Application, Moscow Aviation Institute (National Research University)
ORCID: 0000-0001-8943-2333
E-mail: lexxa1985@inbox.ru

Valentina S. Terentieva – Dr. Sci. (Eng.), Full Professor of the Department of Advanced Materials and Technologies for Aerospace Application, Moscow Aviation Institute (National Research University)
ORCID: 0000-0002-0919-8442
E-mail: k903ter@mai.ru

Сведения об авторах

Анна Александровна Диденко – к.т.н., доцент кафедры «Инженерная графика», Московский авиационный институт (национальный исследовательский университет) (МАИ (НИУ))
ORCID: 0000-0002-2827-8077
E-mail: yurishcheva@yandex.ru

Алексей Николаевич Астапов – к.т.н., доцент кафедры «Перспективные материалы и технологии аэрокосмического назначения», МАИ (НИУ)
ORCID: 0000-0001-8943-2333
E-mail: lexxa1985@inbox.ru

Валентина Сергеевна Терентьева – д.т.н., профессор кафедры «Перспективные материалы и технологии аэрокосмического назначения», МАИ (НИУ)
ORCID: 0000-0002-0919-8442
E-mail: k903ter@mai.ru

Contribution of the Authors

A. A. Didenko – formation of the main concept, search and analysis of the literature, writing the text, formulation of the conclusions.

A. N. Astapov – formation of the main concept, goal and objectives of the study, writing the text, formulation and justification of the heat resistance mechanisms.
V. S. Terentieva – correction of the text and conclusions.

Вклад авторов

А. А. Диденко – формирование основной концепции, поиск и анализ литературы, подготовка текста статьи, формулировка выводов.
А. Н. Астапов – формирование основной концепции, постановка цели и задачи исследования, подготовка текста статьи, формулировка и обоснование механизмов жаростойкости.
В. С. Терентьева – корректировка текста, корректировка выводов.

Received 05.12.2022
Revised 17.12.2022
Accepted 23.12.2022

Статья поступила 05.12.2022 г.
Доработана 17.12.2022 г.
Принята к публикации 23.12.2022 г.

UDC 546.271

https://doi.org/10.17073/1997-308X-2023-2-35-45

Research article
Научная статья

Synthesis of B_4C–TiB_2 composition powder mixtures by carbidobor reduction using nanofibrous carbon for ceramic fabrication

T. S. Gudyma[1], **Yu. L. Krutskii**[1], **E. A. Maksimovskiy**[2], **N. Yu. Cherkasova**[1], **N. I. Lapekin**[1], **T. V. Larina**[3]

[1] **Novosibirsk State Technical University**
20 Karl Marks Prosp., Novosibirsk 630073, Russia
[2] **Nikolaev Institute of Inorganic Chemistry, Siberian Branch of the Russian Academy of Sciences**
3 Lavrent'eva Prosp., Novosibirsk 630090, Russia
[3] **Boreskov Institute of Catalysis, Siberian Branch of the Russian Academy of Sciences**
5 Lavrent'eva Prosp., Novosibirsk 630090, Russia

gudymatan@mail.ru

Abstract. The results of the researching process of obtaining composition powder material B_4C–TiB_2 by carbide reduction of titanium dioxide, using carbon reducing agent – carbon nanofibers, are presented. Furthermore, the results of studying of some properties of ceramics made using the synthesized powder are presented. The synthesis of composite materials was carried out in an induction crucible furnace for 20 min in the temperature range of 1200–1900 °C in an argon atmosphere. It has been established that the optimum temperature of the synthesis is 1650 °C, irrespective of the batch composition. The characteristics of the composite powders containing 10–30 mol. % of the TiB_2 phase have been studied. *X*-ray electron microscopy has revealed that the particles of the powder are predominantly aggregated. There are two peaks in the particle size distribution histograms. The part of the histogram with a smaller particle size mainly characterizes the B_4C phase. The part of the histogram with a larger particle size characterizes the TiB_2 phase. The average particle size of the B_4C phase is in the range of 5.3–5.5 μm, and that of the TiB_2 phase is in the range of 33.6–41.9 μm. The average size of 50 % of composite powder's particles for these contents does not exceed 13.4 μm. The surface area of the samples does not exceed 5 m^2/g. The oxidation of the composite powder materials by atmospheric oxygen begins at a temperature of approximately 500 °C. At the same time, when the temperature reaches 1000 °C, no more than 45 wt. % of the studied powders is oxidized. Ceramics made with the synthesized powder mixture B_4C + 30 mol. % TiB_2 by hot pressing has shown rather high values of relative density (99.0±1.1 %) and fracture toughness (5.0±0.2 MPa·$m^{0.5}$).

Keywords: boron carbide, titanium diboride, carbide reduction, nanofibrous carbon (NFC), high-temperature synthesis

Acknowledgements: The research was performed in accordance with the state order of the Ministry of Education and Science (code FSUN-2023-0008).

For citation: Gudyma T.S., Krutskii Yu.L., Maksimovskiy E.A., Cherkasova N.Yu., Lapekin N.I., Larina T.V. Synthesis of B_4C–TiB_2 composition powder mixtures by carbidobor reduction using nanofibrous carbon for ceramic fabrication. *Powder Metallurgy and Functional Coatings*. 2023;17(2):35–45. https://doi.org/10.17073/1997-308X-2023-2-35-45

Синтез композиционных порошковых смесей $B_4C–TiB_2$ методом карбидоборного восстановления с использованием нановолокнистого углерода для изготовления керамики

Т. С. Гудыма[1] ✉, **Ю. Л. Крутский**[1], **Е. А. Максимовский**[2],
Н. Ю. Черкасова[1], **Н. И. Лапекин**[1], **Т. В. Ларина**[3]

[1] **Новосибирский государственный технический университет**
630073, г. Новосибирск, пр-т Карла Маркса, 20
[2] **Институт неорганической химии им. А.В. Николаева Сибирского отделения РАН**
630090, г. Новосибирск, пр-т Академика Лаврентьева, 3
[3] **Институт катализа им. Г.К. Борескова Сибирского отделения РАН**
630090, г. Новосибирск, пр-т Академика Лаврентьева, 5

✉ gudymatan@mail.ru

Аннотация. Представлены результаты исследования процесса получения порошковых смесей $B_4C–TiB_2$ методом карбидоборного восстановления диоксида титана в присутствии восстановителя – нановолокнистого углерода, а также изучения некоторых свойств керамики, изготовленной с использованием синтезированного порошка. Синтез порошковых смесей проводили в индукционной тигельной печи в течение 20 мин в диапазоне температур 1200–1900 °С в среде инертного газа – аргона. Установлено, что оптимальная температура процесса синтеза независимо от состава шихты составляет 1650 °С. Изучены характеристики порошков, содержащих 10–30 мол. % фазы TiB_2. Методом рентгеновской электронной микроскопии установлено, что частицы порошка преимущественно агрегированы. На гистограммах распределения частиц по размерам присутствуют два пика: первый (с меньшим размером частиц) в основном характеризует фазу B_4C, а второй (с крупными частицами) – фазу TiB_2. Средний размер частиц фазы B_4C составляет 5,3–5,5 мкм, а фазы TiB_2 – 33,6–41,9 мкм. Средний размер 50 % частиц порошка для исследуемых составов не больше 13,4 мкм. Величина удельной поверхности образцов не превышает 5 $м^2/г$. Окисление полученных смесей кислородом воздуха начинается при температуре около 500 °С. При этом при достижении температуры 1000 °С окисляется не более 45 мас. % исследуемых порошков. Керамика, изготовленная с использованием синтезированной порошковой смеси $B_4C + 30$ мол. % TiB_2 методом горячего прессования, продемонстрировала достаточно высокие значения относительной плотности (99,0±1,1 %) и трещиностойкости (5,0±0,2 $МПа·м^{0,5}$).

Ключевые слова: карбид бора, диборид титана, карбидоборное восстановление, нановолокнистый углерод (НВУ), высокотемпературный синтез

Благодарности: Исследование выполнено в соответствии с госзаданием Минобрнауки (код FSUN-2023-0008).

Для цитирования: Гудыма Т.С., Крутский Ю.Л., Максимовский Е.А., Черкасова Н.Ю., Лапекин Н.И., Ларина Т.В. Синтез композиционных порошковых смесей $B_4C–TiB_2$ методом карбидоборного восстановления с использованием нановолокнистого углерода для изготовления керамики. *Известия вузов. Порошковая металлургия и функциональные покрытия*. 2023;17(2):35–45. https://doi.org/10.17073/1997-308X-2023-2-35-45

Introduction

Over the past 20 years, the study of the production and properties of $B_4C–TiB_2$ composite ceramics has attracted a great interest, driven by the combination of the unique properties of their components – boron carbide and titanium diboride.

Boron carbide exhibit a high melting temperature (2447 °C) and possesses a unique combination of high hardness (up to 43 GPa) and low density (2.52 g/cm^3) [1; 2]. However, ceramics based on it are characterized by poor sintering and low fracture toughness. The use of modifying additives, such as titanium diboride, can significantly increase these indices by 10–40 % [3; 4].

Titanium diboride, as well as boron carbide, is a refractory compound, its melting temperature is ~3225 °C [5]. The microhardness of TiB_2 ceramics is rather high and amounts to 25–35 GPa. Titanium diboride exhibit a relatively high thermal conductivity coefficient (66.4 W/(m·K)) and low specific electrical toughness (~10^{-7} Ohm·m) [6; 7]. Furthermore, TiB_2 is quite stable when heated in air, and it is not oxidized at a temperature of up to 800 °C. At a temperature of 900 °C, it is slightly oxidized with the formation of a vitreous protective film on the surface of the material, which prevents its further oxidation [8].

Many researchers note an increase in the fracture toughness and sinterability of the ceramics based on B_4C–TiB_2 system in comparison with the ceramics containing only B_4C [9; 10]. The presence of TiB_2 prevents the growth of B_4C grains, reduces the sintering temperature and improves the mechanical properties of the resulting composite [11; 12]. Besides, there are data [13; 14] being indicative of the fact that the presence of TiB_2 increases the electrical conductivity of B_4C–TiB_2 material. B_4C–TiB_2 composite of eutectic composition can itself act as a modifying additive for refractory ceramics, increasing its mechanical properties [15].

In most cases, ready-made B_4C and TiB_2 powders are used as batch components for the production of B_4C–TiB_2 composite ceramic material [14; 16]. The preparation of such a batch before compaction involves mixing using a planetary ball mill.

The literary sources present the data on the production of B_4C–TiB_2 composites by *in situ* methods in accordance with reactions (1) [17], (2) [3] and (3) [18]:

$$\mathrm{Ti} + 6\mathrm{B} + \mathrm{C} = \mathrm{B_4C} + \mathrm{TiB_2}, \tag{1}$$

$$\mathrm{TiC} + 6\mathrm{B} = \mathrm{B_4C} + \mathrm{TiB_2}, \tag{2}$$

$$(1 + x)\mathrm{B_4C} + 2x\mathrm{TiO_2} + 3x\mathrm{C} = \\ = \mathrm{B_4C} + 2x\mathrm{TiB_2} + 4x\mathrm{CO}. \tag{3}$$

The advantage of running the processes in accordance with reactions (1) and (2) is the absence of gaseous products, which is particularly important for the simultaneous synthesis and compaction of the material. On the other hand, the use of expensive boron and long-term mixing of the batch are required. Reaction (3) is prospective for the preliminary production of B_4C–TiB_2 batch due to the use of cheaper reagents. For instance, in terms of producing a mixture with a molar ratio of $B_4C:TiB_2 = 1:1$, the cost of reagents for reaction (3) is almost 5 times lower than for reactions (1) and (2). In addition, the gaseous product release during the heat treatment can contribute to additional mixing of the batch and more uniform heating.

Acetylene black is most often used as a carbon source in carbide synthesis. This material exhibit a rather high surface area of ~50 m^2/g. However, nanofibrous carbon (NFC) with a developed surface area (~150 m^2/g) can serve as a more efficient carbon material [19]. A highly dispersed carbon agent can accelerate the formation of titanium diboride due to more intensive diffusion of carbon into titanium dioxide particles. It should be noted that there are some technological challenges in using NFC. This highly dispersed material is prone to caking and requires thorough homogenization of the reaction mixture before the heat treatment. Besides, NFC is a more expensive reagent, its price is about 5 times higher than that of acetylene black. However, in light of the fact that the mass fraction of carbon agent in the reaction mixture for reaction (3) is relatively low, the cost of final product increases insignificantly.

The purpose of this paper is to research the synthesis and study the properties of $B_4C + TiB_2$ composite powder materials obtained by the carbide reduction of titanium dioxide (reaction (3)) using NFC.

Research methods

To obtain $B_4C + TiB_2$ powder composites, the following reagents were used:

– highly dispersed boron carbide B_4C (assay 98.5 wt. %, average particle size $d = 2.1$ μm) synthesized from simple substances according to method [20];

– titanium dioxide (TU 6-09-3811-79, assay 99.0 wt. %, $d = 1.0$ μm);

– nanofibrous carbon (carbon content 99 wt. %) [21; 22].

The used NFC contained catalyst residues: ~0.1 wt. % Al_2O_3 and 0.9 wt. % Ni. In its initial form, the carbon material consisted of pellets being 0.4–8.0 mm in size formed by densely intertwined fibers with an average diameter of 73 nm. The NFC pellets were pre-ground in the AGO-2S planetary ball mill for 5 min at an acceleration of 15g and a NFC to ball mass ratio of 1:15. The average particle size of NFC after grinding was 3.9 μm.

According to the diagram of B_4C–TiB_2 system state at the eutectic point, the content of TiB_2 is ~26 mol. % [23]. The composite powder materials, the composition of which corresponds to the eutectic point and beyond it, were selected for research. The ratio of reagents was selected so that the composite powder materials containing 10, 20, 25, and 30 mol. % of TiB_2 were obtained in accordance with reaction (3). In calculating the batch composition, the presence of impurities in the composition of reagents was taken into account. The samples were designated as T10, T20, T25 and T30, respectively. The initial powders were mixed in a planetary ball mill for 5 min at an acceleration of 20g, and then they were sifted through a sieve with a mesh size of 100 μm.

The synthesis was performed in the VCh-25AV induction crucible furnace (Russia). Argon was chosen as an inert atmosphere preventing nitriding of boron carbide and titanium diboride. During carbide reduction of titanium dioxide, gaseous products (CO and CO_2) are released and the pressure in the system increases. To ensure the safety of the process, the synthesis should be performed in a flow reactor, ensuring continuous removal of the resulting gases by an argon flow. The temperature was controlled using the Kelvin Compact 2300 optical pyrometer (PC EUROMIX, Russia). The pressure in the reactor was almost atmospheric. The temperatures of the beginning of titanium dioxide reduction were determined by performing the thermodynamic calculations in accordance with the procedure [24]. The temperatures were calculated for different CO pressures, since it is difficult to estimate the partial pressure of CO in Ar + CO gas mixture.

The value of the isobaric-isothermal potential of the reaction of carbide reduction of titanium dioxide turns negative at the temperatures of 745, 849 and 994 °C for CO pressures of 0.001, 0.01 and 0.1 MPa, respectively.

In this research, the heat treatment of the batch was initially performed to prepare a mixture of B_4C–25 mol. % TiB_2 (T25) at $t = 1200$, 1400, 1650 and 1900 °C for 20 min in accordance with reaction (3). The completeness of the process was evaluated by weighing the batch and the reaction products, as well as by comparing experimental data with the theoretical ones. The estimated weight loss upon the completeness of this reaction was 19.05 wt. %. In practice, this value may slightly differ from the estimated value. This is due to the presence of impurities in the reagents used, as well as due to the possibility of the formation of aluminum borocarbide $Al_3B_{48}C_2$, being prone to oxidation and hydration, during the synthesis. Since the results of the conducted studies revealed that the optimal synthesis temperature is 1650 °C, further experiments with a batch of a different composition were performed at the same temperature for 20 min.

The *X*-ray phase analysis (XPA) of the obtained powders was performed by means of DRON-3 diffractometer using CuK_α-radiation. The diffraction patterns were interpreted using Power Diffraction File (PDF-2) database. The ratio of B_4C and TiB_2 phases was estimated using the corundum number method.

The total carbon content was determined by infrared absorption spectrometry using the CS 844 sulfur and carbon analyzer (LECO Corporation, the USA) as per GOST 12344-2003.

The microstructure of the powders and the morphology of the particles were studied using S-3400N scanning electron microscope (Hitachi, Japan) equipped with an energy-dispersive analysis attachment (Oxford Instruments Analytical, the United Kingdom). The particle size distribution was evaluated by means of laser particle size analyzer MicroSizer 201 VA Instrument (VA Instalt LLC, Russia). The surface area was determined by the method of low-temperature nitrogen adsorption using NOVA 2200e device (Quantachrome Instruments, the USA).

The thermal-oxidative stability of the samples was determined using STA 449 C Jupiter synchronous thermal analysis instrument (Netzsch, Germany). During the analysis, the sample was oxidized in an atmosphere of synthetic air when heated up to a temperature of 1000 °C at a rate of 15 °C/min.

Experiments on the production of $B_4C–TiB_2$ composite ceramics were performed on a hot pressing unit designed by the Institute of Automation and Electrometry, the Siberian Branch of the Russian Academy of Sciences (Novosibirsk), using a synthesized powder containing 30 mol. % of TiB_2. In this case, the batch was pre-ground in a planetary ball mill at an acceleration of 20*g* for 5 min at a mass ratio of the batch to balls of 1:30. The process was carried out in argon atmosphere at a pressing pressure of 25 MPa and a temperature of 2100 °C.

The relative density and open porosity of ceramics were evaluated in accordance with GOST 2409-2014 using AD-1653 hydrostatic weighing set installed on GR-300 analytical balance (AND, Japan).

Vickers microhardness measurements were performed on 402MVD unit (Wolpert Group, Great Britain). The indentation load was 500 g. At least 5 punctures were applied to the samples in such a way that the distance between the center of one indent and the edge of the next one was at least 2.5 lengths of the diagonal of the indent.

The fracture toughness was determined by indentation on a hardness tester of TP model No. 3534 (Russia) with an indenter in the form of a 4-sided diamond Vickers pyramid with a load of 5 kg. Its values were calculated according to equation [25]

$$K_{1c} = 0.048\left(\frac{l}{a}\right)^{-0,5}\left(\frac{H_v}{E\Phi}\right)^{-0,4}\frac{H_v a^{0,5}}{\Phi},$$

where l is the fracture length, μm; a is the half-diagonal of impression, μm; H_v is the microhardness, GPa; E is the Young modulus, GPa; $\Phi = 3$ is the constant.

Results and discussion

Fig. 1 shows the *X*-ray diffraction patterns of the synthesized samples of B_4C–25 mol. % TiB_2 mixture. It can be seen that at the synthesis temperatures $t = 1200$ and 1400 °C the peaks of both the target B_4C and TiB_2 phases and the unreacted carbon are observed for condensed products. At $t = 1650$ and 1900 °C, B_4C and TiB_2 phases are formed in the reaction products, and the *X*-ray diffraction patterns show the impurity reflections of $Al_3B_{48}C_2$

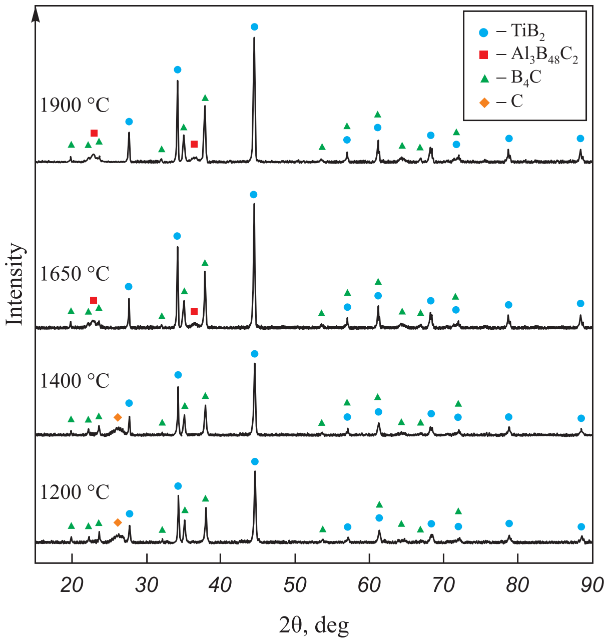

Fig. 1. The diffraction patterns of the samples of B_4C–25 mol. % TiB_2 mixtures obtained at the temperatures of 1200–1900 °C

Рис. 1. Дифрактограммы образцов смесей B_4C–25 мол. % TiB_2, полученных при температурах 1200–1900 °С

phase. Its presence is caused by the fact that NFC has aluminum oxide impurity Al_2O_3, which reacts with the components of the batch [20].

Fig. 2 presents the electron micrographs of mixture samples synthesized at the temperatures of 1400, 1650 and 1900 °C. The micrographs were taken in the mode of registration of secondary electrons. The scanning electron microscopy (SEM) images of a sample obtained at $t = 1400$ °C clearly show heterogeneous particles, some of which are fragmented. To clarify their nature, an elemental mapping was performed, which indicated that the particles constituted remains of unreacted NFC (Fig. 3). Besides, the energy- dispersive analysis data revealed the presence of oxygen in the amount of 5 wt. %.

The samples obtained at $t = 1650$ and 1900 °C have aggregated particles with smooth edges, the size of which does not exceed several micrometers. According to the energy-dispersive analysis, these samples contain titanium, boron, carbon, as well as nickel and aluminium (~1 wt. % in total).

The theoretical weight loss of the batch as a result of reaction (3) is 19.05 % at a ratio of reagents corresponding to 25 mol. % of TiB_2 in the resulting powder. The experimental weight loss was 0.9, 1.7, 19.5 and 19.4 % at the processing temperatures of 1200, 1400, 1650 and 1900 °C, respectively. It follows from the obtained results that the reaction of boride formation is fully completed at $t = 1650$ °C.

The results of granulometric analysis of the samples of B_4C –25 mol. % TiB_2 composition synthesized at $t = 1650$ and 1900 °C showed that the average particle size of the obtained powders increases from 8.4 to 9.8 µm upon an increase in the synthesis temperature. Since an increase in the particle size of the powder can lead to adeterioration in its sintering properties, the further experiments at $t = 1650$ °C were conducted.

To evaluate the effect of the mixture composition on the properties of the resulting powder, the batch with the composition corresponding to 10, 20, 25 and

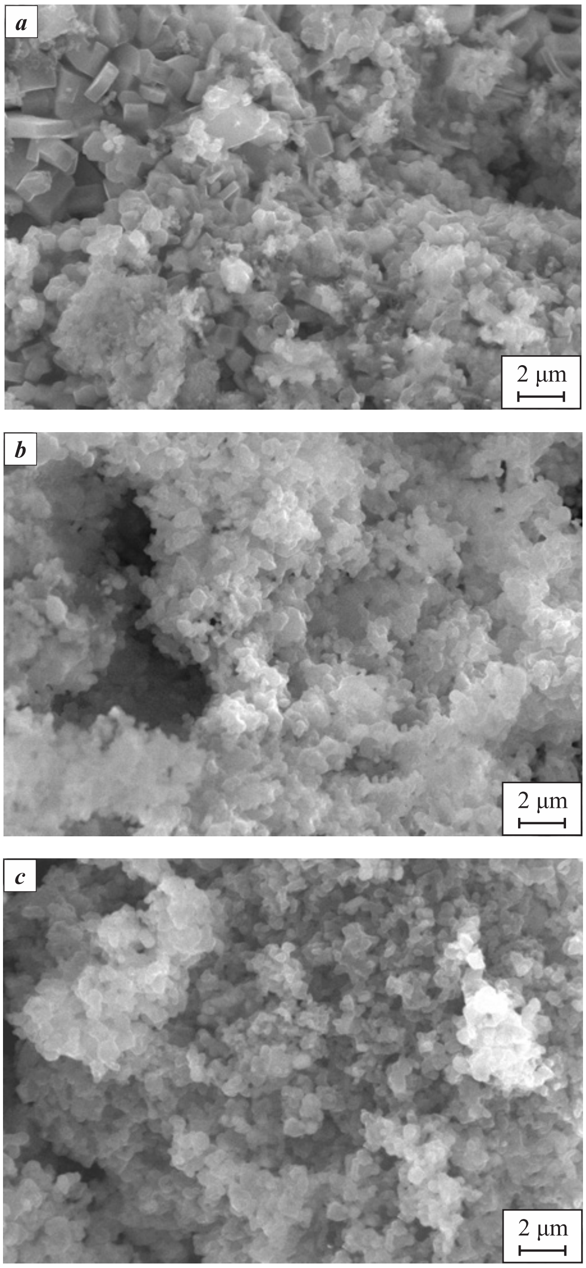

Fig. 2. The SEM images of $B_4C–TiB_2$ powders synthesized at $t = 1400$ °C (***a***), 1650 °C (***b***) and 1900 °C (***c***)

Рис. 2. Снимки РЭМ порошков $B_4C–TiB_2$, синтезированных при $t = 1400$ °С (***a***), 1650 °С (***b***) и 1900 °С (***c***)

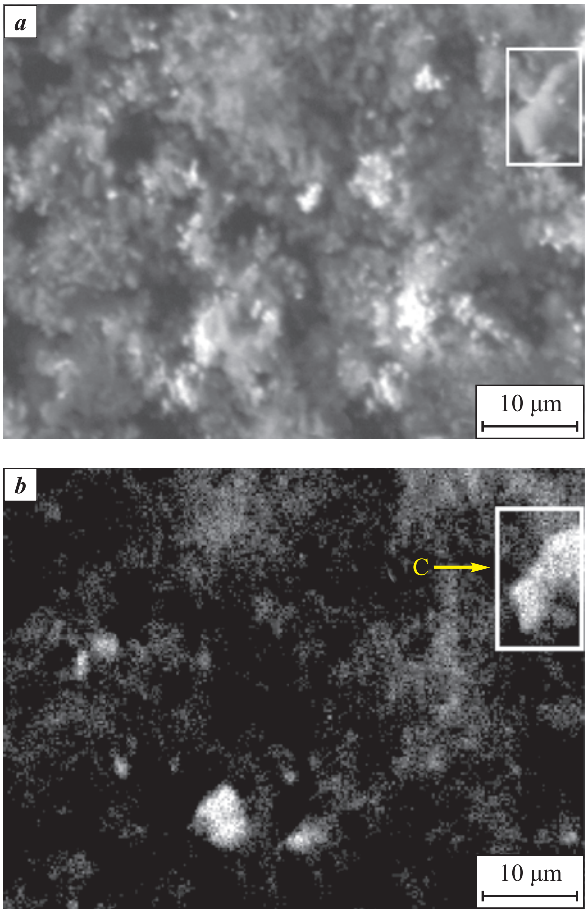

Fig. 3. The micrograph of $B_4C–TiB_2$ powder synthesized at t = 1400 °C (***a***), and the distribution of carbon (***b***)

Рис. 3. Микрофотография порошка $B_4C–TiB_2$, синтезированного при t = 1400 °C (***a***), и распределение углерода (***b***)

30 mol. % of TiB_2 was heat-treated. The experimental weight loss of the batch during the synthesis was close to the theoretical value in all cases (the relative deviation did not exceed 3 %), which indicates the completeness of the synthesis process at t = 1650 °C, regardless of the composition of the sample. This was also confirmed by X-ray phase analysis data (Fig. 4). The diffraction patterns of the condensed reaction products contain TiB_2 and B_4C phases for all samples. The TiB_2 phase content estimated by the corundum number method was 9, 18, 24, and 29 mol. % for T10, T20, T25, and T30 samples, respectively. These data turned out to be close to the estimated values.

From the results of determining the total carbon content, presented in Table 1, it can be seen that the obtained experimental data slightly exceed the values corresponding to the given composition of the synthesized mixtures. This also indicates a complete synthesis process. It should be noted that with an increase in TiB_2 phase content in the powders, the excess of carbon decreases.

Fig. 5 shows the micrographs of the samples of composite powder materials with different TiB_2 contents. All SEM images contain aggregated particles of several micrometers in size, and the absence of fragmented particles indirectly bespeaks of the absence of unreacted particles of the initial components of the reaction mixture.

In the course of particle size analysis, the samples of $B_4C–TiB_2$ powders were subjected to ultrasonic dispersion at a power of 200 W for 30 s. Two peaks were found in the particle size distribution histograms of T10 and T30 samples (Fig. 6), with the second peak increasing upon an increase in TiB_2 phase content. Since the ratio of the heights of the first and the second maxima on the bimodal curve changes with an increase in the concentration of titanium diboride in the synthesized mixture, it can be assumed

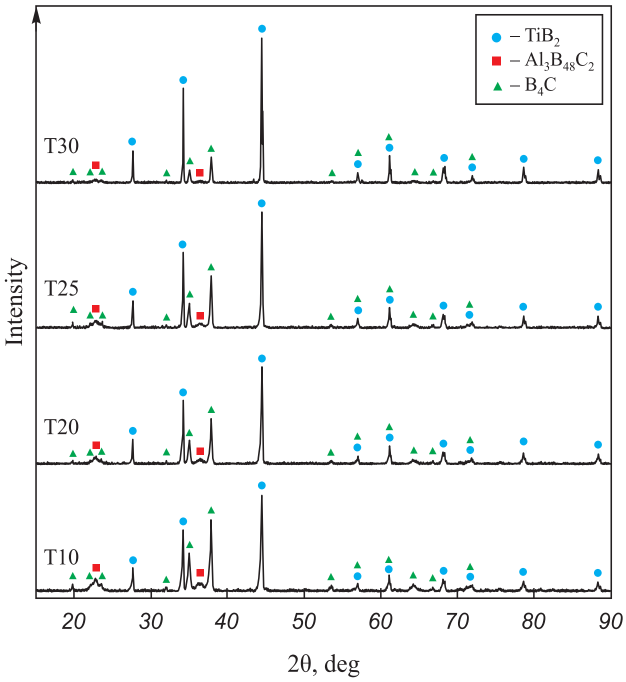

Fig. 4. The diffraction patterns of the samples of powder mixtures containing 10–30 mol. % TiB_2, synthesized at t = 1650 °C

Рис. 4. Дифрактограммы образцов порошковых смесей, содержащих 10–30 мол. % TiB_2, синтезированных при t = 1650 °C

***Table 1.* The results of determining the total carbon content, wt. %**

***Таблица 1.* Результаты определения содержания общего углерода, мас. %**

Sample	Experiment	Calculation
T10	19.7	19.1
T20	16.8	16.5
T25	15.4	15.3
T30	14.2	14.1

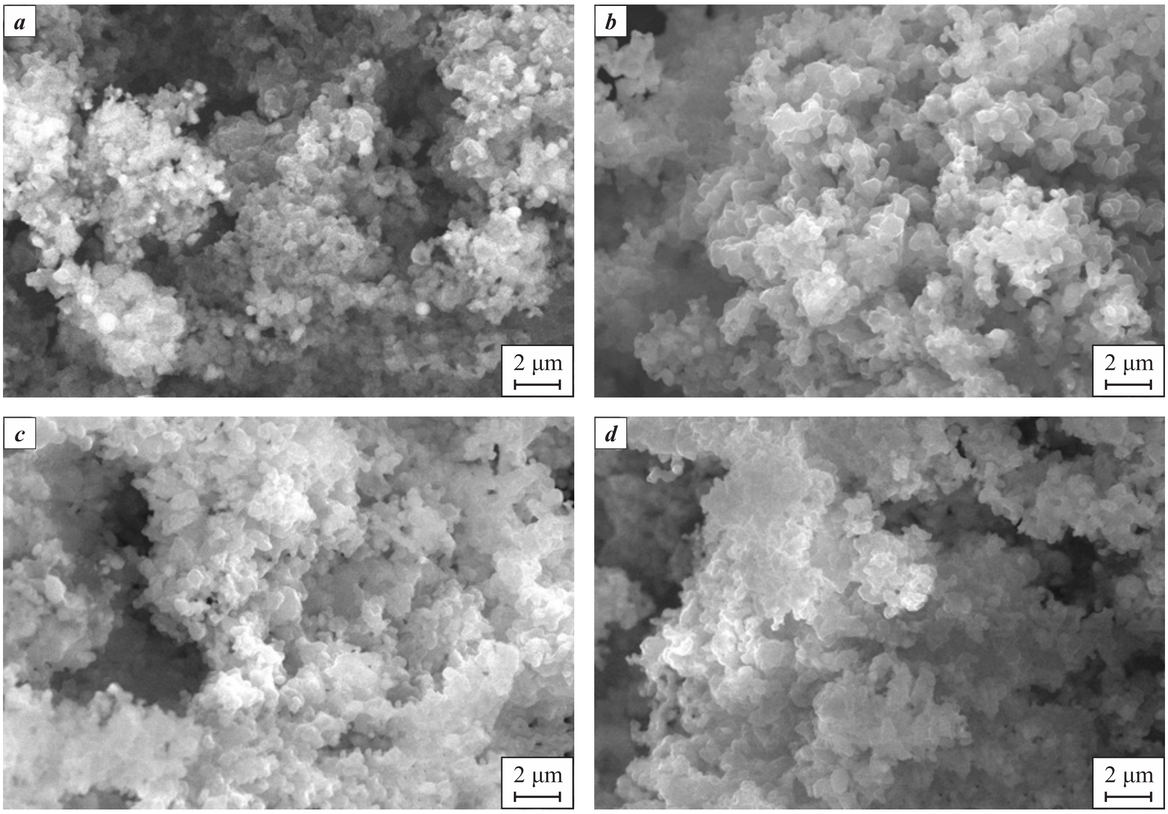

Fig. 5. The micrographs of B_4C–TiB_2 powder synthesized at t = 1650 °C
TiB_2 content, mol. %: 10 (***a***), 20 (***b***), 25 (***c***) and 30 (***d***)

Рис. 5. Микрофотографии образцов порошковых смесей B_4C–TiB_2, синтезированных при t = 1650 °C
Содержание TiB_2, мол. %: 10 (***a***), 20 (***b***), 25 (***c***) и 30 (***d***)

that the part of the histogram with a smaller particle size mainly characterizes the B_4C phase; consequently, its other part with a larger particle size refers to the TiB_2 phase. Based on this assumption, the average size of particles and aggregates was calculated for each phase (Table 2), and the values of standard deviations and asymmetry indices were determined using method [26].

Table 2 shows that the average 50 % particle size increases with an increase in the TiB_2 content of the powders under research. There is also an increase in the particle size of B_4C phase compared to pure B_4C (2.4 μm). The standard deviation values indicate a wide range in particle size distribution, i.e. the powder is polydisperse. The low value of asymmetry degree proves the symmetry of the distribution curves for each phase. The largest value of the average particle size of B_4C and TiB_2 phases is typical for the sample containing 30 mol. % of TiB_2.

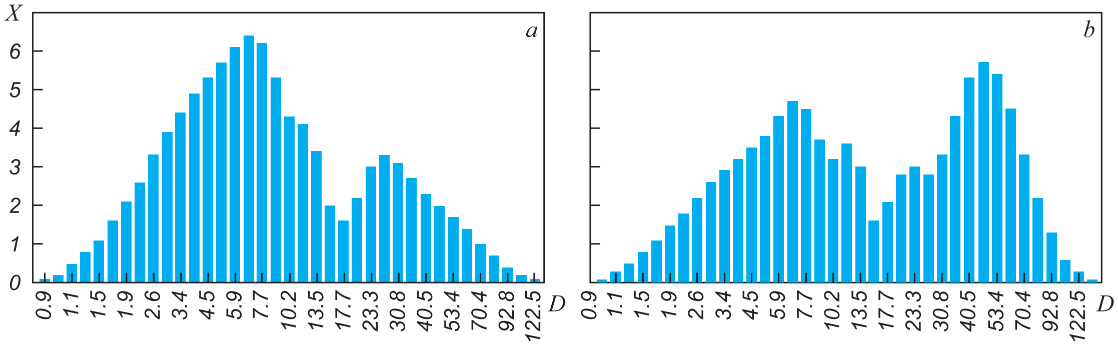

Fig. 6. Particle size distribution histograms for T10 (***a***) and T30 (***b***) samples
X – fraction content, wt. %; D – particle size, μm

Рис. 6. Гистограммы распределения частиц по размерам образцов T10 (***a***) и T30 (***b***)
X – содержание фракции, мас. %; D – размер частиц, мкм

Table 2. **The results of research of particle size of B_4C–TiB_2 powders**

Таблица 2. **Результаты исследования размера частиц порошков B_4C–TiB_2**

Sample	Average size of 50 % of particles D50, μm	Phase	Average size of the phase, μm	Standard deviation, μm	Asymmetry degree
T10	7.4	B_4C	5.3	1.9	–0.050
		TiB_2	33.6	1.6	0.040
T20	8.3	B_4C	5.0	1.9	–0.040
		TiB_2	40.0	1.6	0.010
T25	8.4	B_4C	5.1	1.9	–0.040
		TiB_2	41.0	1.6	–0.023
T30	13.4	B_4C	5.5	1.9	–0.050
		TiB_2	41.9	1.6	–0.005

The surface area values were 5, 4, 3, and 3 m^2/g for T10, T20, T25, and T30 samples, respectively, whereas the said value was 4 m^2/g for the initial boron carbide sample without modifying additives.

In order to determine the thermal-oxidative stability of the obtained B_4C–TiB_2 powders, they were oxidized in a synthetic air atmosphere. Similar thermogravimetric curves were obtained for all samples of different composition. The derivatogram of T10 sample is presented in Fig. 7 as an example.

X-ray phase analysis was conducted to identify the products of oxidation of the mixture with oxygen. The diffraction pattern of the sample of composite powder material after heating up to 1000 °C in an oxidizing atmosphere is shown in Fig. 8.

The results of thermogravimetric analysis show that the weight gain is caused by the oxidation process starting at t ~500 °C. Upon the temperature reaching 1000 °C, there are unoxidized B_4C and TiB_2 phases, as well as $TiBO_3$, TiO_2 and B_2O_3 oxidation products present in the samples. It can be assumed that when this temperature is reached, the process proceeds in accordance with the following reactions

$$(1-x)B_4C + xTiB_2 + (3.5-0.25y)O_2 = \\ = (2-x-0.5y)B_2O_3 + (x-y)TiO_2 + \\ + yTiBO_3 + (1-x)CO, \qquad (4)$$

$$(1-x)B_4C + xTiB_2 + (4-1.5x-0.25y)O_2 = \\ = (2-x-0.5y)B_2O_3 + (x-y)TiO_2 + \\ + yTiBO_3 + (1-x)CO_2. \qquad (5)$$

Upon that, the oxidation of minimum 80 wt. % of composite powder material occurs. The mass fraction of the oxidized substances at t = 1000 °C is 80, 75, 69 and 73 wt. % for T10, T20, T25 and T30 samples, respectively, and 83 wt. % for the initial boron carbide. The incomplete oxidation of the samples can be

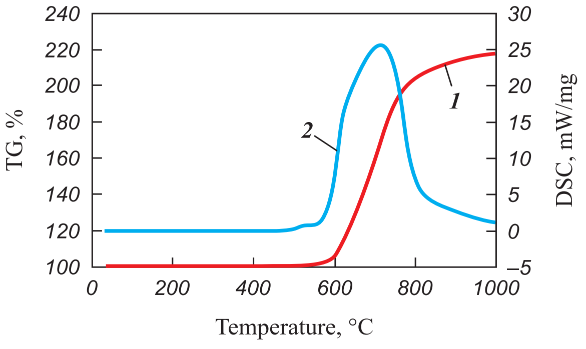

Fig. 7. TG (***1***) and DSC (***2***) curves for B_4C–10 mol. % TiB_2 (T10) sample

Рис. 7. Кривые ТГ (***1***) и ДСК (***2***) образца B_4C–10 мол. % TiB_2 (T10)

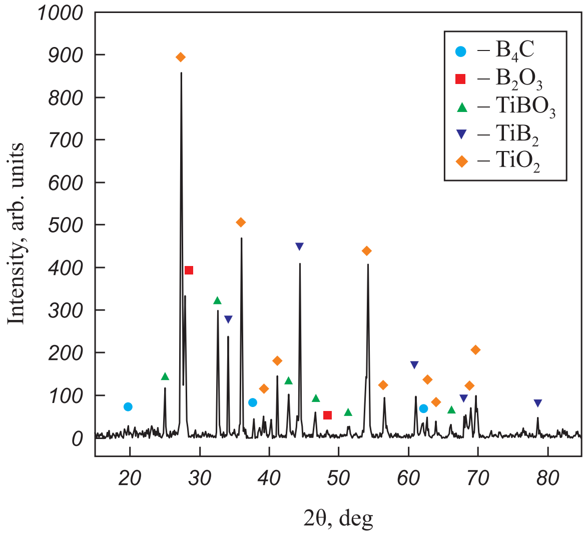

Fig. 8. The diffraction pattern of B_4C–25 mol. % TiB_2 (T25) sample subjected to oxidation in a synthetic oxygen atmosphere at t = 1000 °C

Рис. 8. Дифрактограмма образца B_4C–25 мол. % TiB_2 (T25), подвергнутого окислению в среде синтетического кислорода при t = 1000 °C

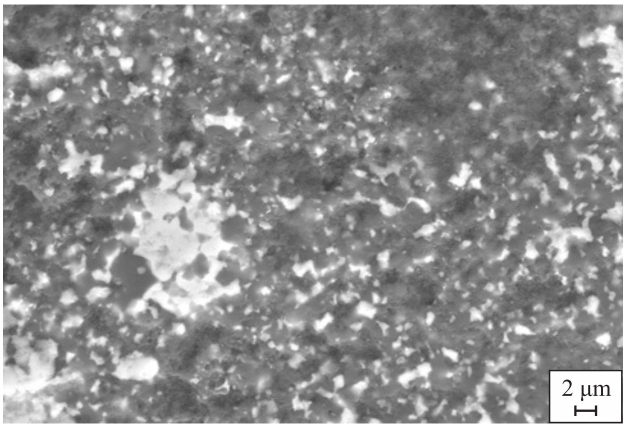

Fig. 9. The microstructure of B_4C–30 mol. % TiB_2 composite ceramics
Gray area – B_4C matrix, light inclusions – TiB_2

Рис. 9. Микроструктура композиционной керамики B_4C–30 мол. % TiB_2
Серые участки – матрица B_4C, светлые включения – TiB_2

explained by the formation of a liquid protective film of B_2O_3, the melting temperature of which is ~450 °C, on the surface of B_4C and TiB_2 particles [27].

The synthesized powder containing 30 mol. % of TiB_2 was selected for the preparation of composite ceramics. The relative density of the obtained material was 99.0±1.1 %, and the relative density of B^4C ceramics produced in a similar way without the use of modifying additives was 97.7±0.5 %.

Thus, the use of a batch with B_4C–30 mol. % TiB_2 composition obtained by carbide reduction allows to produce ceramics with a high relative density. Its structure consists of a boron carbide matrix (gray area) and light inclusions of titanium diboride of various sizes (Fig. 9).

The microhardness of the composite ceramics was 33.0±3.4 GPa, and the fracture toughness was 5.0±0.2 MPa·$m^{0.5}$; for ceramics without TiB_2 additives, these indices were 45.5±5.2 GPa and 3.6±0.11 MPa·$m^{0.5}$, respectively. Thus, the presence of a modifying additive in the composition of ceramics naturally led to a decrease in microhardness and an increase in the material fracture toughness.

Conclusion

B_4C–TiB_2 composite powder materials have been obtained by the carbide reduction of titanium dioxide using an excess of boron carbide and nanofibrous carbon. It has been established that the process of formation of the TiB_2 phase starts at t = 1200 °C, but it is fully completed at 1650 °C. a further increase in a temperature leads to an increase in the particle size of B_4C–TiB_2 powder. The average size of 50 % particles of the composite powder material containing 10–30 mol. % of TiB_2 is 15 µm maximum, and the surface area value does not exceed 5 m^2/g. The average particle size of the B_4C phase is in the range of 5.3–5.5 µm, and that of the TiB_2 phase is 33.6÷41.9 µm.

The oxidation of the obtained mixtures with atmospheric oxygen starts at t ~500 °C. Upon that, maximum 80 wt. % of the powders under study are oxidized when the temperature reaches 1000 °C.

The presence of 30 mol. % of TiB_2 in the composite powder material allows to perform the hot pressing production of the ceramics with a higher relative density (99.0±1.1 %) and fracture toughness (5.0±0.2 MPa·$m^{0.5}$) as compared to the ceramics obtained in a similar way only from B_4C.

References / Список литературы

1. Domnich V., Reynaud S., Haber R.A., Chhowalla M. Boron carbide: Structure, properties, and stability under stress. *Journal of the American Ceramic Society*. 2011;94(11):3605–3628.
https://doi.org/10.1111/j.1551-2916.2011.04865.x
2. Krutskii Y.L., Nepochatov Y.K., Pel' A.N., Skovorodin I.N., Dyukova K.D., Krutskaya T.M., Kuchumova I.D., Mats O.E., Tyurin A.G., Emurlaeva Y.Y., Podryabinkin S.I. Synthesis of polydisperse boron carbide and synthesis of a ceramic on its basis. *Russian Journal of Applied Chemistry*. 2019;92(6):750–758.
https://doi.org/10.1134/S1070427219060041

   Крутский Ю.Л., Непочатов Ю.К., Пель А.Н., Сковородин И.Н., Дюкова К.Д., Крутская Т.М., Кучумова И.Д., Матц О.Э., Тюрин А.Г., Эмурлаева Ю.Ю., Подрябинкин С.И. Синтез полидисперсного карбида бора и получение керамики на его основе. *Журнал прикладной химии*. 2019;92(6):719–727.
https://doi.org/10.1134/S0044461819060045
3. Guo W., Wang A., He Q., Tian T., Liu C., Hu L., Shi Y., Liu L., Wang W., Fu Z. Microstructure and mechanical properties of B_4C–TiB_2 ceramic composites prepared via a two-step method. *Journal of the European Ceramic Society*. 2021;41(14):6952–6961.
https://doi.org/10.1016/j.jeurceramsoc.2021.07.013
4. Rubink W.S., Ageh V., Lide H., Ley N.A., Young M.L., Casem D.T., Faierson E.J., Scharf T.W. Spark plasma sintering of B_4C and B_4C–TiB_2 composites: Deformation and failure mechanisms under quasistatic and dynamic loading. *Journal of the European Ceramic Society*. 2021;41(6):3321–3332.
https://doi.org/10.1016/j.jeurceramsoc.2021.01.044
5. Fahrenholtz W.G., Hilmas G.E. Ultra-high temperature ceramics: Materials for extreme environments. *Scripta Materialia*. 2017;129:94–99.
https://doi.org/10.1016/j.scriptamat.2016.10.018
6. Basu B., Raju G.B., Suri A.K. Processing and properties of monolithic TiB_2 based materials. *International Materials Reviews*. 2006;51(6):352–374.
https://doi.org/10.1179/174328006X102529
7. Golla B.R., Mukhopadhyay A., Basu B. Review on ultra-high temperature boride ceramics. *Progress in Mmaterials*

Science. 2020;111:100651.
https://doi.org/10.1016/j.pmatsci.2020.100651

8. Krutskii Y.L., Bannov A.G., Antonova E.V., Sokolov V.V., Pichugin A.Y., Maksimovskii E.A., Krutskaya T.M., Netskina O.V., Bataev I.A. Synthesis of fine dispersed titanium diboride from nanofibrous carbon. *Ceramics International*. 2017;43(3):3212–3217.
https://doi.org/10.1016/j.ceramint.2016.11.146

9. White R.M., Dickey E.C. Mechanical properties and deformation mechanisms of B_4C–TiB_2 eutectic composites. *Journal of the European Ceramic Society*. 2014;34(9): 2043–2050.
https://doi.org/10.1016/j.jeurceramsoc.2013.08.012

10. Clayton J.D., Rubink W.S., Ageh V., Choudhuri D., Chen R.R., Du J. Scharf T.W. Deformation and failure mechanics of boron carbide–titanium diboride composites at multiple scales. *JOM: the Journal of the Minerals, Metals & Materials Society*. 2019;71:2567–2575.
https://doi.org/10.1007/s11837-019-03548-y

11. Heydari M.S., Baharvandi H.R. Comparing the effects of different sintering methods for ceramics on the physical and mechanical properties of B_4C–TiB_2 nanocomposites. *International Journal of Refractory Metals and Hard Materials*. 2015;51:224–232.
https://doi.org/10.1016/j.ijrmhm.2015.04.003

12. Srivatsan T.S., Guruprasad G., Black D., Radhakrishnan R., Sudarshan T.S. Influence of TiB_2 content on microstructure and hardness of TiB_2–B_4C composite. *Powder Technology*. 2005;159(3):161–167.
https://doi.org/10.1016/j.powtec.2005.08.003

13. Cai K.F., Nan C.W., Schmuecker M., Mueller E. Microstructure of hot-pressed B_4C–TiB_2 thermoelectric composites. *Journal of Alloys and Compounds*. 2003;350(1-2): 313–318. https://doi.org/10.1016/S0925-8388(02)00993-3

14. Wang A., He Q., Guo W., Liu C., Tian T., Hu L., Liu L., Wang W., Fu Z. Microstructure and properties of hot pressed TiB_2 and SiC reinforced B_4C-based composites. *Materials Today Communications*. 2021;26:102082.
https://doi.org/10.1016/j.mtcomm.2021.102082

15. Bogomol .I, Borodianska H., Zhao T., Nishimura T., Sakka Y., Loboda P., Vasylkiv O. a dense and tough (B_4C–TiB_2)–B_4C «composite within a composite» produced by spark plasma sintering. *Scripta Materialia*. 2014;71:17–20. https://doi.org/10.1016/j.scriptamat.2013.09.022

16. Liu Y., Li Z., Peng Y., Huang Y., Huang Z., Zhang D. Effect of sintering temperature and TiB_2 content on the grain size of B_4C–TiB_2 composites. *Materials Today Communications*. 2020;23:100875.
https://doi.org/10.1016/j.mtcomm.2019.100875

17. Nikzad L., Orrù R., Licheri R., Cao G. Fabrication and formation mechanism of B_4C–TiB_2 composite by reactive spark plasma sintering using unmilled and mechanically activated reactants. *Journal of the American Ceramic Society*. 2012;95(11):3463–3471.
https://doi.org/10.1111/j.1551-2916.2012.05416.x

18. Shestakov V.A., Gudyma T.S., Krutskii Y.L., Uvarov N.F., Brester A.E., Skovorodin I.N. Evaluation of the temperature range suitable for the synthesis of B_4C–TiB_2 and B_4C–ZrB_2 powder composite materials. *Inorganic Materials*. 2021;57:481–486.
https://doi.org/10.1134/S0020168521050083

Шестаков В.А., Гудыма Т.С., Крутский Ю.Л., Уваров Н.Ф., Брестер А.Е., Сковородин И.Н. Оценка температурного диапазона процессов синтеза порошковых композиционных материалов B_4C–TIB_2 и B_4C–ZrB_2. *Неорганические материалы*. 2021;57(5):506–511.
https://doi.org/10.31857/S0002337X21050080

19. Gudyma T.S., Krutskii Yu.L., Uvarov N.F., Aparnev A.I. Optimization of the obtaining temperature of powder composite material B_4C–ZrB_2 by the boron carbide method. *MATEC Web of Conferences*. 2021;340:5.
https://doi.org/10.1051/matecconf/202134001028

20. Krutskii Yu.L., Bannov A.G., Sokolov V.V., Dyukova K.D., Shinkarev V.V., Ukhina A.V., Maksimovskii E.A., Krutskaya T.M., Kuvshinov G.G. Synthesis of highly dispersed boron carbide from nanofibrous carbon. *Nanotechnologies in Russia*. 2013;8:191–198.
https://doi.org/10.1134/S1995078013020109

Крутский Ю.Л., Баннов А.Г., Соколов В.В, Дюкова К.Д., Шинкарев В.В., Ухина А.В., Максимовский Е.А., Пичугин А.Ю., Соловьев Е.А., Крутская Т.М., Кувшинов Г.Г. Синтез высокодисперсного карбида бора из нановолокнистого углерода. *Российские нанотехнологии*. 2013;8(3-4):43–48.

21. Kurmashov P.B., Maksimenko V.V., Bannov A.G., Kuvshinov G.G. Horizontal vibrofluidized bed pilot reactor for nanofiber carbon synthesis process. *Khimicheskaya tekhnologiya*. 2013;14(10):635–640. (In Russ.).

Курмашов П.Б., Максименко В.В., Баннов А.Г., Кувшинов Г.Г. Горизонтальный пилотный реактор с виброожиженным слоем для процесса синтеза нановолокнистого углерода. *Химическая технология*. 2013;14(10):635–640.

22. Popov M.V. Improving the efficiency of the process of obtaining a methane-hydrogen mixture by catalytic decomposition of light hydrocarbons: Abstract of the dissertation of PhD. Novosibirsk: NSTU, 2019. 20 p. (In Russ.).

Попов М.В. Повышение эффективности процесса получения метано-водородной смеси каталитическим разложением легких углеводородов: Автореф дис. … канд. техн. наук. Новосибирск: НГТУ, 2019. 20 с.

23. Ordan'yan S.S. Rules for the reactions in B_4C–$Me^{IV–VI}B_2$ systems. *Refractories*. 1993;34:268–271.
https://doi.org/10.1007/bf01293229

24. Elyutin V.P., Pavlov Yu.A., Polyakov V.P., Sheboldaev S.B. Interaction of metal oxides with carbon. Moscow: Metallurgiya, 1976. 360 p. (In Russ.).

Елютин В.П., Павлов Ю.А., Поляков В.П., Шеболдаев С.Б. Взаимодействие окислов металлов с углеродом. М.: Металлургия, 1976. 360 с.

25. Niihara K., Morena R, Hasselman D. Evaluation of K_{1c} of brittle solids by the indentation method with low crack-to-indent ratios *Journal of Materials Science Letters*. 1982;1:13–16. https://doi.org/10.1007/BF00724706

26. Blott S.J., Pye K. GRADISTAT: a grain size distribution and statistics package for the analysis of unconsolidated sediments. *Earth Surface Processes and Landforms*. 2001;26(11):1237–1248. https://doi.org/10.1002/esp.261

27. Samsonov G.V. Physical and chemical properties of oxides: Ref. ed. Moscow: Metallurgiya, 1978. 471 p. (In Russ.).

Самсонов Г.В. Физико-химические свойства окислов: Справ. изд. М.: Металлургия, 1978. 471 с.

Information about the Authors

Tat'yana S. Gudyma – Postgraduate Student of the Department of Chemistry and Chemical Technology, Novosibirsk State Technical University (NSTU)
ORCID: 0000-0002-4724-3371
E-mail: gudymatan@mail.ru

Yurii L. Krutskii – Cand. Sci. (Eng.), Associate Professor of the Department of Chemistry and Chemical Technology, NSTU
ORCID: 0000-0003-2524-4143
E-mail: j_krutskii@rambler.ru

Eugene A. Maximovskiy – Cand. Sci. (Chem.), Senior Researcher of the Laboratory of Functional Films and Coatings, Nikolaev Institute of Inorganic Chemistry, Siberian Branch RAS
ORCID: 0000-0002-1555-2719
E-mail: eugene@niic.nsc.ru

Nina Yu. Cherkasova – Cand. Sci. (Eng.), Junior Research of the Research Laboratory of Physicochemical Technologies and Functional Materials, NSTU
ORCID: 0000-0002-5603-7852
E-mail: cherkasova.2013@corp.nstu.ru

Nikita I. Lapekin – Student of the Department of Materials Science in Mechanical Engineering, NSTU
E-mail: lapekin21@mail.ru

Tat'yana V. Larina – Cand. Sci. (Phys.-Math.), Senior Researcher of the Department for Catalytic Studies, Boreskov Institute of Catalysis, Siberian Branch RAS
ORCID: 0000-0002-8020-5270
E-mail: larina@catalysis.ru

Сведения об авторах

Татьяна Сергеевна Гудыма – аспирант кафедры химии и химической технологии, Новосибирский государственный технический университет (НГТУ)
ORCID: 0000-0002-4724-3371
E-mail: gudymatan@mail.ru

Юрий Леонидович Крутский – к.т.н., доцент кафедры химии и химической технологии, НГТУ
ORCID: 0000-0003-2524-4143
E-mail: j_krutskii@rambler.ru

Евгений Анатольевич Максимовский – к.х.н., ст. науч. сотрудник лаборатории функциональных пленок и покрытий, Институт неорганической химии им. А.В. Николаева (ИНХ) СО РАН
ORCID: 0000-0002-1555-2719
E-mail: eugene@niic.nsc.ru

Нина Юрьевна Черкасова – к.т.н., мл. науч. сотрудник научно-исследовательской лаборатории физико-химических технологий и функциональных материалов, НГТУ
ORCID: 0000-0002-5603-7852
E-mail: cherkasova.2013@corp.nstu.ru

Никита Игоревич Лапекин – студент кафедры материаловедения в машиностроении, НГТУ
E-mail: lapekin21@mail.ru

Татьяна Викторовна Ларина – к.ф-м.н., ст. науч. сотрудник отдела исследования катализаторов, Институт катализа им. Г.К. Борескова СО РАН
ORCID: 0000-0002-8020-5270
E-mail: larina@catalysis.ru

Contribution of the Authors

T. S. Gudyma – formation of the main concept, goal and objectives of the study; writing the text, formulation of the conclusions, conducting the calculations, testing the samples

Yu. L. Krutskii – preparation and management of the experiments, provision of the resources.
E. A. Maksimovskiy – conducting the experiments, processing of the research results.
N. Yu. Cherkasova – conducting the calculations, writing the text, testing the samples.
N. I. Lapekin – conducting the calculations, analysis of the research results.
T. V. Larina – scientific guidance, correction of the text and conclusions.

Вклад авторов

Т. С. Гудыма – формирование основной концепции, постановка цели и задачи исследования, подготовка текста, формулировка выводов, проведение расчетов, испытаний образцов, подготовка текста статьи.
Ю. Л. Крутский – подготовка эксперимента, руководство проведением эксперимента, обеспечение ресурсами.
Е. А. Максимовский – проведение экспериментов, обработка результатов исследований.
Н. Ю. Черкасова – проведение расчетов, испытаний образцов, подготовка текста статьи.
Н. И. Лапекин – проведение расчетов, анализ результатов исследований.
Т. В. Ларина – научное руководство, корректировка текста, корректировка выводов.

Received 14.06.2022
Revised 13.10.2022
Accepted 17.10.2022

Статья поступила 14.06.2022 г.
Доработана 13.10.2022 г.
Принята к публикации 17.10.2022 г.

Refractory, Ceramic, and Composite Materials
Тугоплавкие, керамические и композиционные материалы

UDC 621.762

https://doi.org/10.17073/1997-308X-2023-2-46-52

Research article
Научная статья

Core/rim microstructure of Ti(C, N) cermets with low nickel-molybdenum binder content

I. G. Grigorov, **V. A. Zhilyaev**

Institute of solid state chemistry, Ural branch of the Russian Academy of Sciences
91 Pervomayskaya Str., Yekaterinburg 620990, Russia

igor.grigorov2012@yandex.ru

Abstract. We investigated the influence of the basic component concentration on the microstructure of the KNT3 and KNT3 tungsten-free hard alloys (TFHA), focusing on ceramic-metal samples (cermets) with a low nickel-molybdenum binder content. The microstructure of the sintered cermets was analyzed using reflected electron images of thin sections obtained with a scanning electron microscope. Our analusis revealed that the KNT alloy exhobits a core/rim structure (CRM). We observed that decreasing the Ni–Mo binder content leads to a significantincrease in the rim size isurrounding the Ti(C, N) core in the sintered alloy. We also investigated the effect of the plasticizer on the formation of the core/rim microstructure with a low binder content. Furthermore, we found that the absence of nitrogen-enriched areas in the Ti(C, N) grains increases the molybdenum diffusion rate across the refractory phase interfaces during the cooling stage, resulting in a higher specific volume fraction of the shell in the cermet microstructure.

Keywords: thin shell micrography, cermets, titanium carbonitride (Ti(CN)), nickel-molybdenum binder, plasticizer

For citation: Grigorov I.G., Zhilyaev V.A. Core/rim microstructure of Ti(C, N) cermets with low nickel-molybdenum binder content. *Powder Metallurgy and Functional Coatings*. 2023;17(2):46–52.
https://doi.org/10.17073/1997-308X-2023-2-46-52

Микроструктура ядро/обод в керметах Ti(C, N) при дефиците никель-молибденовой связки

И. Г. Григоров, **В. А. Жиляев**

Институт химии твердого тела Уральского отделения РАН
Россия, 620990, г. Екатеринбург, ул. Первомайская, 91

igor.grigorov2012@yandex.ru

Аннотация. По результатам, полученным ранее в работах по безвольфрамовым твердым сплавам (БВТС) марок КНТ3 и КНТ7, проведен анализ влияния компонентов, составляющих их основу, на конечное формирование микроструктуры сплавов. Исследования проводились на керамико-металлических образцах (керметах) при дефиците связующей фазы из никеля с молибденом. Для анализа микроструктуры керметов были использованы изображения поверхности их шлифов, полученных с помощью растровой электронной микроскопии в режиме отраженных электронов. Показано, что особенностью микроструктуры сплавов серии КНТ является наличие у них структуры ядро/обод (Core/Rim Structure – CRM). Анализ выявил, что с уменьшением в БВТС серии КНТ содержания связующей фазы из Ni–Mo заметно увеличился размер обода в спеченном сплаве вокруг ядра из Ti(C, N). Дополнительно рассмотрена роль пластификатора в процессе формирования микроструктуры ядро/обод БВТС серии КНТ при дефиците связующей фазы. По результатам исследования микроструктуры керметов сделаны выводы, которые позволяют предположить, что в отсутствие зон, обогащенных азотом, возрастает вероятность диффузии молибдена через межфазные границы тугоплавких фаз. Следствием этого является увеличение параметра удельной объемной доли оболочки в микроструктуре кермета.

Ключевые слова: анализ изображения шлифов, керметы, карбонитрид титана (Ti(CN)), никель-молибденовая связка, пластификатор

Для цитирования: Григоров И.Г., Жиляев В.А. Микроструктура ядро/обод в керметах Ti(C, N) при дефиците никель-молибденовой связки. *Известия вузов. Порошковая металлургия и функциональные покрытия*. 2023;17(2):46–52. https://doi.org/10.17073/1997-308X-2023-2-46-52

Introduction

The KNT series of tungsten-free hard alloys (TFHA) are composed of titanium carbonitride Ti(C, N) and nickel and molybdenum powders as fusible binders. These alloys can be used as an alternative to tungsten carbide hard alloys. The KNT alloys exhibit unique properties that distinguish them from other TFHAs including high hardness and low specific gravity. For example, the widely used KNT16 alloy (GOST 26530-85) has a hardness of 89 HRA and a density of 5.9 g/cm^3 [1–4].

The titanium carbonitride-based cermet offers several advantages, such as its easy availability and simple manufacturing. Moreover it exhibit higher hardness at high temperatures compared to tungsten carbide, along with superior scale resistance. Additionally, a thin oxide film is formed on the surface of the cermet during tool operates at elevated temperatures, which acts as a lubricant. As a result, the KNT alloys exhibit low friction coefficient and good wear resistance. Nonetheless, KNT alloys also possess certain drawbacks, including low impact toughness and thermal conductivity, and a high coefficient of thermal expansion. Consequently, these properties increase the likelihood of cracking when the tool is soldered and sharpened [2].

We developed a TFHA (KNT series) alloy with a reduced amount of No–Mo bonder, to evaluate its suitability as carbide cores for armor-piercing projectiles [3; 5]. These alloy has improved ceramic properties due the presence of a metallic bond improves their [6–12]. The authors presented the sintering conditions, essential TFHA microstructure characteristics, and physical and mechanical properties of the KNT3 and KNT7 alloys [13–15].

The microstructure of the KNT alloy is characterized by a core/rim structure (CRS) [15–20]. The core is comprised of a permanent liquid phase (PLP) consisting of carbonitride $TiC_{1-x}Ni_x$, while the rim (which forms the shell of the core) is a multicomponent carbonitride (Ti, Mo)(C, N). The formation of the cermet microstructure is primarily attributed to the wetting of the solid phase by the molten binder, facilitated by a wetting angle close to zero at the interface between the solid phase and the melt.

The objective of this study is to examine the impact of the carbon-to-nitrogen ratio in the permanent liquid phase (PLP) on the formation of the core/rim structure (CRS).

Alloys with a low binder content

Figure 1 presents composite contrast SEM cross sections of KNT7 and KNT3 alloys. It is apparent from the Fig. 1 that the coaxial shell of the base metal grains, or the rim, around the cermet cores in KNT3 occupies a larger surface area compared to KNT7. This notable difference in the microstructures of KNT3 cermets and conventional hard alloys was previously by Pakholkov V. et al. [3]. The authors suggested variations in the manufacturing process conditions such as sintering temperature and time, as shown in the table, can lead to the formation of different microstructures in cases where the content of the melt liquid phase is inadequate.

The rim (shell) formation by the dissolution-sedimentation reaction [4] is limited by the amount of available molybdenum in the liquid phase. The shell formation may be associated with molybdenum solid-phase mass transfer over the interphase interfaces. There are no available studies of this phenomenon so we decided to investigate the CRS phase and structure formation during the interaction between titanium carbonitride and metallic melts at various stages of sintering.

Formation of CRS ctructure in KNT alloys with a low binder content

The detailed synthesis of KNT3 and KNT7 cermets is presented in references [3; 13]. The values of sintering temperature (t_{sn}) and isothermal holding time (τ_h) for each sample (see the Table) can be attributed to the increased contribution of solid-phase sintering

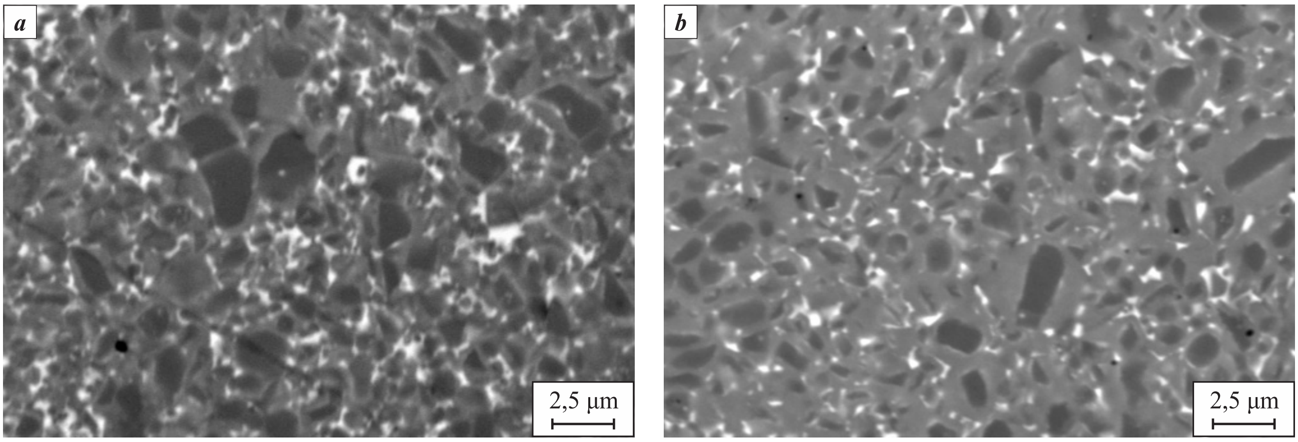

Fig. 1. The core/rim microstructure of KNT7 (***a***) and KNT3 alloys (***b***)
JSM 6390 LA microscope (JEOL Ltd., Japan), ×5000, reflected electron image

Рис. 1. Вид микроструктуры ядро/обод сплавов КНТ7 (***a***) и КНТ3 (***b***)
Микроскоп JSM 6390 LA (JEOL Ltd., Япония), увеличение ×5000, режим съемки – отраженные электроны

Phase composition of the cermets [13]

Фазовый состав исследуемых керметов [13]

Hard alloy grade	Sintering conditions		Content, vol. %		
	t_{sn} ± 10 °C	τ ± 1 %, min	TiC_xN_z core	Rim (Ti, Mo)(C, N)	Ni–Mo binder
KNT7	1480	20	44.64	47.41	6.70
	1480	60	43.95	48.27	6.65
	1500	60	40.42	53.26	6.30
	1520	12	40.97	52.12	6.74
	1520	40	38.64	55.24	6.10
	1520	60	36.67	57.46	5.86
	1540	60	34.06	60.48	5.45
	1560	60	30.89	63.78	5.30
KNT3	1540	20	24.76	72.94	2.22
	1540	60	23.12	74.78	2.02
	1560	60	22.86	75.16	1.94
	1580	60	21.60	76.66	1.70

to cermet formation as the metal component content decreases.

The permanent liquid phase in KNT alloys is titanium carbonitride, which has a double crystal structure consisting of TiC and TiN. Its thermodynamic compatibility with each metal component of the binder phase varies. Cermets are primarily composed on carbon + metal compounds. Nitrogen interacts with metals only at high temperatures and may or may not form weak nitrides. For example, titanium nitride (TiN) is used as an intermediate buffer layer in the electronics industry. It serves as an effective barrier for preventing the diffusion flows between conductive contact components.

The synthesis of the KNT alloy involves three stages of sintering, namely heating, holding at the melting temperature, and cooling in the furnace.

During the heating stage, several reactions take place between the refractory components and the refractory and binder components. These processes occur partially before the liquid phase appears and include gassing, diffusion reactions, and shrinkage of the powder compacts. As the powder mixture is heated, CO is released starting at approximately 900 °C and reaches its maximum release rate at around 1100 °C. Nitrogen is released at ~1200 °C and reaches its maximum release rate at 1300 °C. The nitrogen release rate decreases at temperatures above 1300 °C is associated with the beginning of CRS growth in cermets.

During the the low-temperature sintering phase, the rubber-based plasticizer (4–5 % gasoline solution) [21; 22] is removed before the liquid metal (melt) emerges. Upon decomposition, the plasticizer yields the Mo_2C molybdenum compound, which may account for another characteristic of the shell microstructure. Figure 2 illustrates the two-layer shell structure of the KNT3 cermet, comprising an inner shell consisting of a solid solution rich in heavy elements, that surrounds the Ti(C, N) grain; and an outer shell is Ti-based material.

The last stage of the two-level shell microstructure formation, particularly its onset, remains ambiguous and conflicting. One proposal suggests that the final shell structure is created during the final stage of sintering, whereby TiC and MoC carbide are deposited on the Ti(C, N) particles. These carbides form a solid solution dissolved in the liquid binder. Another proposal assumes that the inner shell is formed by a solid-phase interaction at the initial sintering stage (up to 900 °C), while the outer shell is formed by dissolution/deposition.

The second sintering stage begins with the interaction between the Ni and Mo binders and refractory phases and the emergence of the liquid phase. The dissolution/deposition process becomes a significant contributor to the formation of the sintered cermet microstructure.

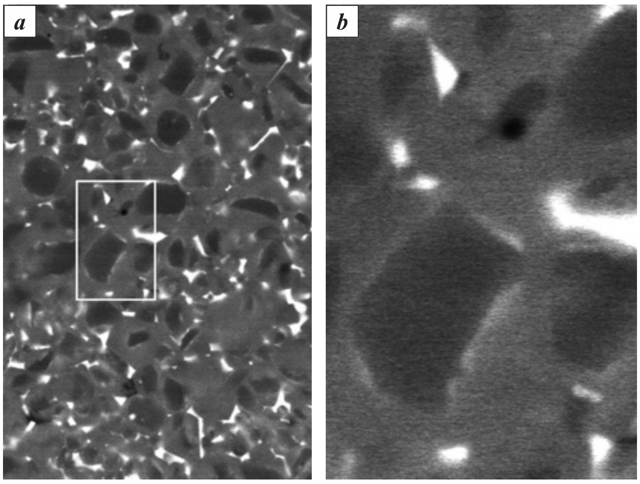

Fig. 2. Two-level microstructure of the KNT3 cermet rim: inner shell (light areas) and outer shell (dark gray areas)
JSM 6390 LA microscope, ×5000 (***a***) and ×20,000 (***b***), reflected electron images

Рис. 2. Вид двухуровневой микроструктуры оболочки (обода) кермета КНТ3: внутренней (светлые участки) и наружной (темно-серые)
Микроскоп JSM 6390 LA, увеличение ×5000 (***a***) и ×20 000 (***b***), режим съемки – отраженные электроны

According to available sources, during the sintering process, Ti(C, N) reacts with the melt such that the liquid molybdenum facilitates the dissolution of titanium and carbon from the PLP, while the nitrogen-rich, poorly soluble carbonitride remains preserved as a solid phase. The enrichment of the refractory phase with titanium nitride is more or less pronounced depending on the liquid/solid phase ratio. The nitrogen-rich areas of the Ti(C, N) grains remain insoluble in the liquid metal bond and act as crystallization nuclei of the (Ti, Mo)C carbide solutions deposited from the melt by dissolution/sedimentation, leading to the formation of the so-called *K*-phase [4].

The formation of the *K*-phase takes place during the liquid-phase sintering of hard alloys in the presence of a carbide-forming element in the melt. As the liquid phase emerges, the TiC component of the PLP begins to dissolve, forming (Ti, Mo)C. The deposition of this compound is possible only when the limit solubility product value $Mo_{1-n}Ti_nC_y$ is reached.

The core size of the Ti(C, N) particles increases with the sintering time primarily due to particle coalescence at their interfaces, which is more intense under liquid-phase sintering than under solid-phase sintering, before the shell structure formation. The rate of shell deposition on the Ti(C, N) grains depends on the sintering temperature and (Ti, Mo)C concentration in the melt. The shell thickness reaches 0.5–3.0 μm as the sintering temperature increases from 1450 to 1540 °C.

Pakholkov V. et al. [3] observed that as the volume fraction of the Ni–Mo binder decreases, the degree of coalescence of the Ti(C, N) grains increases. The specific volume content (V_V) of the Ti shell (rim) consisting of $Ti_{1-x}Mo_xC_yN_z$ exhibits an inverse relationship between the V_V of the shell (as shown in the table) and binder volume, but the reason for this is unclear.

The furnace cooling rate is controlled and does not exceed 10 °C/min to ensure a smooth temperature gradient across the TFHA thickness, thus tavoiding thermal cracking caused by different coefficients of linear thermal expansion of the TFHA components. The shell formation by dissolution-deposition from the melt $(Ti_{1-n}Mo_n)C_x$ in the KNT3 alloy is limited by the volume content of the binder. At the final stage of the CRS formation, significant shell growth can be attributed to a solid-phase molybdenum mass transfer across the TiC_xN_z – $(Ti_{1-n}Mo_n)C_x$ interface [3]. Figure 3 illustrates the CRS difference for KNT7 and KNT3 cermets for identical sintering conditions (t_{sn} = 1560 °C; τ = 60 min).

Conclusions

We have determined that the synthesis of KNT solid alloy can be divided into three stages: heating, holding at the temperature required for melt formation, and cooling in the furnace. Our conclusion can be summarized as follows.

1. We have observed that the decrease in volume fraction of the Ni–Mo metallic binder leads to an increase in the volume fraction of the $Ti_{1-x}Mo_xC_yN_z$.

2. The absence of nitrogen-enriched areas in the Ti(C, N) grains leads to an increase in the diffusion rate of molybdenum across the refractory phase interfaces during the cooling stage.

3. We have discovered a two-level structure of the cermet shell with inner and outer layers. The inner shell (appearing as light areas in the SEM image) is molybdenum-rich, while the outer shell is Ti-rich (appearing as dark gray areas).

4. We propose a chemical explanation for the formation of the inner cermet shell as a result of the decomposition of the rubber-based plasticizer (4–5 % gasoline solution) during the heating stage.

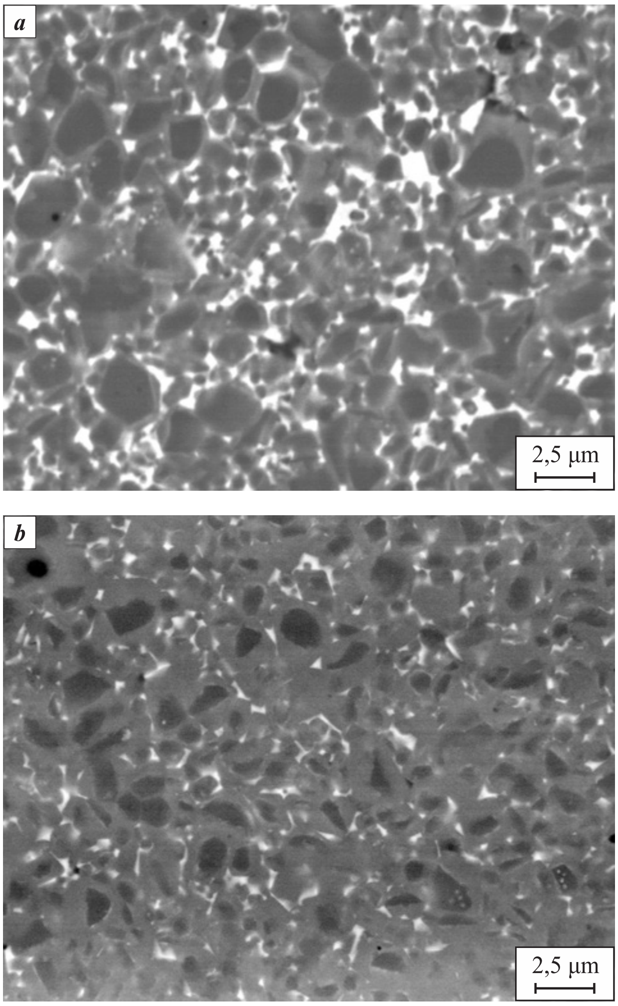

Fig. 3. Microstructure of KNT7 (***a***) and KNT3 (***b***) cermets
JSM 6390 LA microscope, ×3000, t_{sn} = 1560 °C, τ = 60 min, reflected electron images

Рис. 3. Вид микроструктуры керметов марок КНТ7 (***a***) и КНТ3 (***b***)
Микроскоп JSM 6390 LA, увеличение ×3000, $t_{сп}$ = 1560 °C, τ = 60 мин, режим – отраженные электроны

References / Список литературы

1. Panov V.S., Chuvilin A.M. Technology and properties of sintered hard alloys and products from them. Moscow: MISIS, 2001. 426 p. (In Russ.).

   Панов В.С., Чувилин А.М. Технология и свойства спеченных твердых сплавов и изделий из них. М.: МИСИС, 2001. 426 с.

2. Yanushkin A.S., Yakimov S.A., Petrov I.P., Arkhipov P.V. Studies of the surface of tungsten-free hard alloys ground by the combined method. *Nauchnyi zhurnal Bratskogo gosudarstvennogo universiteta*. 2009;(2):70–77. (In Russ.).

   Янюшкин А.С., Якимов С.А., Петров И.П., Архипов П.В. Исследования поверхности безвольфрамовых твердых сплавов, шлифованного комбинированным методом. *Научный журнал Братского государственного университета*. 2009;(2):70–77.

3. Pakholkov V.V., Melnikov B.V., Grigorov I.G., Zainulin Yu.G., Alyamovsky S.I. Features of the formation of the microstructure of hard alloys based on $TiC_{0.5}N_{0.47}$ with a deficiency of nickel–molybdenum bond. *Neorganicheskie materialy*. 1990;26(2):292–296. (In Russ.).

   Пахолков В.В., Мельников Б.В., Григоров И.Г., Зайнулин Ю.Г., Алямовский С.И. Особенности формирования микроструктуры твердых сплавов на основе $TiC_{0,5}N_{0,47}$ при дефиците никель – молибденовой связки. *Неорганические материалы*. 1990;26(2):292–296.

4. Zhilyaev V.A., Patrakov E.I. Regularities of the contact interaction of double carbides $(Ti_{1-n}Me_n)C$ with nickel. *Russian Journal of Non-Ferrous Metals*. 2015;56(3):329–332. https://doi.org/10.3103/S1067821215030232

   Жиляев В.А., Патраков Е.И. Кинетика и механизм контактного взаимодействия карбонитрида титана с Ni–Mo-расплавом. *Известия вузов. Порошковая металлургия и функциональные покрытия*. 2015;(2):30–37. https://doi.org/10.17073/1997-308X-2015-2-30-37

5. Kieffer R., Benesovsky F. Hard alloys. (Translated from German). Moscow: Metallurgiya. 1971. 392 p. (In Russ.).

   Киффер Р., Бенезовский Ф. Твердые сплавы. Перевод с нем. М.: Металлургия, 1971. 392 с.

6. Bolognini S., Feusier G., Mari D., Viatte T., Benoit W. TiMoCN-based cermets: high-temperature deformation.

International journal of refractory metals and hard materials. 2003;21(1–2):19–29.
https://doi.org/10.1016/S0263-4368(02)00091-4

7. Mari D., Bolognini S., Feusier G., Cutard T., Verdon C., Viatte T., Benoit W. TiMoCN based cermets: Part I. Morphology and phase composition. *International Journal of Refractory Metals and Hard Materials*. 2003;21(1):37–46. https://doi.org/10.1016/S0263-4368(03)00010-6
8. Mari D., Bolognini S., Feusier G., Cutard T., Viatte T., Benoit W. TiMoCN based cermets Part II. Microstructure and room temperature mechanical properties. *International Journal of Refractory Metals and Hard Materials*. 2003;21(1):47–53.
https://doi.org/10.1016/S0263-4368(03)00011-8
9. Zhou S., Zhao W., Xiong W. Microstructure and properties of the cermets based on Ti(C, N). *International Journal of Refractory Metals and Hard Materials*. 2009;27(1):26–32. https://doi.org/10.1016/j.ijrmhm.2008.01.011
10. Bellosi A., Calzavarini R., Faga M.G., Monteverde F., Zancolo C., D'Errico G.E. Characterization and application of titanium carbonitride-based cutting tools. *Journal of Materials Processing Technology*. 2003;143-144:527–532.
https://doi.org/10.1016/S0924-0136(03)00339-X
11. Xiong J., Guo Z., Wen B., Li C., Shen B. Microstructure and properties of ultra-fine $TiC_{0.7}N_{0.3}$ cermet. *Materials Science and Engineering: A*. 2006;416(1-2):51–58.
https://doi.org/10.1016/j.msea.2005.08.060
12. Peng Y., Miao H., Peng Z. Development of TiCN-based cermets: Mechanical propertiesand wear mechanism. *International Journal of Refractory Metals and Hard Materials*. 2013;39:78–89.
https://doi.org/10.1016/j.ijrmhm.2012.07.001
13. Grigorov I.G., Zhilyaev V.A., Ermakov A.N., Zainulin Yu.G., Shveykin G.P. On the methodology of forecasting some physical and mechanical properties of kermets. *Materialovedenie*. 2004;(8):14–20. (In Russ.).

    Григоров И.Г., Жиляев В.А., Ермаков А.Н., Зайнулин Ю.Г., Швейкин Г.П. О методике прогнозирования некоторых физико-механических свойств керметов. *Материаловедение*. 2004;(8):14–20.
14. Grigorov I.G., Zainulin Y.G. Analysis of fracture of metal ceramic hard alloys of KNT brand. *Materialovedenie*. 2019;10(4):987–994. (In Russ.).

    Григоров И.Г., Зайнулин Ю.Г. Анализ изломов металлокерамических твердых сплавов марки КНТ. *Материаловедение*. 2019;(2):17–24.
15. Grigorov I.G., Zainulin Y.G., Shveykin G.P. Fractal analysis of fracture of powder metallurgical hard alloy. *Materialovedenie*. 2017;8(1):67–74. (In Russ.).

    Григоров И.Г., Зайнулин Ю.Г., Швейкин Г.П. Фрактальный анализ разрушения металлокерамических твердых сплавов. *Материаловедение*. 2016;(6):16–22.
16. Li P., Ye J., Liu Y., Yang D., Yu H. Study on the formation of core–rim structure in Ti(CN)-based cermets. *International Journal of Refractory Metals and Hard Materials*. 2012;35:27–31.
https://doi.org/10.1016/j.ijrmhm.2012.03.012
17. Ahn S., Kang S. Formation of core/rim structures in Ti(C,N)–WC–Ni cermets via a dissolution and precipitation process. *Journal of the American Ceramic Society*. 2000;83(6):1489–1494.
https://doi.org/10.1111/j.1151-2916.2000.tb01415.x
18. Kim S., Min K., Kang S. Rim structure in $Ti(C_{0.7}N_{0.3})$–WC–Ni cermets. *Journal of the American Ceramic Society*. 2003;86(10):1761–1766.
https://doi.org/10.1111/j.1151-2916.2003.tb03551.x
19. Bellosi A., Medri V., Monteverde F. Processing and properties of Ti(C,N)–WC-based materials. *Journal of the American Ceramic Society*. 2001;84(11):2669–2676.
https://doi.org/10.1111/j.1151-2916.2001.tb01069.x
20. Zheng Y., Lin W., Wang S., Xiong W. Effect of carbont on the microstructure and mechanical properties of Ti(C, N)-based cermets. *Ceramics International*. 2004;30(8): 2111–2115. https://doi.org/10.1016/j.ceramint.2003.11.016
21. Ermakov A.N., Grigorov I.G., Ermakova O.N., Pushin V.G., Zainulin Yu.G. Influence of plasticizer on microstructure and properties of titanium carbonitride – titanium nickelide system. *Perspetkivnye materialy*. 2006;(5):42–48. (In Russ.).

    Ермаков А.Н., Григоров И.Г., Ермакова О.Н., Пушин В.Г., Зайнулин Ю.Г. Влияние пластификатора на микроструктуру и свойства системы карбонитрид титана – никелид титана. *Перспективные материалы*. 2006;(5):42–48.
22. Grigorov I.G., Zhilyaev V.A., Ermakov A.N., Zainulin Yu.G. The effect of plasticizer on the microstructure of an alloy based on carbonitride and titanium nickelide. *Konstruktsii iz kompozitsionnykh materialov*. 2006;(4): 46–49. (In Russ).

    Григоров И.Г., Жиляев В.А., Ермаков А.Н., Зайнулин Ю.Г. Влияние пластификатора на микроструктуру сплава на основе карбонитрида и никелида титана. *Конструкции из композиционных материалов*. 2006;(4):46–49.

Information about the Authors

Igor' G. Grigorov – Cand. Sci. (Chem.), Research Scientist of Laboratory of Structural and Phase Analysis, Institute of Solid State Chemistry, Ural Branch of the Russian Academy of Sciences (ISSC UB RAS)
ORCID: 0000-0003-1906-7654
E-mail: igor.grigorov2012@yandex.ru

Viktor. A. Zhilyaev – Dr. Sci. (Eng.), ISSC UB RAS

Сведения об авторах

Игорь Георгиевич Григоров – к.х.н., вед. науч. сотрудник лаборатории структурного и фазового анализа, Институт химии твердого тела УрО РАН (ИХТТ УрО РАН)
ORCID: 0000-0003-1906-7654
E-mail: igor.grigorov2012@yandex.ru

Виктор Александрович Жиляев – д.т.н., ИХТТ УрО РАН

Contribution of the Authors

I. G. Grigorov – basic concept, problem statement, paper authoring, conclusions.

V. A. Zhilyaev – research supervision, article proofreading, editing the conclusions.

Вклад авторов

И. Г. Григоров – формирование основной концепции, постановка цели и задачи исследования, подготовка текста, формулировка выводов.

В. А. Жиляев – научное руководство, корректировка текста, корректировка выводов.

Received 26.05.2022
Revised 24.11.2022
Accepted 01.12.2022

Статья поступила 26.05.2022 г.
Доработана 24.11.2022 г.
Принята к публикации 01.12.2022 г.

Nanostructured Materials and Functional Coatings
Наноструктурированные материалы и функциональные покрытия

UDC 621.793: 671.762.4

https://doi.org/10.17073/1997-308X-2023-2-53-61

Research article
Научная статья

Effect of modifiers on the structure formation and properties of nickel-phosphorus coatings applied to powder steels

I. N. Shcherbakov[1], **B. G. Gasanov**[2]

[1] **Don State Technical University**
1 Gagarin square, Rostov-on-Don 344000, Russia
[2] **South Russian State Polytechnic University named after M.I. Platov**
132 Prosveshcheniya st., Rostov reg., Novocherkassk 346428, Russia

bdd-don@mail.ru

Abstract. The paper shows the effect of solution temperature on the deposition rate of applying composite nickel-phosphorus coatings modified with boron nitride and polytetrafluoroethylene to powder samples made of improved P40, P40Kh and P40KhN steels obtained by hot stamping of porous sintered blanks. It has been experimentally established that within the range of 70–90 °C, the average deposition rate of modified BN and $(C_2F_4)n$ coatings is 15–19 μm/h, while the chemical composition of the improved steels and the surface configuration of the samples have no effect on the coating build-up rate. The mechanism of the formation of the structure and properties of nickel-phosphorus coatings (NiPC) without additives and those of NiPC modified with boron nitride and polytetrafluoroethylene during deposition, sintering and running-in is revealed. It has been established that immediately after deposition, Ni–P coating has an amorphous structure with inclusions of nickel particles, and its microhardness does not exceed 380–390 MPa with no modifiers added. In the dry friction mode at the running-in stage, $Ni_{12}P_5$ and Ni_2P phases are formed in the modified Ni–P coatings, allowing to improve their tribological properties, and in the steady-state mode, the phase disordering of the modified NiPC proceeds. It has been experimentally revealed that the coefficient of friction and wear decrease by 1.3 times when only $(C_2F_4)n$ is introduced into Ni–P coating, these indices decrease by 1.6 times when only BN is added, and they decrease almost twice when BN and $(C_2F_4)n$ are introduced together. It has been established that upon the combined (complex) modification of NiPC with BN and $(C_2F_4)n$ after the heat treatment, there is almost no nickel oxide phase, nickel boride of NiB type is formed in the coating during running-in, and its content does not decrease when entering the stationary friction mode, thus increasing tribotechnical properties of the coating. During running-in, the coefficient of friction of Ni–P + BN + $(C_2F_4)n$ coating decreases from 0.28 to 0.19, and the wear rate of such a coating in the stationary friction mode is 1.5 mg/h. The efficiency of applying the antifriction nickel-phosphorus coatings modified with BN + $(C_2F_4)n$ to the products made of the improved structural steels obtained by various methods has been theoretically and experimentally substantiated.

Keywords: nickel-phosphorus coating (NiPC), powder steel, modifier, tribotechnical properties, boron nitride, polytetrafluoroethylene

For citation: Shcherbakov I.N., Gasanov B.G. Effect of modifiers on the structure formation and properties of nickel-phosphorus coatings applied to powder steels. *Powder Metallurgy and Functional Coatings*. 2023;17(2):53–61. https://doi.org/10.17073/1997-308X-2023-2-53-61

Влияние модификаторов на структурообразование и свойства никель-фосфорных покрытий, нанесенных на порошковые стали

И. Н. Щербаков[1] ✉, **Б. Г. Гасанов**[2]

[1] **Донской государственный технический университет**
344000, г. Ростов-на-Дону, пл. Гагарина, 1
[2] **Южно-Российский государственный политехнический университет им. М.И. Платова**
346428, Ростовская обл., г. Новочеркасск, ул. Просвещения, 132

✉ bdd-don@mail.ru

Аннотация. Показано влияние температуры раствора на скорость осаждения композиционных никель-фосфорных покрытий, модифицированных нитридом бора и политетрафторэтиленом, на порошковые образцы из улучшаемых сталей марок П40, П40Х и П40ХН, полученных горячей штамповкой пористых спеченных заготовок. Экспериментально установлено, что в интервале температур 70–90 °С средняя скорость осаждения модифицированных BN- и $(C_2F_4)n$-покрытий составляет 15–19 мкм/ч, а химический состав улучшаемых сталей и геометрия поверхности образцов практически не влияют на скорость их наращивания. Предложен механизм формирования структуры и свойств Ni–P-покрытий без добавок и модифицированных нитридом бора и политетрафторэтиленом в процессах осаждения, спекания и приработки. Установлено, что непосредственно после осаждения Ni–P-покрытие имеет аморфную структуру с включениями частиц никеля, а его микротвердость без добавки модификаторов не превышает 380–390 МПа. На стадии приработки в режиме сухого трения в модифицированных Ni–P-покрытиях образуются фазы $Ni_{12}P_5$ и Ni_2P, позволяющее повысить их трибологические характеристики, а при установившемся режиме в них протекает фазовое разупорядочивание. Экспериментально выявлено, что при введении в Ni–P-покрытие только $(C_2F_4)n$ коэффициент трения и износ снижаются в 1,3 раза, при добавлении одного BN – в 1,6 раза, а при совместном введении BN и $(C_2F_4)n$ – почти в 2 раза. Установлено, что при совместном (комплексном) модифицировании Ni–P-покрытий BN и $(C_2F_4)n$ после термообработки никель практически не окисляется, в процессе приработки в покрытии образуется борид никеля типа NiB, содержание которого при выходе на стационарный режим трения не уменьшается, что стабилизирует триботехнические характеристики покрытия. В процессе приработки коэффициент трения состава покрытия Ni–P + BN + $(C_2F_4)n$ снижается с 0,28 до 0,19, а скорость изнашивания в режиме стационарного трения составляет 1,5 мг/ч. Теоретически и экспериментально обоснована эффективность нанесения антифрикционных никель-фосфорных покрытий, модифицированных BN + $(C_2F_4)n$, на изделия из конструкционных улучшаемых сталей, полученных различными методами.

Ключевые слова: никель-фосфорное покрытие (НФП), порошковая сталь, модификатор, триботехнические свойства, нитрид бора, политетрафторэтилен

Для цитирования: Щербаков И.Н., Гасанов Б.Г. Влияние модификаторов на структурообразование и свойства никель-фосфорных покрытий, нанесенных на порошковые стали. *Известия вузов. Порошковая металлургия и функциональные покрытия*. 2023;17(2):53–61. https://doi.org/10.17073/1997-308X-2023-2-53-61

Introduction

Various methods of modifying and coating structural, tool and special materials to improve their functional properties are known [1–3]. Numerous papers are devoted to studying the effect of the chemical composition, methods and technological parameters of coating of steel products [4–8]. Particular attention is given to the development of new materials and technologies for coating the products of complex configuration, modified with various micro- and nano-additives [9–11]. From a technological point of view, composite nickel-phosphorus coatings (NiPC), which are obtained by chemical deposition [6; 7; 11–14] and characterized by high wear resistance, a relatively low coefficient of friction, the ability to resist significant cyclic contact loads, as well as the possibility of introducing solid lubricants and other modifiers [8–12; 15–17] into the matrix, are attractive.

However, the works devoted to the development of technology for the production of composite NiPC do not sufficiently research the kinetics of structure formation, which is formed both during deposition and sintering and during friction, and will make it possible to predict their properties, develop new materials and explain the physicochemical processes occurring at all stages of the technological process of coating and operation [13–18].

The analysis of the operating conditions of steel products coated with composite NiPC, as well as scientific and technical developments in the field of structural adaptability of materials and coatings upon friction, developed during the creation of self-lubricating materials and coatings, revealed that the structural states of substances, which predetermine the phenomenon of self-organization in dissipative tribological systems, must be considered when developing the ones [10–13; 19–21].

The purpose of this paper was to study the mechanism of structure formation and tribological properties of composite nickel-phosphorus coatings modified with boron nitride and polytetrafluoroethylene $(C_2F_4)n$ applied to the improved powder steels.

Research methods and technology for obtaining samples

Samples 25 mm in diameter and 5 mm in thickness were obtained by sintering and hot stamping of porous blanks of improved P40, P40Kh and P40KhN steels using the technology specified in work [22]. For the purpose of coating, the surface of the steel samples was prepared in accordance with the requirements described in [10–13]. The working solution for the deposition of NiPC composites Ni–P + BN, Ni–P + $(C_2F_4)n$ and Ni–P + BN + $(C_2F_4)n$ was prepared in the sequence described by the authors [11–13].

The thickness of the composite coatings was determined by means of Konstanta K6 thickness gauge (Russia) with ID1 transducer with a maximum error of $\pm 0.01T + 1$ μm. The adhesive strength of NiPC was evaluated by random testing of reference samples in accordance with GOST 9.302-88 "Control Methods: Bending and Tension", using TME-10 tensile machine (Russia). The loading rate was 2 mm/min.

The *X*-ray studies of the samples were performed by means of DRON-1.5 diffractometer. The phase composition of the samples was identified using *X*-ray data published in the reference literature [23] and the methods described in paper [24]. In order to analyze the amorphous component in the coatings, the samples were taken at a rate of 2 °C/min and with a more optimal scale along the intensity axis. The required reference diffraction patterns were obtained by "smearing" of diffraction lines in the patterns of the corresponding crystalline phases, assuming their ultradispersity [24]. During the qualitative phase analysis, in all cases we attempted to describe the composition of the sample by a minimum number of phases.

The *X*-ray microanalysis was conducted by the methods of electron probe research in the Resource Sharing Center of South Russian State Polytechnic University (NPI) named after M.I. Platov, using VEGA II LMU scanning electron microscope (Tescan, Czechia) equipped with INCA ENERGY 450/XT energy-dispersive microanalysis system (OXFORD Instruments Analytical, Great Britain), providing the opportunity of elemental analysis in the range from Na to U.

The pattern of distribution of modifiers in the coating matrix, as well as the particle sizes and phase morphology were studied by means of Epiquant metallographic microscope (Karl Zeiss Jena, Germany).

Microhardness was measured at a load of 0.0981 N (10 Gs) applied for 15 s, using PMT-3 device (Russia) under GOST 9450-76. For the purpose of a more reliable determination of this characteristic, the number of measurements was 30–50 at a coating thickness of 20 μm.

To determine the tribotechnical properties of NiPC, an end friction machine (FGUP OKTB Orion, Russia) was used, allowing to develop the specific loading on the surface of the studied material up to 300 MPa at a sliding speed of 0.048 m/s. The friction area temperature was measured with a thermocouple inserted into the sample at a distance of 0.5 mm from the friction surface track. The overlap coefficient of the rubbing surfaces of the sample and the counterbody was 0.2. The washers made of steel 45 with a hardness of 48–52 HRC and a roughness of $R_a = 0.25$ μm were used as a counterbody.

Research findings and discussion

The operational reliability of the parts of friction units, to which the composite coatings are applied, largely depends on the uniformity of their thickness and adhesion to the substrate. As shown by the experimental results presented in Figure 1, the process of NiPC formation is initiated when the samples (solution) are heated above 35–40 °C, the coating growth rate increases more intensively with increasing temperature from 60 to 90 °C and reaches 14–18 μm/h depending on the chemical composition (see Figure 1). The highest deposition rate (18–19 μm/h) is observed when applying Ni–P + BN + $(C_2F_4)n$ coating at a temperature of 900 °C.

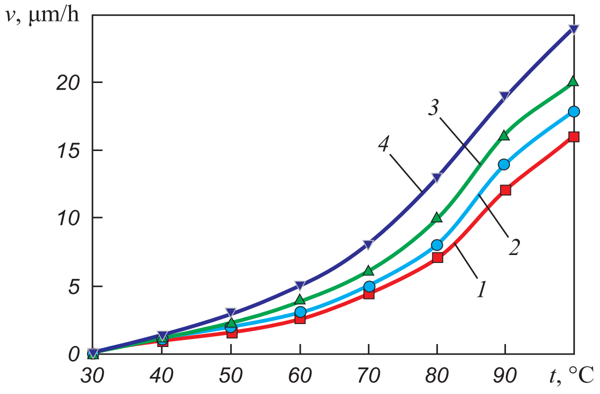

Fig. 1. The dependence of the coating deposition rate on the solution temperature and chemical composition
1 – Ni–P, ***2*** – Ni–P + $(C_2F_4)n$, ***3*** – Ni–P + BN, ***4*** – Ni–P + BN + $(C_2F_4)n$

Рис. 1. Зависимость скорости осаждения покрытия от температуры раствора и химического состава
1 – Ni–P, ***2*** – Ni–P + $(C_2F_4)n$, ***3*** – Ni–P + BN, ***4*** – Ni–P + BN + $(C_2F_4)n$

The studies revealed that Ni–P coating exhibits an amorphous structure immediately after deposition, and its microhardness reaches the maximum of 380–390 HV (Table 1) without modifying additives. When introducing $(C_2F_4)n$, the microhardness of the coating slightly decreases, since it is lower for this polymer than for NiPC. If the coating is modified with boron nitride, its microhardness increases up to 490–500 HV (see Table 1). This can be explained by the nature of the disperse BN phase, which is characterized by a higher hardness than Ni–P coating. The microhardness of Ni–P + BN + (C_2F_4) n composition is slightly lower than that of NiPC modified with BN.

To improve the tribotechnical properties of NiPC and the strength of adhesion to the steel substrate, the coated samples were heated within the range of $t = 50 \div 700$ °C with a spacing of 50 °C for 1 h. At the first stage, the effect of heating temperature on the microhardness of the samples was studied. As can be seen in Fig. 2, the *HV* behavior is the same for all types of coatings, depending on the sintering temperature of the samples. Table 2 provides the critical sintering temperatures and holding time at which the coatings modified with various additives exhibit the maximum microhardness.

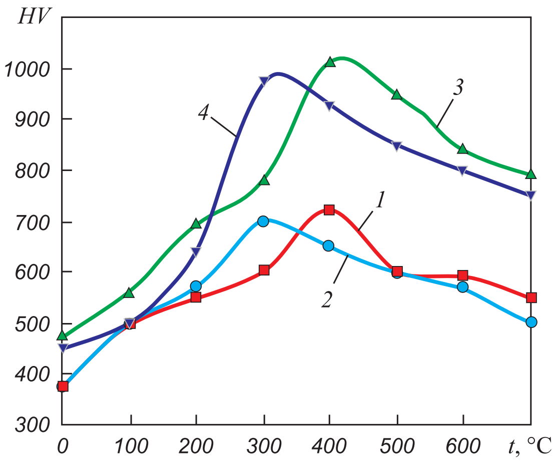

Fig. 2. The dependence of microhardness of NiPC on P40KhN steel on sintering temperature and composition
1 – Ni–P, ***2*** – Ni–P + $(C_2F_4)n$, ***3*** – Ni–P + BN, ***4*** – Ni–P + BN + $(C_2F_4)n$

Рис. 2. Зависимость микротвердости НФП на стали П40ХН от температуры спекания и состава
1 – Ni–P, ***2*** – Ni–P + $(C_2F_4)n$, ***3*** – Ni–P + BN, ***4*** – Ni–P + BN + $(C_2F_4)n$

In particular, the microhardness of the samples made of P40KhN steel coated with Ni–P + $(C_2F_4)n$, sintered at $t = 360$ °C for 1 h, was 700 HV (Fig. 2, curve *2*), while the microhardness of the samples made of P40KhN steel coated with Ni–P + BN + $(C_2F_4)n$ increased up to 980–990 HV (Fig. 2, curve *4*). The maximum *HV* values were obtained for Ni–P and Ni–P–BN coatings after the sintering of the samples at $t = 400$ °C (Fig. 2, curves *1* and *3*).

The studies revealed that composite NiPC are brittle and flake off easily after deposition, and the strength of their adhesion to the substrate is very low. Upon sintering, the samples coated with NiPC within the range of $t = 500 \div 700$ °C, nickel and steel interdiffusion occurs at steel–coating interface and a transitional diffusion layer, contributing to an increase in the strength of adhesion of the coating to the substrate, forms (Fig. 3). Upon that, the chrome content of NiPC does not exceed the measurement error (see Fig. 3, *b*).

The qualitative assessment of the adhesion strength of composite NiPC was performed by bending method (10 samples for each coating). The studies showed no flaking of the coating on the surface of P40KhN steel at the point of fracture, however, noticeable cracks appeared in Ni–P + $(C_2F_4)n$ coating on the surfaces of P40 and P40Kh steels upon bending.

The results of studies performed by means of UMM-5 tensile machine (Fig. 4) showed that the mass loss of coatings of all non-sintered samples without sintering was as follows, g: Ni–P – 0.085; Ni–P + $(C_2F_4)n$ – 0.092; Ni–P + BN – 0.045 and Ni–P + BN + $(C_2F_4)n$ – 0.050. The flake off masses of the samples with Ni–P + BN + $(C_2F_4)n$ coatings are virtually identical, but they are 30–35 % less compared to those with Ni–P.

Upon an increase in the temperature of sintering of the samples made of P40Kh steel from 50 to 350 °C with the holding time of 1 h, the amount of flaking off Ni–P coating decreases from 90 to 25 mg, and the one of Ni–P + BN decreases from 42 to 9 mg (see Fig. 4,

Table 1. **The microhardness of coatings in amorphous state**

Таблица 1. **Микротвердость покрытий в аморфном состоянии**

Coating composition	Micro-hardness $HV_{0.01/15}$	Standard deviation, %
Ni–P	380–390	7
Ni–P + $(C_2F_4)n$	370–375	9
Ni–P + BN	490–500	8
Ni–P + BN + $(C_2F_4)n$	450–460	9

Table 2. **The modes of sintering of samples made of P40Kh steel coated with different compositions**

Таблица 2. **Режимы спекания образцов из стали П40Х с покрытиями различного состава**

Coating composition	*t*, °C	Heat treatment time, min
Ni–P	400	90
Ni–P + $(C_2F_4)n$	360	60
Ni–P + BN	400	90
Ni–P + BN + $(C_2F_4)n$	360	90

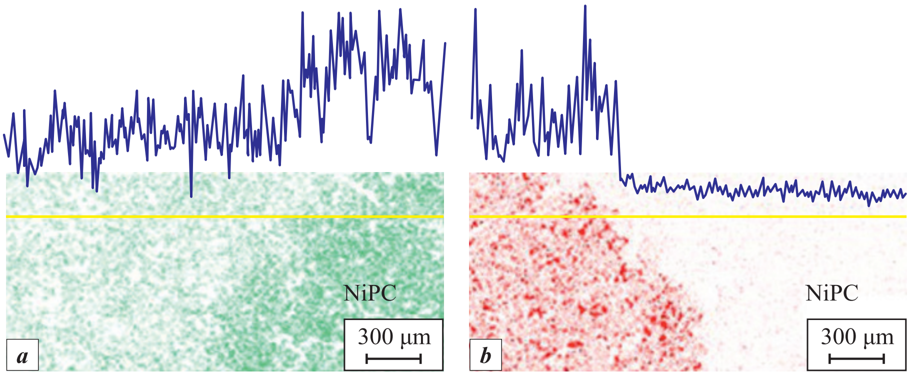

Fig. 3. The distribution of nickel (***a***) and chrome (***b***) at the interlayer boundary “P40KhN steel – Ni–P coating” after sintering at $t = 700$ °C for 2 h

Рис. 3. Распределение никеля (***a***) и хрома (***b***) на межслойной границе «сталь П40ХН – Ni–P-покрытие» после спекания при $t = 700$ °C в течение 2 ч

curve *1* and *2*). The studies demonstrated that the samples modified with boron nitride and polytetrafluoroethylene (Fig. 4, curve *4*) exhibited the minimum mass loss of coatings, whereas the samples with $(C_2F_4)n$-modified coatings (Fig. 4, curve *3*) had the largest losses. The mass loss decrease after sintering at $t = 400$ °C for 1 h is approximately the same for the $(C_2F_4)n$-modified coatings (Fig. 4, *b*, curves *1* and *2*).

As can be seen in Fig. 2 and 4, the microhardness and mass loss behavior, depending on the sintering temperature, coincides, and that is associated with the kinetics of coating microstructure formation.

According to the *X*-ray phase analysis, immediately after the chemical deposition, the boron nitride-modified NiPC exhibited an amorphous structure, which can be called an *X*-ray amorphous structure.

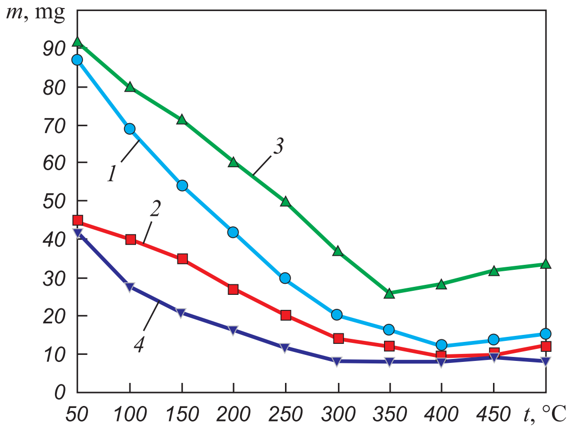

Fig. 4. The dependence of flake off mass on the sintering temperature and the composition on the samples made of P40Kh steel
1 – Ni–P, ***2*** – Ni–P + BN; ***3*** – Ni–P + $(C_2F_4)n$, ***4*** – Ni–P + BN + $(C_2F_4)n$

Рис. 4. Зависимость отслоившейся массы покрытия от температуры спекания и состава на образцах из стали П40Х
1 – Ni–P, ***2*** – Ni–P + BN; ***3*** – Ni–P + $(C_2F_4)n$, ***4*** – Ni–P + BN + $(C_2F_4)n$

It should be noted that the number of centers for the nucleation of NiPC inclusions virtually does not depend on the surface geometry of the powder samples, while the surface roughness and the presence of micro- and macropores impact the morphology (Fig. 5, *a* and *b*). In those areas of the surface of the sintered samples where the micropores are located, the content of nickel and phosphorus is noticeably lower than on the end surface of the samples made of hot-stamped P40Kh steel.

After sintering Ni–P + BN-coated samples made of P40Kh steel obtained by hot stamping of porous blanks within the temperature range of 350–370 °C for 1 h, β-Ni, Ni_3P, BN phases and a small amount of NiO, being well-identified in diffractograms (Fig. 6, *a*), were found. At the running-in stage during testing, the Ni_3P and BN phases are dispersed and their characteristic reflections are smeared, therefore they can only be approximately identified in *X*-ray patterns (Fig. 6, *a*, curve *2* and *3*). Furthermore, $Ni_{12}P_5$, Ni_2P and NiB highly dispersed phases arise during friction, and their content in the surface layers of the coating increases upon entering the stationary friction mode. The nickel oxides appeared to dissociate and disperse at the running-in stage and in the stationary friction mode, therefore, they could not be identified in the diffraction patterns.

The coefficient of friction (in the dry friction mode) slightly decreases from 0.29 at 20 °C to 0.22 at 300 °C upon temperature increase in the contact area of “steel 45 – P40Kh with NiPC” pair, while the temperature increases (Table 3). However, the wear rate increases significantly from 0.21 to 3.8 µm/h at the indicated heating temperatures of the coatings (Table 3). Upon modifying NiPC with boron nitride, the coefficient of friction (*f*) and wear rate (*I*) are slightly lower than those of the samples containing no additives (see Table 3). This can be explained by the fact that during the running-in of the coating surface, the dispersed NiB inclusions appear, and their con-

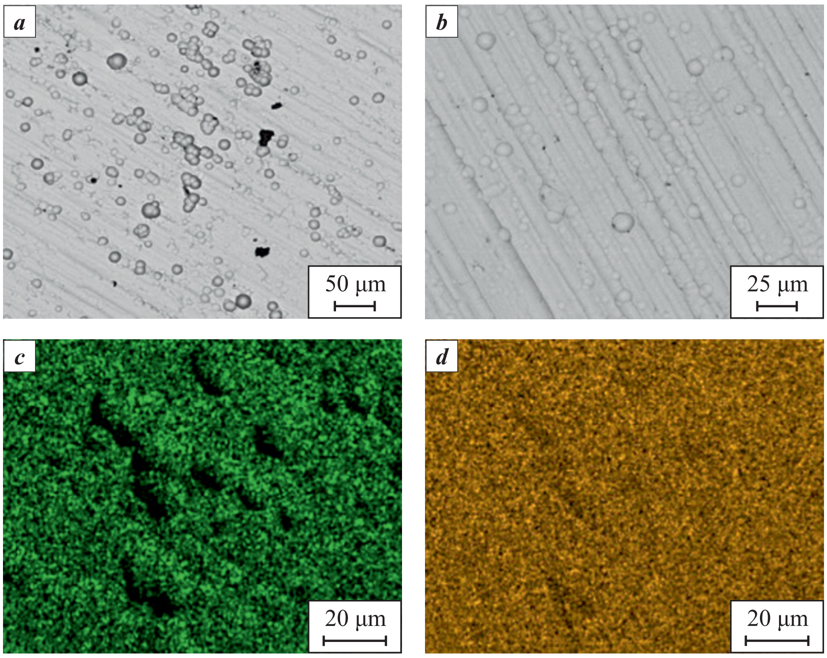

Fig. 5. The microstructure of NiPC on the surface of sintered steel before (***a***) and after (***b***) heat treatment and the behavior of distribution of nickel (***c***) and phosphorus (***d***) (light inclusions) in the coating

Рис. 5. Микроструктура НФП на поверхности спеченной стали до (***a***) и после (***b***) термообработки и характер распределения в покрытии никеля (***c***) и фосфора (***d***) (светлые включения)

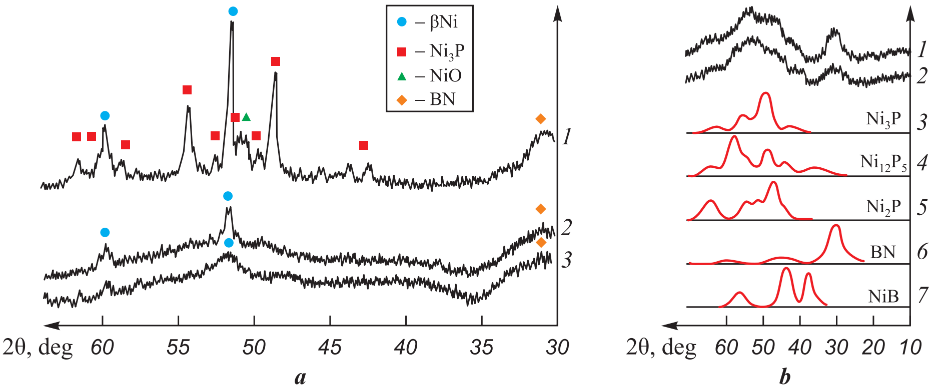

Fig. 6. The surface diffraction patterns of NiPC modified with BN
a – after sintering (***1***) and at the running-in stage (***2*** and ***3***);
b – in the steady-state friction mode (***3***–***7*** – the reflections being typical for the specified phases)

Рис. 6. Дифрактограммы поверхности НФП, модифицированного BN
a – после спекания (***1***) и на стадии приработки (***2*** и ***3***);
b – в установившемся режиме трения (***3***–***7*** – рефлексы, характерные для указанных фаз)

***Table 3.* The effect of the chemical composition of the modifiers on the coefficient of friction and wear rate at different temperatures**

***Таблица 3.* Влияние химического состава модификаторов на коэффициент трения и скорость изнашивания покрытий при разных температурах**

Coating composition	f			I, μm/h		
	t = 20 °C	250 °C	300 °C	20 °C	250 °C	300 °C
Ni–P	0.29	0.24	0.22	0.21	2.5	3.8
Ni–P + BN	0.25	0.22	0.20	0.18	2.1	3.1
Ni–P + $C_2F_4)n$	0.23	0.20	0.19	0.32	2.4	3.2
Ni–P + BN + $(C_2F_4)n$	0.20	0.18	0.17	0.14	1.5	2.2

tent does not change when entering the stationary friction mode (Fig. 7, *a*).

Upon modifying NiPC with $(C_2F_4)n$ polytetrafluoroethylene in the process of sintering under the aforementioned mode, the crystals of β-Ni and Ni_3P phase are formed more actively, while nickel oxide is absent (Fig. 7, *a*). During running-in, nickel particles actively interact with phosphorus; phosphorus-containing $Ni_{12}P_5$ and Ni_2P highly dispersed phases were found on the surface of the coating along with $(C_2F_4)n$ inclusions (Fig. 7, *b*). In this case, no phases formed during sintering were found in Ni–P + $(C_2F_4)n_4$ coating at the stage of the steady-state friction mode. Therefore, the diffraction patterns shown in Fig. 7, *a*, curve *3* and Fig. 7, *b*. curve *1* and *2* have a form being typical for materials with an amorphous-crystalline structure. Consequently, during friction, a structural-phase disorder arises on the surface of composite NiPC modified with NB and $(C_2F_4)n_4$.

Upon modifying NiPC with $(C_2F_4)n$ polytetrafluoroethylene, the coefficient of friction is slightly decreased and the wear rate in the steady state is virtually the same as that of coatings with NB additive (Table 3). The complex modification of Ni–P coatings with BN and $(C_2F_4)n$ showed the efficiency of their introduction. If, upon that, the phase composition of NiPC remains the same as that of a coating modified only with $(C_2F_4)n$ (Fig. 8, *a*), its tribological properties are significantly higher than after the introduction of these additives separately (Table 3). Particularly, upon adding $(C_2F_4)n$, the wear rate of NiPC at the stage of the stationary friction mode decreases by 1.3 times; upon adding BN, it decreases by 1.6 times, and it decreases virtually by 2 times upon the combined introduction of BN and $(C_2F_4)n$ (Table 3).

It should be noted that the performance of P40, P40Kh and P40KhN powder steels obtained by hot stamping of porous blanks coated with the Ni–P + BN + $(C_2F_4)n$

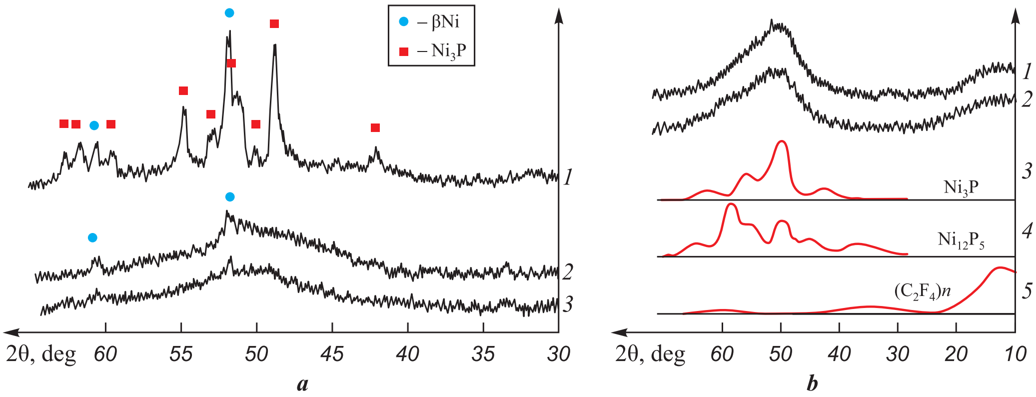

Fig. 7. The surface diffraction patterns of Ni–P + $(C_2F_4)n$ composite coating
a – after sintering (***1***) and at the running-in stage (***2*** and ***3***);
b – in the steady-state friction mode (***3–5*** – the reflections being typical for the specified phases)

Рис. 7. Дифрактограммы поверхности композиционного покрытия состава Ni–P + $(C_2F_4)n$
а – после спекания (***1***) и на стадии приработки (***2*** и ***3***);
b – в установившемся режиме трения (***3–5*** – рефлексы, характерные для указанных фаз)

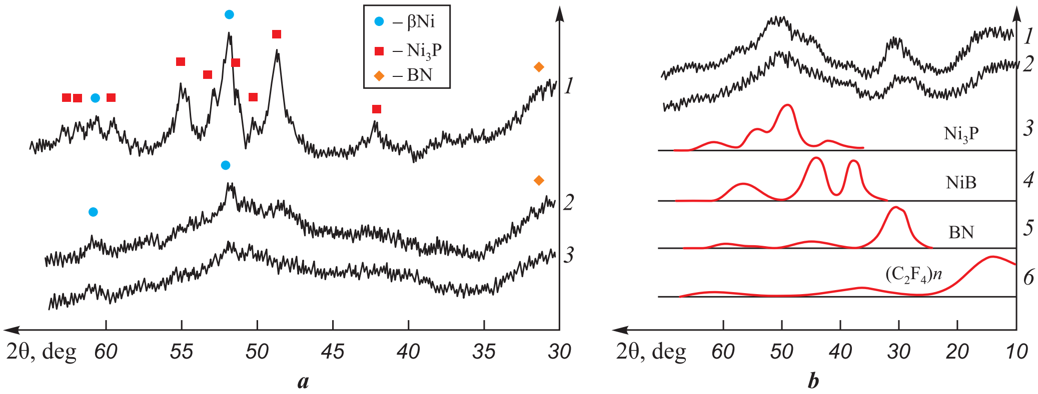

Fig. 8. The surface diffraction patterns of Ni–P + BN + $(C_2F_4)n$ coatings
a – after sintering (***1***) and at the running-in stage (***2*** and ***3***);
b – in the steady-state friction mode (***3–6*** – the reflections being typical for the specified phases)

Рис. 8. Дифрактограммы поверхности покрытий Ni–P + BN + $(C_2F_4)n$
а – после спекания (***1***) и на стадии приработки (***2*** и ***3***);
b – в установившемся режиме трения (***3–6*** – рефлексы, характерные для указанных фаз)

composition remained active for some time upon the appearance of traces of the base metal, while the samples with Ni–P-coating, which does not contain these additives, did not exhibit such a phenomenon.

Conclusion

It has been experimentally established that the process of formation of modified nickel-phosphorus coatings is initiated when the solution is heated above 35–40 °C. Upon temperature increase from 60 to 90 °C, the rate of coating build-up on the powder samples made of P40, P40Kh and P40KhN steel increases more intensively and reaches 14–19 μm/h, depending on the chemical composition of the coating. The microhardness of coatings of different chemical composition is largely effected by the mode of the subsequent heat treatment.

It was newly revealed that composite NiPC are rather brittle and flake off easily after deposition; upon sintering the powder samples with such coatings in the range of $t = 500–700$ °C, nickel and steel interdiffusion occurs at steel–coating interface and a transitional diffusion layer, contributing to an increase in strength of adhesion of the coating to the substrate, forms. During friction, $Ni_{12}P_5$, Ni_2P and NiB highly dispersed phases, improving the tribological properties, arise. The contents of these phases in the surface layers of the coating increase when entering the stationary friction mode.

It has been theoretically and experimentally substantiated that the complex modification of nickel-phosphorus coatings with BN and $(C_2F_4)n$ allows to reduce the coefficient of friction and the wear rate at the stage of the stationary mode. When only $(C_2F_4)n$ polytetrafluoroethylene is added to NiPC, the coefficient of friction and the wear rate decrease by 1.3 times; upon adding BN, they decrease by 1.6 times, and upon the combined BN and $(C_2F_4)n$ modification they decrease virtually by 2 times.

References / Список литературы

1. Kutkov A.A. Wear-resistant and anti-friction coatings. Moscow: Mashinostroenie, 1976. 152 p. (In Russ.).

   Кутьков А.А. Износостойкие и антифрикционные покрытия. М.: Машиностроение, 1976. 152 с.
2. Mashkov Y.K. Tribology of structural materials: manual. Omsk: OmGTU, 1996. 298 p. (In Russ.).

   Машков Ю.К. Трибология конструкционных материалов: Учеб. пособие. Омск: Изд-во ОмГТУ, 1996. 298 с.
3. Gawrilov G., Owtscharova E. Die Chemische Abscheidung von Dispersionsschichten mit Ni–P und Ni–B-matrix. Einlagern von oxiden: Titanoxid. *Galvanotechnik*. 1973;64(1):23–28.
4. Djokic S.S. Electroless deposition of metals and alloys. In: *Modern Aspects of Electrochemistry*. Conway B.E., White R.E. (eds). 2002;(35):51–133. https://doi.org/10.1007/0-306-47604-5_2
5. Pettarina V., Churrucaa M.J., Felhosb D., Karger-Kocsisc J., Frontinia P.M. Changes in tribological performance of high molecular weight high density polyethylene induced by the addition of molybdenum disulphide particles. *Wear*. 2010;269(1–2):31–45. https://doi.org/10.1016/j.wear.2010.03.006
6. Cavallotti P.L., Magagnin L., Cavallotti C. Influence of added elements on autocatalytic chemical deposition electroless NiP. *Electrochimica Acta*. 2013;114:805–812. https://doi.org/10.1016/j.electacta.2013.09.083
7. Song Y.W., Shan D.Y., Han E.H. Corrosion behaviors of electroless plating Ni–P coatings deposited on magnesium alloys in artificial sweat solution. *Electrochimica Acta*. 2007;53(4):2009–2015. https://doi.org/10.1016/j.electacta.2007.08.062
8. Guseva I.V., Mashchenko T.S., Borisenko A.I. Chemical deposition of coatings with the inclusion of fibrous fillers. In: *Processing of 9th All-Union. Heat Resistant Coatings Meetings*. Leningrad: Nauka, 1981. P. 66–68. (In Russ.).

   Гусева И.В., Мащенко Т.С., Борисенко А.И. Химическое осаждение покрытий с включением волокнистых наполнителей. *В сб. Тр. 9-го Всесоюз. совещания по жаростойким покрытиям*. Л.: Наука, 1981. С. 66–68.
9. Dziadur W. Structure and mechanical properties of nickel-phosphorus coatines. In: *Processing of 15th Conference Mater. Test. Metall. [during] 11th Conference Mater-Test., (EROMAT, 94)* (Balatonzerplak, 30 May–1 June, 1994). 1994. Vol. 4. P. 1154–1158.
10. Shcherbakov I.N., Ivanov V.V., Korotkiy A.A. Elaboration and Investigation of metallic coating with inclusion of potassium polytitanate. *Solid State Phenomena*. 2018;284:1140–1143. https://doi.org/10.4028/www.scientific.net/SSP.284.1140
11. Shcherbakov I.N., Ivanov V.V., Logvinov V.T., Derlugyan P.D., Trofimov G.E., Derlugyan F.P. Chemical nanoconstruction of composite materials and coatings with antifriction properties. Rostov-on-Don: Izdatel'stvo zhurnala «Izv. vuzov. Severo-Kavkazskii region», 2011. 130 p. (In Russ.).

    Щербаков И.Н., Иванов В.В., Логвинов В.Т., Дерлугян П.Д., Трофимов Г.Е., Дерлугян Ф.П. Химическое наноконструирование композиционных материалов и покрытий с антифрикционными свойствами. Ростов-на-Дону: Издательство журнала «Известия вузов. Северо-Кавказский регион», 2011. 130 с.
12. Trofimov G.E., Scherbakov I.N., Shevchenko M.Yu., Loginov V.T., Derlugyan P.D., Derlugyan F.P., Ivanov V.V. Solution for chemical deposition of composite coating: Patent 2451113 (RF). 2012. (In Russ.).

    Трофимов Г.Е., Щербаков И.Н., Шевченко М.Ю., Логинов В.Т., Дерлугян П.Д., Дерлугян Ф.П., Иванов В.В. Раствор для химического осаждения композиционного покрытия: Патент 2451113 (РФ). 2012, http://www.fips.ru/Archive/PAT/2012FULL/2012.05.20/DOC/RUNWC1/000/000/002/451/113/document.pdf
13. Ivanov V.V., Scherbakov I.N. Modeling of composite nickel-phosphorus coatings with antifriction properties. Rostov-on-Don: Izdatel'stvo zhurnala «Izv. vuzov. Severo-Kavkazskii region», 2008. 111 p. (In Russ.).

Иванов В.В., Щербаков И.Н. Моделирование композиционных никель-фосфорных покрытий с антифрикционными свойствами. Ростов-на-Дону: Издательство журнала «Известия вузов. Северо-Кавказский регион», 2008. 111 с.

14. Petukhov I.V., Semenova V.V., Medvedeva N.A., Oborin V.A. Effect of deposition time on the formation of Ni–P coatings. *Vestnik Permskogo universiteta. Khimiya*. 2011;3:47–56. (In Russ.).

Петухов И.В., Семенова В.В., Медведева Н.А., Оборин В.А. Влияние времени осаждения на процессы формирования Ni–P покрытий. *Вестник Пермского университета. Химия*. 2011;(3):47–56.

15. Goldenstein A., Rostoker W., Schossberger F., Gutzeit G. Structure of chemically deposited nickel. *Journal of the Electrochemical Society*. 1957;104(2):104–110.

16. Królikowski A., Wiesko A. Impedance studies of hydrogen evolution on Ni–P alloys. *Electrochimica Acta*. 2002;47(13-14):2065–2069.
https://doi.org/10.1016/S0013-4686(02)00074-9

17. Soboleva E.S., Ryabchikova L.S. Comparative assessment of the wear resistance of nickel-phosphorus and chrome coatings in friction nodes. *Vestnik Yaroslavskogo gosudarstvennogo tekhnicheskogo universiteta*. 2004;(4):81–82. (In Russ).

Соболева Е.С., Рябчикова Л.С. Сравнительная оценка износостойкости никель-фосфорных и хромовых покрытий в узлах трения. *Вестник Ярославского государственного технического университета*. 2004;(4):81–82.

18. Cheong W., Luan B.L., Shoesmith D.W. Protective coating on Mg AZ91D alloy – The effect of electroless nickel (EN) bath stabilizers on corrosion behaviour of Ni–P deposit. *Corrosion Science*. 2007;49(4):1777–1798.
https://doi.org/10.1016/j.corsci.2006.08.025

19. Sayfulin R.S. Composite coatings and materials. Moscow: Khimiya, 1977. 272 p. (In Russ.).

Сайфулин Р.С. Композиционные покрытия и материалы. М.: Химия, 1977. 272 с.

20. Xiaoming Chen, Liuyang Zhang, Cheol Park, Catharine C. Fay, Xianqiao Wang, Changhong Ke. Mechanical strength of boron nitride nanotube-polymer interfaces. *Applied Physics Letters*. 2015;107(25):253105.
https://doi.org/10.1063/1.4936755

21. Sugg J. Quality electroless nickel plating through statistical process control. In: *Processing of 77th AESF Annu. Tech. Conference* (Boston, Mass., July 9–12, 1990). Orlando (Fla), 1990, Vol. 1. P. 1417–1424.

22. Dorofeev Yu.G., Marinenko L.G., Ustimenko V.I. Structural powder materials and products. Moscow: Metallurgiya, 1986. 143 p. (In Russ.).

Дорофеев Ю.Г., Мариненко Л.Г., Устименко В.И. Конструкционные порошковые материалы и изделия. М.: Металлургия, 1986. 143 с.

23. Mirkin L.I. Handbook of *X*-ray diffraction analysis of polycrystals. Moscow: Fizmatgiz, 1961. 862 p. (In Russ.).

Миркин Л.И. Справочник по рентгеноструктурному анализу поликристаллов. М.: Физматгиз, 1961. 862 с.

24. Ivanov A.N., Rastorguev L.N., Skakov Yu.A., Umanskii Ya.S. Crystallography, radiography and electron microscopy. Moscow: Metallurgiya, 1982. 632 p. (In Russ.).

Иванов А.Н., Расторгуев Л.Н., Скаков Ю.А., Уманский Я.С. Кристаллография, рентгенография и электронная микроскопия. М.: Металлургия, 1982. 632 с.

Information about the Authors

Igor N. Shcherbakov – Cand. Sci. (Eng.), Associate Professor of the Department «Operation of vehicles and logistics», Don State Technical University
ORCID: 0000-0002-3129-078X
E-mail: bdd-don@mail.ru

Бадрудин Гасанович Гасанов – Dr. Sci. (Eng.), Professor of the Department «Cars and transport and technological complexes», Platov South-Russian State Polytechnic University
E-mail: gasanov.bg@gmail.com

Сведения об авторах

Игорь Николаевич Щербаков – к.т.н., доцент кафедры «Эксплуатация транспортных средств и логистика», Донской государственный технический университет
ORCID: 0000-0002-3129-078X
E-mail: bdd-don@mail.ru

Бадрудин Гасанович Гасанов – д.т.н., профессор кафедры «Автомобили и транспортно-технологические комплексы», Южно-Российский государственный политехнический университет им. М.И. Платова
E-mail: gasanov.bg@gmail.com

Contribution of the Authors

I. N. Shcherbakov – preparation and management of the experiments, testing the samples, writing the text, conducting the experiments, processing of the research results.
B. G. Gasanov – scientific guidance, correction of the text and conclusions.

Вклад авторов

И. Н. Щербаков – подготовка эксперимента, испытаний образцов, подготовка текста статьи, проведение экспериментов, обработка результатов исследований, обеспечение ресурсами.
Б. Г. Гасанов – научное руководство, корректировка текста, корректировка выводов.

Received 05.04.2022
Revised 31.10.2022
Accepted 10.11.2022

Статья поступила 05.04.2022 г.
Доработана 31.10.2022 г.
Принята к публикации 10.11.2022 г.

Nanostructured Materials and Functional Coatings
Наноструктурированные материалы и функциональные покрытия

UDC 620.18

https://doi.org/10.17073/1997-308X-2023-2-62-70

Research article
Научная статья

Investigation of the tribological characteristics of Ta–Zr–Si–B–C–N coatings

A. D. Sytchenko ✉, R. A. Vakhrushev, Ph. V. Kiryukhantsev-Korneev

National University of Science and Technology "MISIS"
4 bld.1 Leninskiy Prosp., Moscow 119049, Russia

✉ alina-sytchenko@yandex.ru

Abstract. Ta–Zr–Si–B–C–N coatings were deposited by magnetron sputtering using a TaSi$_2$–Ta$_3$B$_4$–(Ta, Zr)B$_2$ composite target. Ar, as well as Ar + N$_2$ and Ar + C$_2$H$_4$ gas mixtures, were used as the working gas. The structure and composition of the coatings were studied by scanning electron microscopy, glow-discharge optical emission spectroscopy, and *X*-ray diffraction. A Calowear tester was used to measure the thickness and abrasion resistance of the coatings. Erosion resistance tests were carried out using a UZDN-2T (Russia) ultrasonic disperser. Tribological tests in the sliding friction mode were carried out on an HT Tribometer (CSM Instruments, Switzerland) automated friction machine. The wear zone after tribological testing was examined using a Veeco Wyko 1100 (Veeco, USA) optical profiler. The results showed that the Ta–Zr–Si–B coating was characterised by a columnar structure with an *h*-TaSi$_2$ crystallite size of 11 nm. The introduction of nitrogen and carbon into the composition of the coatings led to the suppression of columnar growth and a ~2–4-fold decrease in the size of *h*-TaSi$_2$ crystallites. Carbon-containing coatings demonstrated the best abrasive resistance. The sliding friction tests showed that the Ta–Zr–Si–B coating is characterised by a stable coefficient of friction of 0.3 at a temperature of 25 °C up to the maximum working temperature of 250 °C. The introduction of nitrogen led to an increase in the coefficient of friction up to 0.8–1.0 at a $t = 50 \div 110$ °C. The coating with the minimum carbon concentration showed a stable coefficient of friction of ~0.3 up to a maximum temperature of 250 °C. The best result was demonstrated by the sample containing the maximum amount of carbon, with its coefficient of friction remaining at the 0.25 level up to a temperature of 350 °C.

Keywords: magnetron sputtering, coatings, TaSi$_2$, ZrB$_2$, abrasion and erosion resistance, high-temperature tribology

Acknowledgements: This work was carried out with the financial support of the Russian Science Foundation (project 19-19-00117-П). The authors are grateful to Senior Engineer N.V. Shvyndina (NUST MISIS) for the help in the structural studies.

For citation: Sytchenko A.D., Vakhrushev R.A., Kiryukhantsev-Korneev Ph.V. Investigation of the tribological characteristics of Ta–Zr–Si–B–C–N coatings. *Powder Metallurgy and Functional Coatings*. 2023;17(2):62–70. https://doi.org/10.17073/1997-308X-2023-2-62-70

Исследование триботехнических характеристик покрытий Ta–Zr–Si–B–C–N

А. Д. Сытченко ✉, Р. А. Вахрушев, Ф. В. Кирюханцев-Корнеев

Национальный исследовательский технологический университет «МИСИС»
119049, г. Москва, Ленинский пр-т, 4, стр. 1

✉ alina-sytchenko@yandex.ru

Аннотация. Покрытия Ta–Zr–Si–B–C–N были нанесены методом магнетронного распыления с использованием композиционной мишени TaSi$_2$–Ta$_3$B$_4$–(Ta, Zr)B$_2$. В качестве рабочего газа использовали Ar, а также смеси газов Ar + N$_2$ и Ar + C$_2$H$_4$. Структуру и состав покрытий исследовали методами сканирующей электронной микроскопии, оптической эмиссионной спектроскопии тлеющего разряда и рентгенофазового анализа. Толщину и стойкость покрытий к абразивному воздействию оценивали по схеме «шарик–шлиф». Испытания на эрозионную стойкость проводили с использованием ультразвукового диспергатора УЗДН-2Т (Россия). Трибологические испытания в режиме трения–скольжения осуществляли на автоматизированной машине трения HT Tribometer («CSM Instruments», Швейцария). Зону износа после трибологических испытаний исследовали с помощью оптического профилометра Wyko 1100 («Veeco», США). Результаты показали, что покрытие Ta–Zr–Si–B характеризуется столбчатой структурой с размером кристаллитов *h*-$TaSi_2$ порядка 11 нм. Введение азота и углерода в состав покрытий привело к подавлению столбчатого роста и снижению размера кристаллитов *h*-$TaSi_2$ в 2–4 раза. Лучшую абразивную и эрозионную стойкость показали углеродсодержащие покрытия. Испытания на трение–скольжение показали, что покрытие Ta–Zr–Si–B характеризуется стабильным коэффициентом трения на уровне 0,3, начиная с 25 °C и до максимальной рабочей температуры 250 °C. Введение азота привело к росту коэффициента трения до значений 0,8–1,0 при $t = 50 \div 110$ °C. Покрытие с минимальной концентрацией углерода показало стабильный коэффициент трения ~0,3 до максимальной температуры 250 °C. Наилучший результат продемонстрировал образец, содержащий наибольшее количество углерода: его коэффициент трения сохранялся на уровне 0,25 до температуры 350 °C.

Ключевые слова: магнетронное напыление, покрытия, $TaSi_2$, ZrB_2, абразивная и эрозионная стойкость, высокотемпературная трибология

Благодарности: Работа выполнена при финансовой поддержке Российского научного фонда (проект 19-19-00117-П).

Авторы признательны ведущему инженеру Н.В. Швындиной (НИТУ МИСИС) за помощь в проведении структурных исследований.

Для цитирования: Сытченко А.Д., Вахрушев Р.А., Кирюханцев-Корнеев Ф.В. Исследование триботехнических характеристик покрытий Ta–Zr–Si–B–C–N. *Известия вузов. Порошковая металлургия и функциональные покрытия*. 2023;17(2):62–70. https://doi.org/10.17073/1997-308X-2023-2-62-70

Introduction

Tantalum disilicide is one of the promising materials in the family of high-temperature ceramics due to its high melting point (2300±100 °C) [1], electrical resistivity (50–70 μΩ·cm) [2], hardness (16 GPa) [3], strength at temperatures above 1000 °C, and good oxidation resistance [4]. $TaSi_2$ coatings are characterised by high thermal stability up to 500 °C and oxidation resistance at 800 °C due to the formation of a Ta_2O_5–SiO_2 oxide layer [5]. Due to their low resistivity (70 μΩ·cm) at $t = 800 \div 900$ °C, $TaSi_2$ coatings are often used in the semiconductor industry [6; 7].

To improve its mechanical and tribological properties and its oxidation resistance, tantalum silicide is doped with various elements such as C, N, B, Hf, and Zr [8–16]. The carbon-doped $TaSi_2$ coating demonstrates good resistance to high-temperature erosion at a thermal flux of 2.4 MW/m^2 [9] and oxidation resistance at $t = 900$ °C for more than 233 h [10]. The authors explain high oxidation resistance as due to the formation of a dense Ta_2O_5–SiO_2 oxide layer. The introduction of nitrogen also improves the mechanical properties and oxidation resistance of $TaSi_2$ coatings.

The study [11] found an extreme dependence of hardness and fracture toughness on the nitrogen content: their maximum values $H = 36$ GPa and $K_{1c} = 3.95$ MPa·m$^{0.5}$, respectively, were reached at a concentration of 35 at. % N. The Ta–Si–N coating is characterised by good oxidation resistance and thermal stability at $t = 700$ °C [12]. In previous studies, the authors studied the structure and properties of Ta–Si–N coatings [13]. The results showed that coatings with an optimal nitrogen concentration had the maximum values of hardness (24 GPa) and elastic recovery (77 %), and also demonstrated high oxidation resistance at $t = 1200$ °C. It is known that introducing nitrogen in Ta–Si–C coatings increases their tribological characteristics at temperatures up to 800 °C due to the formation of the ternary oxide $TaSiO_x$ in the contact area [14].

Research on the effect of the introduction of additives of transition metal borides to the composition of $TaSi_2$-based coatings has been limited to a few studies. Doping Ta–Si–C coatings with zirconium boride [15] increases their adhesive and cohesive strength. The specimens demonstrate good oxidation resistance at $t = 1500$ °C, which may be related to the formation of a protective ZrO_2–SiO_2 oxide layer that prevents oxygen penetration. We have previously investigated the structure and oxidation resistance of Ta–Zr–Si–B–C–N coatings [16] obtained by magnetron sputtering in various gaseous media.

The main objective of this work is to study the tribotechnical characteristics of Ta–Zr–Si–B–C–N coatings exposed to abrasion and erosion impacts and in the sliding friction mode.

Materials and methods

The coatings were deposited by magnetron sputtering in a direct current mode. A sputtered composite target $TaSi_2$–Ta_3B_4–(Ta, Zr)B_2 (composition, at. %: 70.8 Ta, 18.6 Si, 7.4 Zr, 2.9 B) of diameter 120 mm and thickness 6 mm was obtained by hot pressing of crushed products of self-propagating high-temperature synthesis (SHS). Equipment based on the UVN-2M (УВН-2М) pumping system (JSC Kvarts, Russia) with a schematic diagram given in the work [17] was used to deposit the coatings. VOK-100-1 (ВОК-100-1) (JSC Polikor, Russia) aluminium oxide plates and disks were used as model substrates for the coatings. Before coating, the substrates were cleaned for 5 min in isopropyl alcohol using a UZDN-2T (УЗДН-2Т) unit (NPP UkrRosPribor, Ukraine) with an operating frequency of 22 kHz and in a vacuum using a gap-type ion source (Ar^+ ions, 2 keV) for 20 min. Ar (99.9995 %) and its mixtures with N_2 (99.999 %) and C_2H_4 (99.95 %) were used as the working gas. The flow rate was controlled using a gas injection system (OOO Eltochpribor, Russia). The values are given in the table.

The coatings were deposited under the following conditions: the distance between the substrate and the target was 80 mm, the residual pressure was 10^{-3} Pa, and the working pressure in the vacuum chamber was 0.1÷0.2 Pa. The magnetron power was kept constant at 1 kW using a Pinnacle+ power supply (Advanced Energy, USA), with a deposition time of 40 min.

The distribution profiles of the elements and the thickness-averaged composition of the coatings were determined using the glow-discharge optical emission spectroscopy (GDOES) method on a Profiler 2 device (Horiba Jobin Yvon, France) [18]. The structure of the coatings was examined by scanning electron microscopy (SEM) using an S-3400 microscope (Hitachi, Japan). *X*-ray diffraction (XRD) was performed on a D2 Phaser diffractometer (Bruker, Germany) using CuK_α-radiation. The *X*-ray photoelectron spectroscopy (XPS) studies were carried out on a PHI 5000 VersaProbe-II (ULVAC-PHI, USA) instrument. The excitation source was monochromatised AlK_α-radiation ($h\nu$ = 1486.6 eV) with a power of 50 W and a diameter of 200 μm.

The thickness and abrasion resistance of the coatings were measured by a Calowear tester (JSC NII Tavtoprom, Russia) according to the ball-specimen set up as described in the methodology [19]. The material was exposed to an abrasive DiaPro suspension with a 1 μm polycrystalline diamond dispersion fed into the gap between a rotating ShKh-15 (ШХ-15) steel ball of diameter 27 mm and the surface of a stationary sample. The ball rotation speed was 13 rpm, and the load was 1.5 N. The volume of the coating material removed was determined using 2D microscopic images.

Abrasion tests were also used to determine the coating thickness using the formula

$$S = \frac{b^2 - a^2}{8R},$$

where *b* is the wear scar diameter, μm; *a* is the substrate diameter, μm; *R* is the ball radius, μm.

The quantity of the coating material removed was calculated using the formula

$$V = \frac{\pi}{64R}\left(b^4 - a^4\right),$$

where *b* and *a* are the outer and inner diameters of the crater, respectively, mm.

Erosion tests were carried out using a UZDN-2T (УЗДН-2Т) (NPP UkrRosPribor, Ukraine) ultrasonic disperser. A sample was placed in a container positioned in the working area, after 20 ml of water and 5 g of Si_3N_4 abrasive material were added. The distance from the waveguide to the substrate surface was 1 mm, and the frequency was set at 22 kHz. The experiment lasted 15–60 min. The change in the mass of the coating samples due to erosive impact was estimated using a GR202 (AND, Japan) analytical balance with an accuracy of 0.01 mg.

The coatings were tested for sliding friction on an HT Tribometer (CSM Instruments, Switzerland) auto-

Gas flow rate and chemical composition of the coatings

Расход газа и химический состав покрытий

Sample No.	Gas flow rate, cm^3/min			Composition, at. %					
	Ar	N_2	C_2H_4	Ta	Zr	Si	B	N	C
1	25	–	–	40.0	7.5	28.0	24.5	0	0
2	20	5	–	27.3	7.7	22.3	22.3	20.4	0
3	15	10	–	19.3	5.4	17.1	15.7	42.5	0
4	20	–	5	28.1	10.1	25.7	23.6	0	12.5
5	15	–	10	22.1	8.0	21.1	18.4	0	30.4

mated friction machine using a 6-mm-diameter Al_2O_3 ball as a counter body. The load was 1 N. The change in the coefficient of friction was recorded during heating from a temperature of 25 °C to 500 °C. The contact zones after tribological tests in the abrasive wear and sliding friction modes were examined using a Wyko 1100 (Veeco, USA) optical profiler.

Result and discussion

Composition and microstructure of coatings

The table above shows the elemental composition of the coatings. It can be seen that the concentrations of nitrogen and carbon in the coatings increased with an increase in the N_2 and C_2H_4 gas flow rates, respectively.

Fig. 1, *a* shows the *X*-ray diffraction patterns of the coatings taken in the $2\theta = 20 \div 50°$ range.

Besides the Al_2O_3 substrate peaks (card JCPDS 88–0107), the *X*-ray diffraction pattern of coating *1* showed peaks corresponding to the hexagonal *h*-$TaSi_2$ phase (JCPDS 89-2941). Note that the differences in the intensity of the peaks from the Al_2O_3 substrate may be associated with a change in the composition and amorphisation of the coatings as a result of the introduction of nitrogen or carbon. The size of the *h*-$TaSi_2$ crystallites, determined by the Scherrer equation, was 11 nm. The introduction of N_2 and C_2H_4 into the gaseous medium resulted in the formation of coatings with a highly dispersed or amorphous structure. For nitrogen- and carbon-containing coatings, the peak maxima positions in the $2\theta = 25 \div 45°$ range were close to the positions of the most intense peaks of the TaN (JCPDS 89–5198) and TaC (JCPDS 89–3831) FCC phases.

The crystallite size of the *h*-$TaSi_2$ phase for reactive coatings *2*–*5* was estimated from minimally overlapping lines. For coatings *2* and *3* deposited at an N_2 flow rate of 5 and 10 cm^3/min, the sizes were 6.0 and 4.5 nm, while for carbon-containing coatings *4* and *5*, they were similar at 3.5 and 3.0 nm, respectively. The decrease in the size of *h*-$TaSi_2$ crystallites and the amorphisation of coatings upon transition to reaction media are associated with the formation of new TaN and TaC phases, which, apparently, interrupt the growth of *h*-$TaSi_2$ crystallites.

According to the SEM images, base coating *1* had a columnar structure (see Fig. 1, *b*). It is important to note that this phenomenon adversely affects the mechanical properties and oxidation resistance of coatings [20; 21]. All reactive coatings showed an identical structure. The introduction of N_2 and C_2H_4 into the gas medium led to the suppression of columnar growth and the formation of highly dispersed crystallites.

The Calowear tester measurements showed coatings *1* and *2* as having a similar thickness of 7.2 and

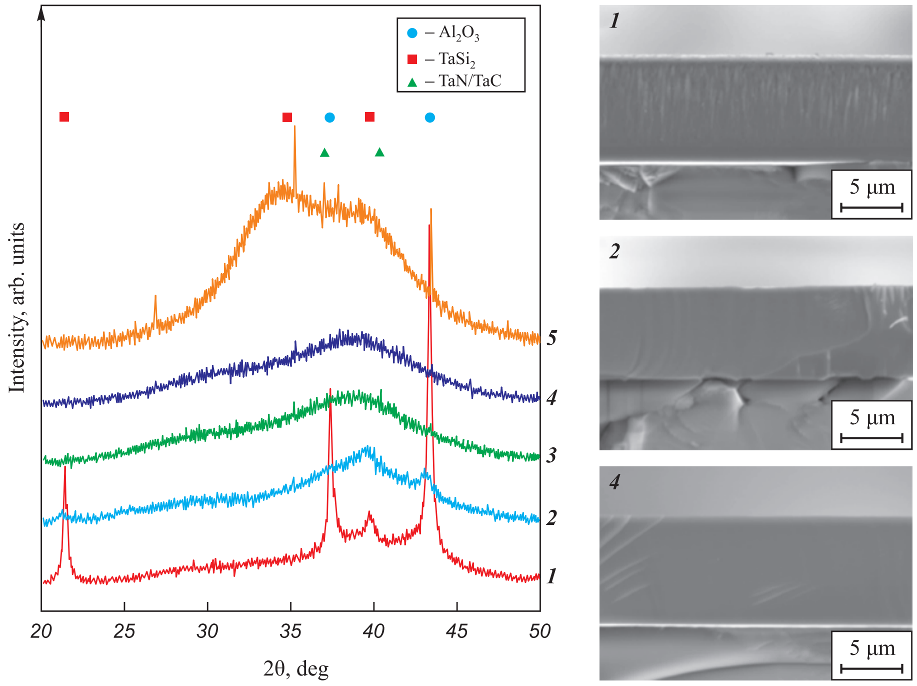

a *b*

Fig. 1. *X*-ray diffraction patterns of the coatings ***1***–***5*** (***a***) and cross-section SEM images of the coatings ***1***, ***2*** and ***4*** (***b***)

Рис. 1. Рентгенограммы покрытий ***1***–***5*** (***a***) и СЭМ-изображения поперечного излома покрытий ***1***, ***2*** и ***4*** (***b***)

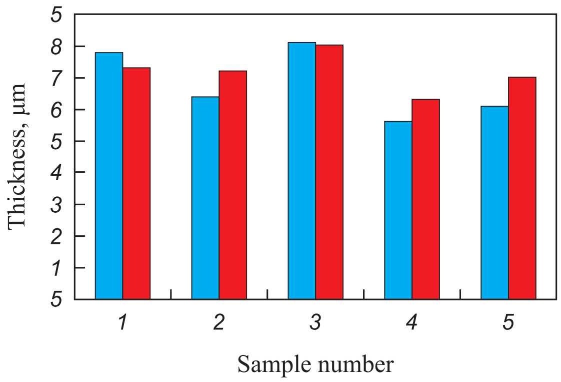

Fig. 2. Comparison of the thicknesses of coatings ***1–5*** obtained by the Calowear tester (🟦) and from the cross-section SEM images of the coatings (🟥)

Рис. 2. Сравнение значений толщины покрытий ***1–5***, полученных методами «шарик–шлиф» (🟦) и по СЭМ-изображениям поперечных изломов (🟥)

7.0 μm, respectively (Fig. 2). An increase in nitrogen concentration led to its growth by 25 %. In [11], a similar result was obtained related to an increase in the thickness of coatings with an increase in the N_2 gas flow rate. Increasing the C_2H_4 flow rate to 5 and 10 cm^3/min led to a decrease in thickness by 18 and 10 %, respectively. The Calowear tester measurements were compared with the thickness values determined from the fracture cross-section SEM images of the coatings (Fig. 2). The results obtained were similar. This method can therefore be used for the rapid assessment of coating thicknesses.

Erosion resistance

The trial tests allowed determining the optimal mode in which the wear of the coatings (abrasive material – Si_3N_4, its mass – 5 g, liquid volume – 20 ml) was observed. The graph in Fig. 3 shows the dependence of the change in mass on the time of exposure to abrasive particles.

Coating *1* obtained in the Ar medium was observed to have the minimum mass loss $\Delta m = -0.2$ mg throughout the experiment. For coating *2*, the value of Δm increased to 0.2 mg over a 0–30 min interval, which is probably due to the adhesion of wear products and abrasive particles on the sample surface. The subsequent decrease in mass by 3.8 mg over a 30–60 min interval is due to coating wear (Fig. 3, *b*). Coating *3* had the value $\Delta m = -0.3$ mg over a 60 min interval, which corresponds to the data obtained for the non-reactive coating. Unstable behaviour was observed for the carbon-containing sample *4*: the Δm value increased by 1.0 mg over a 0–15 min interval, after which at 15–30 min of exposure it dropped to the initial values. Over a 30–60 min interval, $\Delta m = 0.8$ mg. Coating *5* with the maximum carbon concentration had $\Delta m = 1.5$ mg over a 0–15 min interval, after which the sample mass gradually decreased and by the 60th minute of the test approached the initial value ($\Delta m \approx -0.1$ mg).

Visual inspection of the samples revealed no signs of wear on the coating surface *1* (Fig. 3, *b*). The coatings obtained in nitrogen had a clear circular wear boundary with noticeable areas of the substrate, whereas the samples obtained in ethylene had less pronounced wear marks and no areas corresponding to the substrate.

The samples obtained in Ar and Ar + C_2H_4 media therefore showed the best erosion resistance. The high erosion resistance of carbon-containing coatings can be explained by the increased hardness of the TaC carbide phase compared to the TaN and $TaSi_2$ phases [22; 23].

Abrasion resistance

The results of the abrasive tests showed that scratches from the impact of abrasive particles were observed on the surfaces of all samples. Fig. 4 shows the depths (*H*) and thickness (*h*) of wear craters under abrasive action for coatings *1–5*.

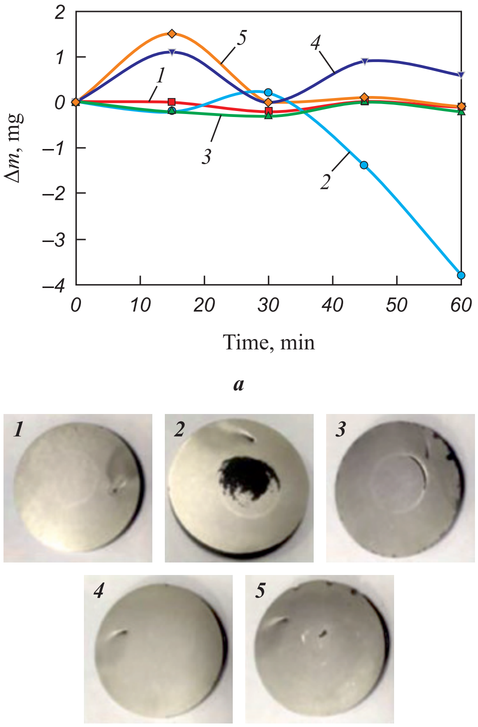

Fig. 3. Dependence of the change in mass on the time of exposure to abrasive particles (***a***) and photographs of samples after 60 min of exposure (***b***)
1–5 – numbers of coating samples

Рис. 3. График зависимости изменения массы от времени воздействия абразивных частиц (***a***) и фотографии образцов после 60 мин воздействия (***b***)
1–5 – номера образцов покрытий

Fig. 5 shows the dependence of the volume of material removed (V) on the abrasive exposure time (1- and 3-min) for the studied samples. Coatings *1*, *3–5* showed similar values of $H = 4 \div 5$ μm and $V = 5 \div 6 \cdot 10^{-4}$ mm^3, respectively, differing within the error margin. The nitrogen-containing coating *2* has maximum values of $H = 5$ μm and $V = 11 \cdot 10^{-4}$ mm^3. With an increase in the exposure time to 3 min, coatings *1–3* had crater depths in the range of 6–7 μm, and the volume of the removed material was $24 \cdot 10^{-4}$ mm^3. Note that the crater depths did not exceed the thickness of the samples *1–3*. After a 3-minute exposure, coating *4* had an H value of 7 μm at a thickness of 6 μm, which is indicative of wear. In this case, the sample was characterised by a lower value of $V = 18 \cdot 10^{-4}$ mm^3 compared to coatings *1–3*, which may be due to the influence of the solid Al_2O_3 substrate. Coating *5* with the lowest carbon concentration showed the minimum results ($H = 5.5$ μm and $V = 15 \cdot 10^{-4}$ mm^3).

Summing up the data obtained, it can be concluded that the coating deposited at the maximum concentration of ethylene has better abrasive resistance, which may be due to the positive role of carbon in the friction process [24].

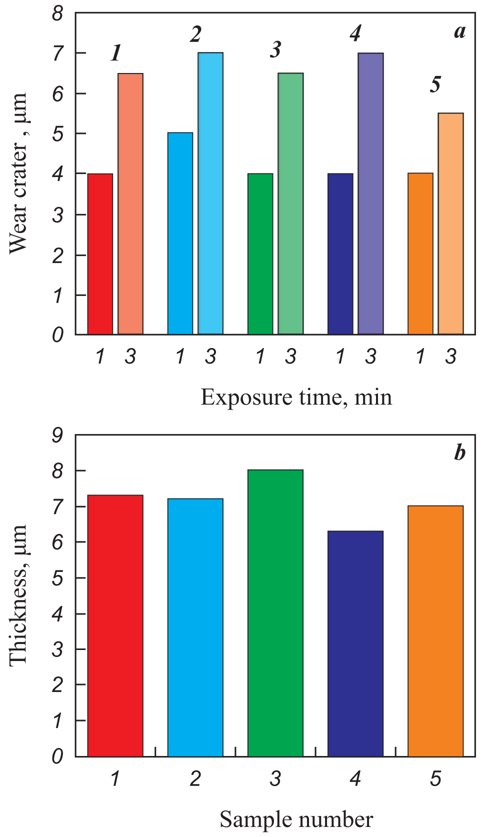

Fig. 4. Depth (***a***) and thickness (***б***) of wear craters under abrasive action over 1- and 3-min intervals for coatings ***1–5***

Рис. 4. Глубина кратеров износа (***а***) и толщина (***б***) при абразивном воздействии в течение 1 и 3 мин для покрытий ***1–5***

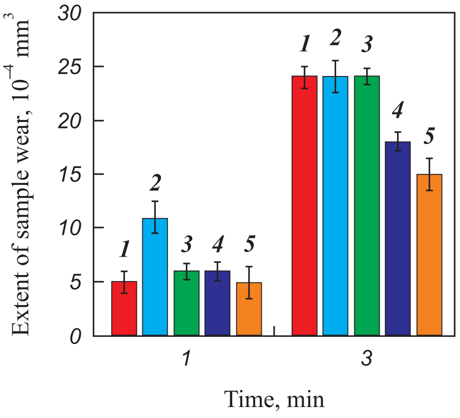

Fig. 5. Extent of sample wear during abrasive exposure over 1- and 3-min intervals for coatings ***1–5***

Рис. 5. Объем износа образца при абразивном воздействии в течение 1 и 3 мин для покрытий ***1–5***

Tribological tests in the sliding friction mode

Fig. 6 shows the results of tribological testing of coatings in the sliding friction mode during heating from a temperature of 25 °C to 500 °C.

Coating 1 showed a stable coefficient of friction of μ ~0.3 up to $t = 225$ °C. Above this temperature, the value of μ increased to >0.8, which is indicative of coating wear. Sample *2* had an unstable coefficient of friction over the entire temperature range. Over the 25–110 °C range, there was a rapid increase of the μ value from 0.2 to 0.82, which may be associated with the formation of friction wear products. A further decrease in μ to 0.3 is due to the removal of wear products from the tribocontact zone. After a stable interval from 150 to 210 °C, the value of μ gradually increased until it exceeded the 0.8 value at $t = 400$ °C.

Coating 3 with the maximum nitrogen content showed a sharp increase in μ to ~1 at $t = 25 \div 50$ °C. The effect of an increase in the coefficient of friction to values close to 1 may be associated with the exit to the substrate and the friction of the counter body material (Al_2O_3) over the Al_2O_3 substrate, accompanied by adhesive interaction. A similar process was described in detail in [25] in the example of the emergence of a steel-to-steel tribocontact. Sample *4* with the minimum carbon content showed a stable value of μ ~0.3 up to a temperature of 250 °C. In the range $t = 250 \div 350$ °C, an increase in μ to 0.9–1.0 was observed. Coating *5* with the maximum carbon concentration demonstrated the best result, with its coefficient of friction having a stable value of 0.25 up to a temperature of 350 °C. According to the literature data, the Ta–Si–C–N coating is characterised by a high coefficient of friction of 0.6 at $t = 300 \div 400$ °C [26]. Note

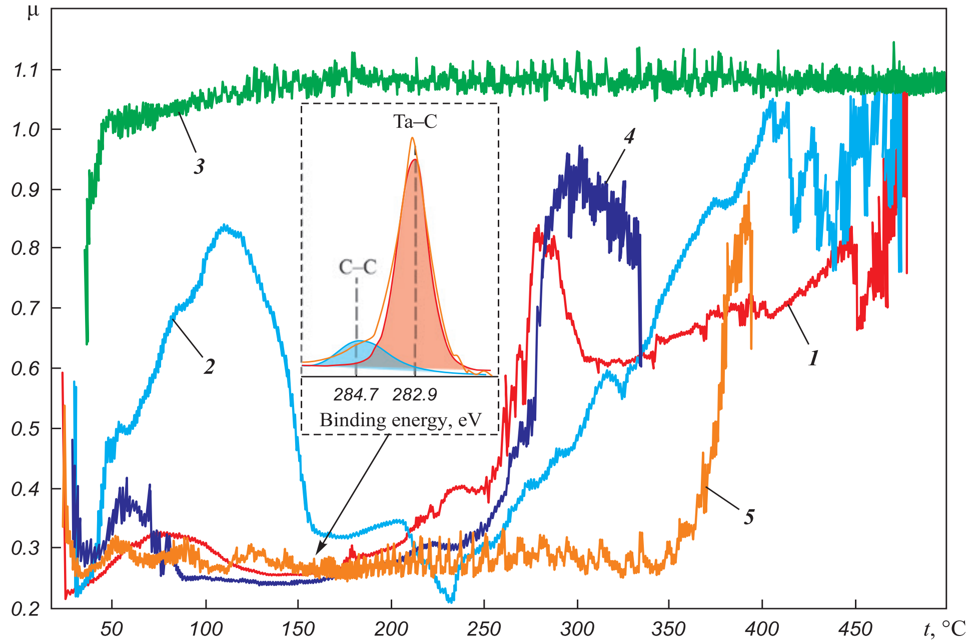

Fig. 6. Dependence of the coefficient of friction on temperature
The inset shows the C1*s* spectrum for coating ***5*** obtained by *X*-ray photoelectron spectroscopy

Рис. 6. Зависимость коэффициента трения от температуры
На вставке представлен спектр C1*s* для покрытия ***5***, полученный методом рентгеновской фотоэлектронной спектроскопии

that the value of μ = 0.25 for sample *5* is half the value obtained earlier for the Ta–Si–C–N coating.

Thus, the coating obtained at a 10 cm^3/min flow rate of C_2H_4 has the minimum coefficient of friction μ = 0.25 and the maximum operating temperature of 350 °C. To determine the reason for the decrease in the coefficient of friction with increasing carbon concentration, coating *5* was studied by *X*-ray photoelectron spectroscopy (see Fig. 6). In the C1*s* spectrum, peaks were observed at a binding energy of 282.9 and 284.4 eV, indicating the presence of Ta–C and C–C bonds, respectively [27; 28]. The reduced coefficient of friction may be associated with the positive role of free carbon, which in some cases can be released during supersaturation of the crystalline carbide phase and acts as a solid lubricant during friction [29]. The influence of the *Me*C carbide phase with a lower coefficient of friction compared to the *Me*N nitride phase also cannot be ruled out [30].

Conclusion

In this work, Ta–Zr–Si–B–C–N system coatings were obtained by magnetron sputtering method using a $TaSi_2$–Ta_3B_4–(Ta, Zr)B_2 target. Ar, as well as Ar + N_2 and Ar + C_2H_4 mixtures, were used as the working gas. The nonreactive Ta–Zr–Si–B coating was characterised by a columnar structure with a crystallite size of the *h*-$TaSi_2$ hexagonal phase of about 11 nm. When N_2 and C_2H_4 were introduced into the working medium, a change in the columnar structure to an equiaxed one with an *h*-$TaSi_2$ grain size of about 3–6 nm was observed. The thickness of the coatings was between 6.0 and 8.1 μm.

Abrasive tests showed that, when exposed for 1–3 min, the sample obtained at the maximum concentration of ethylene has the best abrasive resistance. This effect is associated with the positive role of carbon, which functions as a solid lubricant during friction.

Erosion tests showed that the base sample has the minimum mass change of –0.2 mg. The introduction of nitrogen did not affect the erosion resistance, and the weight loss values for samples *2* and *3* were –0.2 and –0.3 mg, respectively. The introduction of C_2H_4 into the working medium promoted the growth of Δ*m* to 1.1–1.5 mg. No wear was observed on the surface of carbon-containing samples, which indicates their better erosion resistance.

The sliding friction tests showed that coating *1* has a stable coefficient of friction μ = 0.3 up to the maximum working temperature of 225 °C. The introduction of nitrogen led to an increase in the μ values of the coatings up to 0.8–1.0 and a decrease of the maximum operating temperature to 50–110 °C. The coating with the minimum carbon concentration was characterised by a coefficient of friction of ~0.3 up to 250 °C, which is close to the values for the non-reactive coating. Sample *5* containing the maximum content of carbon showed the best result, with its coefficient of friction remaining at the 0.25 level up to a temperature of 350 °C.

References / Список литературы

1. Samsonov G.V., Dvorina L.A., Rud B.M. Silicides. Vol. 1. Moscow: Metallurgiya, 1979. 272 p. (In Russ.).

   Самсонов Г.В., Дворина Л.А., Рудь Б.М. Силициды. Т. 1. М.: Металлургия, 1979. 272 с.
2. Schultes G., Schmitt M., Goettel D., Freitag-Weber O. Strain sensitivity of TiB_2, $TiSi_2$, $TaSi_2$ and WSi_2 thin films as possible candidates for high temperature strain gauges. *Sensors and Actuators A: Physical*. 2006;126(2):287–291. http://doi.org/10.1016/j.sna.2005.05.023
3. Sciti D., Silvestroni L., Celotti G., Melandri C., Guicciardi S. Sintering and mechanical properties of ZrB_2–$TaSi_2$ and HfB_2–$TaSi_2$ ceramic composites. *Journal of the American Ceramic Society*. 2008;91(10):3285–3291. http://doi.org/10.1111/j.1551-2916.2008.02593.x
4. Shon I.J., Ko I.Y., Chae S.M., Na K.I. Rapid consolidation of nanostructured $TaSi_2$ from mechanochemically synthesized powder by high frequency induction heated sintering. *Ceramics International*. 2011;37(2):679–682. https://doi.org/10.1016/j.ceramint.2010.09.054
5. Niu Y., Huang L., Zhai C., Zeng Y., Zheng X., Ding C. Microstructure and thermal stability of $TaSi_2$ coating fabricated by vacuum plasma spray. *Surface and Coatings Technology*. 2015;279:1–8. https://doi.org/10.1016/j.surfcoat.2015.08.025
6. Blanquet E., Vahlas C., Madar R., Palleau J., Torres J., Bernard C. A thermodynamic and experimental approach to $TaSi_2$ chemical vapour deposition. *Thin Solid Films*. 1989;177(1): 189–206. http://doi.org/10.1016/0040-6090(89)90567-1
7. Mansour A.N. Effect of temperature on microstructure and electrical properties of $TaSi_2$ thin films grown on Si substrates. *Vacuum*. 2011;85(6):667–671. https://doi.org/10.1016/j.vacuum.2010.10.003
8. Zhang M., Ren X., Chu H., Lv J., Li W., Wang W., Yang Q., Feng P. Oxidation inhibition behaviors of the HfB_2–SiC–$TaSi_2$ coating for carbon structural materials at 1700 °C. *Corrosion Science*. 2020;177:108982. https://doi.org/10.1016/j.corsci.2020.108982
9. Liu F., Li H., Gu S., Yao X., Fu Q. Ablation behavior and thermal protection performance of $TaSi_2$ coating for SiC coated carbon/carbon composites. *Ceramics International*. 2019;45(3):3256–3262. https://doi.org/10.1016/j.ceramint.2018.10.230
10. Shi X., Zeng X., Li H., Fu Q., Zou J. $TaSi_2$ oxidation protective coating for SiC coated carbon/carbon composites. *Rare Metal Materials and Engineering*. 2011;40(3):403–406. https://doi.org/10.1016/S1875-5372(11)60024-6
11. Monclús M.A., Yang L., López-Cabañas I., Castillo-Rodríguez M., Zaman A., Wang J., Meletis E.I., González-Arrabal R., Llorca J., Molina-Aldareguía J.M. High temperature mechanical properties and microstructure of hard TaSiN coatings. *Materials Science and Engineering: A*. 2020;797:139976. https://doi.org/10.1016/j.msea.2020.139976
12. Mešić B., Schroeder H. Properties of TaSiN thin films deposited by reactive radio frequency magnetron sputtering. *Thin Solid Films*. 2012;520(13):4497–4500. https://doi.org/10.1016/j.tsf.2012.02.068
13. Sytchenko A.D., Levashov E.A., Kiryukhantsev-Korneev P.V. Structure and properties of Ta–Si–N coatings obtained by pulsed magnetron sputtering. *Russian Journal of Non-Ferrous Metals*. 2021;62(5):611–617. https://doi.org/10.3103/S1067821221050151

    Сытченко А.Д., Левашов Е.А., Кирюханцев-Корнеев Ф.В. Структура и свойства покрытий Ta–Si–N, полученных методом импульсного магнетронного распыления. *Известия вузов. Порошковая металлургия и функциональные покрытия*. 2021;15(2):60–67. https://doi.org/10.17073/1997-308X-2021-2-60-67
14. Bondarev A.V., Vorotilo S.A., Shchetinin I.V., Levashov E.A., Shtansky D.V. Fabrication of Ta–Si–C targets and their utilization for deposition of low friction wear resistant nanocomposite Si–Ta–C–(N) coatings intended for wide temperature range tribological applications. *Surface and Coatings Technology*. 2019;359:342–353. https://doi.org/10.1016/j.surfcoat.2018.12.030
15. Ren Y., Qian Y., Xu J., Jiang Y., Zuo J., Li M. Oxidation and cracking/spallation resistance of ZrB_2–SiC–$TaSi_2$–Si coating on siliconized graphite at 1500 °C in air. *Ceramics International*. 2020;46(5):6254–6261. https://doi.org/10.1016/j.ceramint.2019.11.095
16. Kiryukhantsev-Korneev Ph.V., Sytchenko A.D., Vorotilo S.A., Klechkovskaya V.V., Lopatin V.Y., Levashov E.A. Structure, oxidation resistance, mechanical, and tribological properties of N- and C-doped Ta–Zr–Si–B hard protective coatings obtained by reactive D.C. magnetron sputtering of TaZrSiB ceramic cathode. *Coatings*. 2020;10(10):946. https://doi.org/10.3390/coatings10100946
17. Kiryukhantsev-Korneev Ph.V., Sytchenko A.D., Sviridova T.A., Sidorenko D.A., Andreev N.V., Klechkovskaya V.V., Polčak J., Levashov E.A. Effects of doping with Zr and Hf on the structure and properties of Mo–Si–B coatings obtained by magnetron sputtering of composite targets. *Surface and Coatings Technology*. 2022;442:128141. https://doi.org/10.1016/j.surfcoat.2022.128141
18. Kiryukhantsev-Korneev F.V. Possibilities of glow discharge optical emission spectroscopy in the investigation of coatings. *Russian Journal of Non-Ferrous Metals*. 2014;55(5): 494–504. http://doi.org/10.3103/S1067821214050137

    Кирюханцев-Корнеев Ф.В. Возможности метода оптической эмиссионной спектроскопии тлеющего разряда GDOES при исследовании покрытий. *Известия вузов. Порошковая металлургия и функциональные покрытия*. 2013;(2):60–70. https://doi.org/10.17073/1997-308X-2013-2-60-70
19. Kiryukhantsev-Korneev P.V., Phiri J., Gladkov V.I., Ratnikov S.N., Yakovlev M.G., Levashov E.A. Erosion and abrasion resistance, mechanical properties, and structure of the TiN, Ti–Cr–Al–N and Cr–Al–Ti–N coatings deposited by CFUBMS. *Protection of Metals and Physical Chemistry of Surfaces*. 2019;55(5):913–923. https://doi.org/10.1134/S2070205119050125
20. Mirzaei S., Alishahi M., Souček P., Ženíšek J., Holec D., Koutná N., Buršíková V., Stupavská M., Zábranský L., Burmeister F., Blug B., Czigány Zs., Balázsi K., Mikšová R., Vašina P. The effect of chemical composition on the structure, chemistry and mechanical properties of magnetron sputtered W–B–C coatings: *Modeling and Experiments*. *Surface and Coatings Technology*. 2020;383: 125274. https://doi.org/10.1016/j.surfcoat.2019.125274
21. Musil J. Hard nanocomposite coatings: Thermal stability, oxidation resistance and toughness. *Surface and Coatings*

Technology. 2012;207:50–65.
https://doi.org/10.1016/j.surfcoat.2012.05.073

22. Hu J., Li H., Li J., Huang J., Kong J., Zhu H., Xiong D. Structure, mechanical and tribological properties of TaC_x composite films with different graphite powers. *Journal of Alloys and Compounds*. 2020;832:153769.
https://doi.org/10.1016/j.jallcom.2020.153769

23. Nah J.W., Hwang S.K., Lee C.M. Development of a complex heat resistant hard coating based on (Ta, Si)N by reactive sputtering. *Materials Chemistry and Physics*. 2000;62(2): 115–121.https://doi.org/10.1016/S0254-0584(99)00142-X

24. Martínez-Martínez D., López-Cartes C., Justo A., Fernández A., Sánchez-López J.C. Self-lubricating Ti–C–N nanocomposite coatings prepared by double magnetron sputtering. *Solid State Sciences*. 2009;11(3):660–670.
https://doi.org/10.1016/j.solidstatesciences.2008.10.017

25. Kiryukhantsev-Korneev P.V., Pierson J.F., Bychkova M.Y., Manakova O.S., Levashov E.A., Shtansky D.V. Comparative study of sliding, scratching, and impact-loading behavior of hard CrB_2 and Cr–B–N films. *Tribology Letters*. 2016;63(3):44. https://doi.org/10.1007/s11249-016-0729-0

26. Bondarev A.V., Antonyuk M.N., Kiryukhantsev-Korneev Ph.V., Polcar T., Shtansky D.V. Insight into high temperature performance of magnetron sputtered Si–Ta–C–(N) coatings with an ion-implanted interlayer. *Applied Surface Science*. 2021;541:148526.
https://doi.org/10.1016/j.apsusc.2020.148526

27. *XPS Database*. http://www.lasurface.com/database/elementxps.php

28. Vargas M., Castillo H.A., Restrepo-Parra E., De La Cruz W. Stoichiometry behavior of TaN, TaCN and TaC thin films produced by magnetron sputtering. *Applied Surface Science*. 2013;279:7–12.
https://doi.org/10.1016/j.apsusc.2013.03.028

29. Sánchez-López J.C., Martínez-Martínez D., López-Cartes C., Fernández A. Tribological behaviour of titanium carbide/amorphous carbon nanocomposite coatings: From macro to the micro-scale. *Surface and Coatings Technology*. 2008;202(16):4011–4018.
https://doi.org/10.1016/j.surfcoat.2008.02.012

30. González-Hernández A., Morales-Cepeda A.B., Caicedo J.C., Amaya C., Olive-Méndez S.F. Structure, functional groups analysis and tribo-mechanical behavior of carbide and nitride coatings deposited on AISI 1060 substrates by RF-magnetron sputtering. *Journal of Materials Research and Technology*. 2022;18:5432–5443.
https://doi.org/10.1016/j.jmrt.2022.04.075

Information about the Authors

Alina D. Sytchenko – Junior Research Scientist of the “*In situ* Diagnostics of Structural Transformations” Laboratory of Scientific-Educational Center of Self-Propagating High-Temperature Synthesis (SHS), MISIS–ISMAN, National University of Science and Technology (NUST) “MISIS”
ORCID: 0000-0002-8668-5877
E-mail: alina-sytchenko@yandex.ru

Roman A. Vakhrushev – MSc, Laboratory Assistant Researcher of the “*In situ* Diagnostics of Structural Transformations” Laboratory of Scientific-Educational Center of SHS, MISIS–ISMAN
E-mail: romavahaa@gmail.com

Philipp V. Kiryukhantsev-Korneev – Cand. Sci. (Eng.), Associate Professor, Department of Powder Metallurgy and Functional Coatings of NUST “MISIS”; Head of the “*In situ* Diagnostics of Structural Transformations” Laboratory of Scientific-Educational Center of SHS, MISIS–ISMAN
ORCID: 0000-0003-1635-4746
E-mail: kiruhancev-korneev@yandex.ru

Сведения об авторах

Алина Дмитриевна Сытченко – мл. науч. сотрудник лаборатории «*In situ* диагностика структурных превращений» научно-учебного центра (НУЦ) СВС, МИСИС–ИСМАН, Национальный исследовательский технологический университет (НИТУ) «МИСИС»
ORCID: 0000-0002-8668-5877
E-mail: alina-sytchenko@yandex.ru

Роман Алексеевич Вахрушев – магистрант, лаборант-исследователь лаборатории «*In situ* диагностика структурных превращений», НУЦ СВС, МИСИС-ИСМАН
E-mail: romavahaa@gmail.com

Филипп Владимирович Кирюханцев-Корнеев – к.т.н, доцент кафедры порошковой металлургии и функциональных покрытий НИТУ МИСИС; зав. лабораторией «*In situ* диагностика структурных превращений», НУЦ СВС, МИСИС–ИСМАН
ORCID: 0000-0003-1635-4746
E-mail: kiruhancev-korneev@yandex.ru

Contribution of the Authors

A. D. Sytchenko – conducting the calculations, writing the text, testing the samples; analysis of the research results, writing the text, formulation of the conclusions.
R. A. Vakhrushev – testing the samples, writing the text.

Ph. V. Kiryukhantsev-Korneev – formation of the main concept, goal and objectives of the study; scientific guidance, correction of the text and conclusions.

Вклад авторов

А. Д. Сытченко – проведение расчетов, испытаний образцов, анализ результатов исследований, подготовка текста, формулировка выводов.
Р. А. Вахрушев – проведение испытаний образцов, подготовка текста статьи.
Ф. В. Кирюханцев-Корнеев – формирование основной концепции, постановка цели и задачи исследования, научное руководство, корректировка текста, корректировка выводов.

Received 28.06.2022
Revised 01.11.2022
Accepted 08.11.2022

Статья поступила 28.06.2022 г.
Доработана 01.11.2022 г.
Принята к публикации 08.11.2022 г.

Application of Powder Materials and Functional Coatings
Применение порошковых материалов и функциональных покрытий

UDC 621.318.1

https://doi.org/10.17073/1997-308X-2023-2-71-77

Research article
Научная статья

The influence of magnetic fields on the strength of modified epoxy resin composites

M. D. Sosnin, I. A. Shorstkii

Kuban State Technological University
2 Moskovskaya str., Krasnodar 350072, Russia

i-shorstky@mail.ru

Abstract. The aerospace industry is currently undergoing a major trend of transitioning to composites. This study exanines the utilization of the magnetic field of rotating dipoles to produce high-strength iron powder-containing composites. The physical and mechanical properties of the modified epoxy composites were investigated through the use of SEM to analyze their microstructure and elemental composition, and a component distribution map was developed for the samples. Results indicate that the application of the magnetic field of rotating dipoles enhances the compression strength by 16.6 % relative to samples that were not exposed to it. Additionally, the magnetic field eliminates gas porosity and cavities formed during stirring. Tests conducted on composites with a higher content of Al particle showed that the magnetic field of rotating dipoles contributes to the release of excess aluminum as a surface layer. The use of the magnetic field of rotating dipoles is a promising technology for producing enhanced composites with superior physical and mechanical properties, which could potentially be used as structural material in aerospace industry or as adsorbing materials in microelectronics.

Keywords: epoxy composite, magnetic field of rotating dipoles (MFRD), compressive strength, filler, iron powder, microstructure

Acknowledgements: This study is supported by the Kuban Research Foundation as part of the research and innovation project commercialization contest No. NIP-20.1/23.

For citation: Sosnin M.D., Shorstkii I.A. The influence of magnetic fields on the strength of modified epoxy resin composites. *Powder Metallurgy and Functional Coatings*. 2023;17(2):71–77. https://doi.org/10.17073/1997-308X-2023-2-71-77

Исследование влияния магнитных воздействий на прочностные характеристики модифицированных эпоксидных композиционных материалов

М. Д. Соснин, И. А. Шорсткий

Кубанский государственный технологический университет
350072, г. Краснодар, ул. Московская, 2

i-shorstky@mail.ru

Аннотация. Замена традиционных материалов композиционными представляет собой важный вектор развития авиационной и аэрокосмической отраслей промышленности. В работе рассмотрены вопросы применения магнитного поля вращающихся диполей с целью получения композиционных материалов на основе порошкового железа с высокими прочностными и структурными характеристиками. Исследованы физико-механические свойства модифицированных эпоксидных композиционных материалов. С помощью средств электронной микроскопии исследованы микроструктура, элементный состав и получена карта распределения компонентов в получаемых образцах. Экспериментальным путем выявлено, что при наложении магнитного поля вращающихся диполей прочность при сжатии композитов увеличивается на 16,6 % относительно образцов, полученных без применения этой технологии. Это вызвано тем, что данный метод позволяет удалять возникающую в процессе механосинтеза газовую пористость и раковины во внутренней структуре материала. Серия экспериментов с добавлением увеличенного массового соотношения Al-частиц показала, что магнитное поле вращающихся диполей способствует вытеснению излишков алюминия в виде поверхностного слоя. Таким образом, можно заключить, что применение магнитного поля вращающихся диполей является перспективным направлением в области создания композиционных материалов с улучшенными физико-механическими характеристиками. Получаемые эпоксидные композиты могут быть использованы в качестве конструкционных материалов в авиационной и космической отраслях, а также в качестве материалов адсорберов в радиотехнической аппаратуре и микроэлектронике.

Ключевые слова: эпоксидный композиционный материал, магнитное поле вращающихся диполей (МПВД), прочность на сжатие, наполнитель, порошковое железо, микроструктура

Благодарности: Работа выполнена при финансовой поддержке Кубанского научного фонда в рамках конкурса научно-инновационных проектов, ориентированных на коммерциализацию № НИП-20.1/23.

Для цитирования: Соснин М.Д., Шорсткий И.А. Исследование влияния магнитных воздействий на прочностные характеристики модифицированных эпоксидных композиционных материалов. *Известия вузов. Порошковая металлургия и функциональные покрытия*. 2023;17(2):71–77. https://doi.org/10.17073/1997-308X-2023-2-71-77

Introduction

The demand for composite materials filled with powders has been increasing steadily every year, as evidenced global statistics on the polymer market. For example, in 2020, the volum of the global polymer composite market was approximately 13 mln tons [1].

In Russia, the Technet roadmap has been implemented to facilitate the development of advanced manufacturing technologies and composites [2]. The roadmap has identified controlled microstructure composites as one of the key future technologies to be explored.

Thermoplastic polymers and epoxy resins are frequently used as matrices in the production of filler powder-based composites [3]. The composites incorporating thermoplastic polymers are known for their broad mechanical properties and wide-ranging applications [4; 5]. However, it is essential to note that the physical and mechanical characteristics of these composites are not always consistent and may vary.

The incorporation of reinforcing fillers in such composites has been found to enhance the adhesive bond [6; 7] and strength [8]. The dispersion structure of these composites significantly contributes to their strength, primarily through the formation of structured layers [9], filler cluster-aggregation [10], and crystallization [11].

Starokadomsky D. et al. [12] demonstrated the potential for enhancing the strength and durability of epoxy composites by incorporating silicon carbide and titanium nitride fillers. The introduction of these fillers resulted in a significant increase in microhardness (150–200 %) and compressive strength (by 9 %).

Recently, electrophysical methods have been employed to enhance the physical and mechanical characteristics of composites. These methods involve exposing composites to a strong static magnetic field [13; 14], magnetic pulses [15], and the magnetic field of rotating dipoles (MFRD) [16]. MFRD is an efficient technique for regulating the packing structure of powders in composites without requiring significant energy input.

The aim of this study is to investigate the impact of the magnetic field of rotating dipoles on the strength and other structural characteristics of composites containing iron and aluminum powder.

Research methods

Materials

In our study, we examined two types of particles, namely iron microparticles PZHV1.160.26 (GOST 9849-86) and aluminum powder PAP-2 (GOST 5494-95). The matrix used was composed of a mixture of ED-20 dian resin (GOST 10587-84) and polyethylene polyamine (PEPA) in a 5:1 ratio.

Composite manufacturing

Figure 1 illustrates the patented process used to create the modified epoxy composite samples in our study. The experiment involved two types of fillers: powdered iron, and a mixture of powdered iron and Al-particles in a 7:3 weight ratio. The ED-20 resin-based composite was mixed with the powder filler, which contained 70 wt. %. PZHV1.160.26 iron microparticles and 30 wt. %. PAP-2 aluminum powder, in a polymer cylinder with a 20 mm ID. The hardener, PEPA, was then added to the mixture in a quantity equal to 1/5 of the weight of the resin. The resulting compositions were heat treated at a temperature of 90 °C for 1–2 min to eliminate gas porosity, and then poured into molds. Finally, the samples were removed from the molds for analysis.

We fabricated four composite samples with identical dimensions of 20 mm in diameter and 20 mm in length. Among these samples, two were composed of Fe–Al (FAM) and Fe (FM) microparticles and were exposed to the magnetic field generated by rotating dipoles (Figure 2). The induction level of the magnetic field was set to 0.5–0.7 Tesla [17; 18]. The remaining two samples served as refrence samples and were not exposed to the magnetic field.

Strength measurements

We used an IP-100M automatic hydraulic press to apply static loads to the composite samples for both compression and bending tests.

The loading rate was set to 1 mm/min. We then plotted an experimental load-compressive strain curve to estimated the compressive failure stress and relative strain of the samples. To obtain precise measurements, we recorded the compression process at a high frame rate.

The compressive failure stress (σ, MPa) was determined as

$$\sigma = F/A,$$

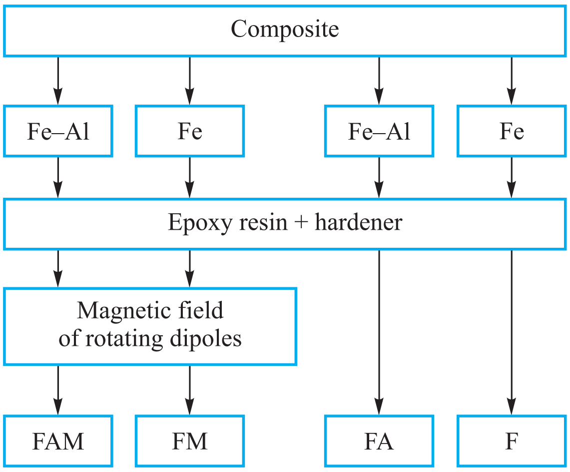

Fig. 1. Composite exposure to the magnetic field of rotating dipoles
FAM – Fe–Al (MFRD); **FM** – Fe (MFRD);
FA – Fe–Al (no MFRD); **F** – Fe (no MFRD)

Рис. 1. Блок-схема получения модифицированных эпоксидных композиционных материалов
FAM – Fe–Al (МПВД); **FM** – Fe (МПВД);
FA – Fe–Al (без МПВД); **F** – Fe (без МПВД)

where F is the max compressive strength, N; A is the cross-section area of the sample, mm^2.

The relative compressive strain at failure was estimated as

$$\varepsilon = \frac{\Delta h}{h_0} \cdot 100\ \%,$$

where Δh is the relative strain, mm; h_0 is the initial sample height, mm.

During the test, we closely monitored the samples being tested. After the tests, each sample was photographed for damage analysis.

To examine the microstructure, elemental composition, and component distribution in the composite samples, we employed an EVO HD 15 scanning electron microscope (Carl Zeiss, UK/Germany) in low vacuum (EP, 70 Pa), 20–25 kV.

Results and discussion

Strength properties

We generated experimental load-strain curves for the compocite samples (Figure 3). As the powder-filled composite samples were compressed, the majority of the load was applied to the matrix, which was followed by a sharply decrease in load after matrix destruction. The load-strain curves for the cylindrical samples (Fig. 3) indicate that the volume deformation of composites causes softening, which is more significant for the samples made without MFRD.

The experimental compressive failure stress values are summarized in the table. The composite sample with the Fe–Al filler exposed to MFRD exhibited the highest compressive failure stress value of 57.5 MPa, indicating its superior strength compared to the othe composite samples.

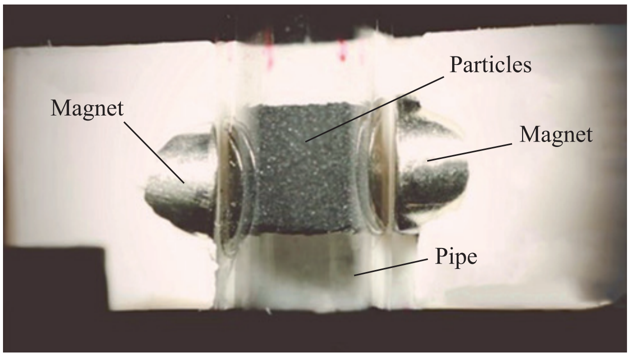

Fig. 2. Modified epoxy resin composite manufacturing process

Рис. 2. Схема воздействия магнитного поля вращающихся диполей на материал

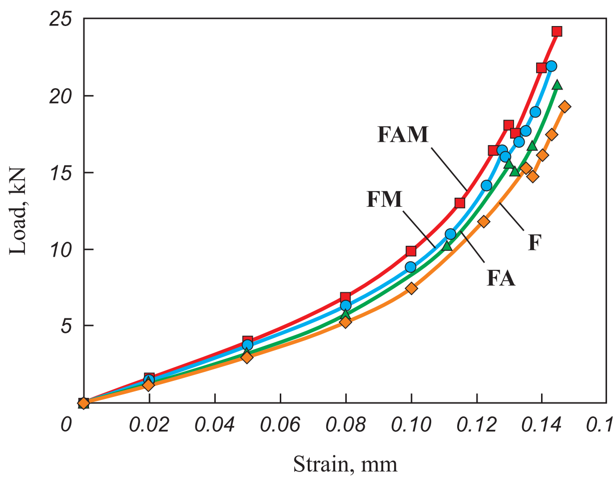

Fig. 3. Strain curves for the composites
FAM – Fe–Al (MFRD); **FM** – Fe (MFRD);
FA – Fe–Al (no MFRD); **F** – Fe (no MFRD)

Рис. 3. Кривые деформирования композиционных материалов, полученных по разным технологиям
FAM – Fe–Al (МПВД); **FM** – Fe (МПВД);
FA – Fe–Al (без МПВД); **F** – Fe (без МПВД)

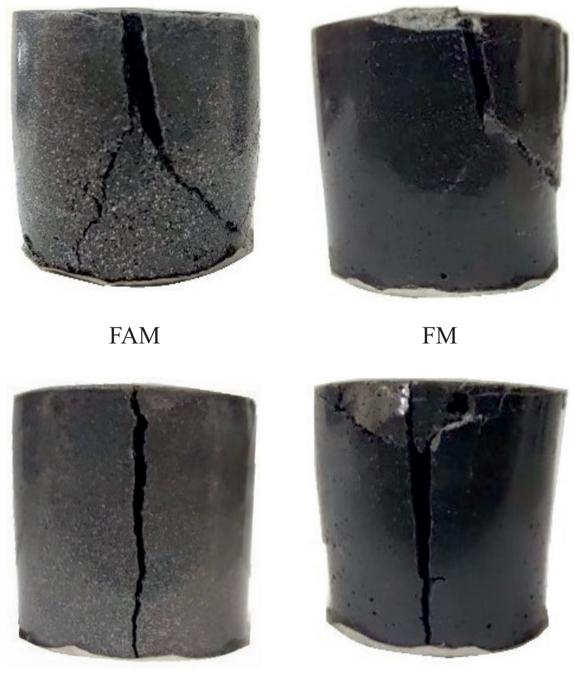
FAM FM
FA F

Fig. 4. Samples after the compression test
FAM – Fe–Al (MFRD); **FM** – Fe (MFRD);
FA – Fe–Al (no MFRD); **F** – Fe (no MFRD)

Рис. 4. Фотографии образцов после испытания на сжатие
FAM – Fe–Al (МПВД); **FM** – Fe (МПВД);
FA – Fe–Al (без МПВД); **F** – Fe (без МПВД)

A comparison was made between the mechanical properties of composites that were exposed and not exposed to MFRD. The results showed that the samples exposed to MFRD were able to withstand a greater load due to a denser and structured distribution of particles in the epoxy matrix [19].

The composite strength of the the Fe–Al filler exposed to MFRD was found to be 30 % higher (57.5 MPa) compared to that of the sample containing only epoxy resin (44 MPa). Additionally, the hardness of the samples was increased by 16.6 % due to the effect of MFRD.

Several researchers have noted the reinforcing effect of incorporating a dispersed system into a polymer matrix [20]. For example, the addition of micro silicon has ben shown to improve strength by 10–15 % [21]. The inclusion of silicon nanoparticles has been found to increase the compressive strength of epoxy composites by 30 % [22].

Visual inspection of the samples after compression revealed brittle fracture in both cases (Figure 4). However, the samples exposed to MFRD showed cracks along the sloped planes, whereas the samples not exposed to MFRD had cracks along the straight planes. This difference is likely due to the packing of particles in the polymer matrix, which is supported by the difference in the composite densities (see table).

Microscopic examination and component distribution maps in the composite samples

Figure 5 displays cross-sections of the composites exposed and not exposed to MFRD. The notable difference is the presence of air cavities in the sample made without MFRD.

Compressive mechanical properties of the composites

Механические свойства при сжатии композиционных материалов различного типа

Composite	ρ, g/cm^3	F_{max}, kN	σ, MPa	ε, %
FAM (Fe–Al + MFRD)	2.79	18.06	57.5	0.650
FM (Fe + MFRD)	2.86	16.39	52.2	0.635
FA (Fe–Al no MFRD)	2.72	15.48	49.3	0.650
F (Fe no MFRD)	2.64	15.26	48.6	0.675
Epoxy resin	1.20	13.80	44.0	0.800

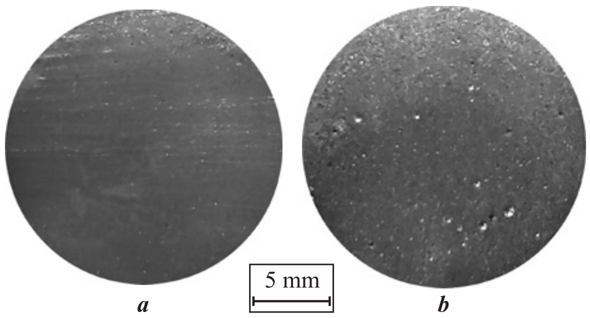

Fig. 5. Surface structure of the FAM (***a***) and FA (***b***) composites

Рис. 5. Структура поверхности композиционных материалов FAM (***а***) и FA (***b***)

To assess the homogeneity of the particle distribution in the composite, component distribution maps for the FA and FAM samples was produced (Figure 6). The results demonstrate that the magnetic field of rotating dipoles produces a more uniform distribution without particle agglomeration.

Conclusion

We tested the compressive strength of cylindrical samples made of epoxy composites containing Fe–Al and Fe particles. It was discovered that the Al-containing sample exposed to MFRD exhibited the highest strength being 14 % greater than that of the sample not exposed to MFRD. The elimination of gas porosity and cavities during the stirring by magnetic degassing is the reason for this phenomenon.

Such composites can be used as structural material in aerospace, or as adsorbing materials in microelectronics.

References / Список литературы

1. Doriomedov M.S. Russian and world market of polymer composites (review). *Trudy VIAM*. 2020;6-7(89):29–37. (In Russ.).
https://doi.org/10.18577/2307-6046-2020-0-67-29-37

   Дориомедов М.С. Российский и мировой рынок полимерных композитов (обзор). *Труды ВИАМ*. 2020;6-7(89):29–37.
https://doi.org/10.18577/2307-6046-2020-0-67-29-37

2. National technology initiative (NTI). URL: http://fea.ru/compound/national-technology-initiative (accessed: 01.04.2022 г.). (In Russ.).

   Национальная технологическая инициатива (НТИ). URL: http://fea.ru/compound/national-technology-initiative (дата обращения: 01.04.2022 г.).

3. Alentyev A.Yu., Yablokova M.Yu. Binders for polymer composite materials. Moscow: Lomonosov MGU, 2010. 69 p. (In Russ.).

   Алентьев А.Ю., Яблокова М.Ю. Связующие для полимерных композиционных материалов. М.: МГУ им. М.В. Ломоносова, 2010. 69 с.

4. Timofeenko AA., Timoshenko V.V. Influence of mixtures of thermoplastic polymer waste on the physical and mechanical characteristics of polymer-mineral compositions. In: *Materials of the V Republican scientific and technical conference of young scientists “New functional materials, modern technologies and research methods”* (Gomel’, 12–14.11.2018). Gomel’: Institut mekhaniki metallopolimernykh sistem imeni V.A. Belogo, NAn Belarusi. 2018. P. 30–31. (In Russ.).

   Тимофеенко А.А., Тимошенко В.В. Влияние смесей термопластичных полимерных отходов на физико-механические характеристики полимер-минеральных композиций. В сб.: *Материалы V Республиканской научно-технической конференции молодых ученых*

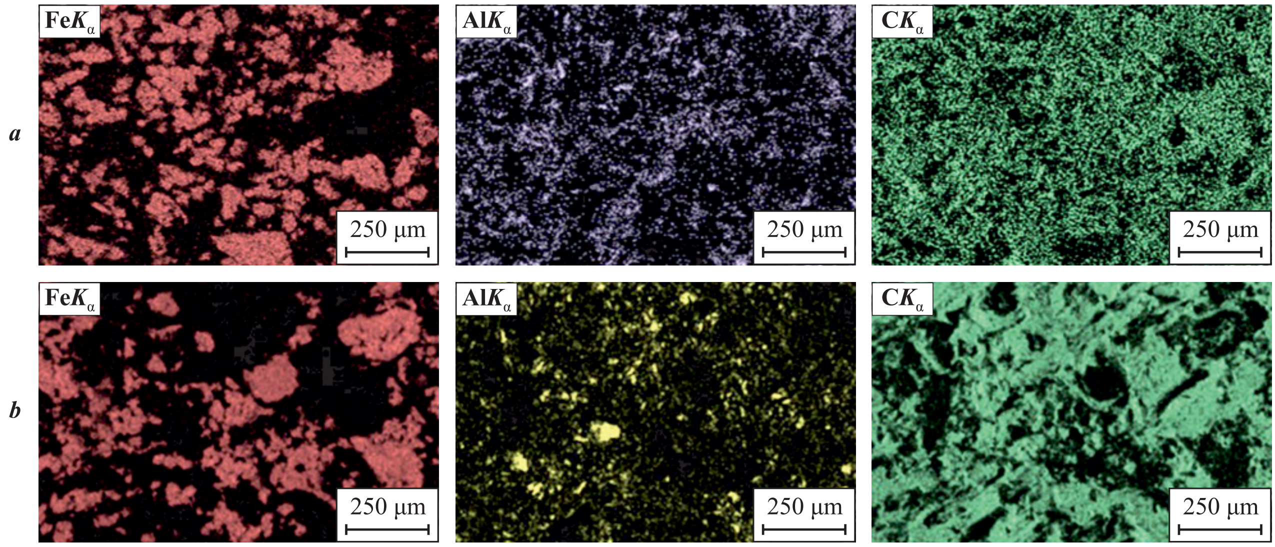

Fig. 6. Fe, Al, and C distribution maps for the FAM (***a***) and FA (***b***) samples composites

Рис. 6. Карты распределения Fe, Al и C в композиционных материалах FAM (***а***) и FA (***б***)

«Новые функциональные материалы, современные технологии и методы исследования» (г. Гомель, 12–14 ноября 2018 г.). Гомель: Институт механики металлополимерных систем им. В.А. Белого, НАН Беларуси, 2018. С. 30–31.

5. Kondratyev D.N.. Zhuravskiy V.G. The use of nanostructured materials to increase the reliability of REA. *Nanoindustriya*. 2008;4:14–18. (In Russ.).

Кондратьев Д.Н., Журавский В.Г. Использование наноструктурных материалов для повышения надежности РЭА. *Наноиндустрия*. 2008;4:14–18.

6. Panin S.V., Kornienko L.A., Alexenko V.O., Nguyen Duc Anh, Ivanova L.R. Influence of nanofibers/nanotubes on physical-mechanical and tribotechnical properties of polymer composites based on thermoplastic UHMWPE and PEEK matrixes. *Izvestiya vysshih uchebnyh zavedenij. Seriya: Khimiya i khimicheskaya tekhnologiya*. 2017;60(9):45–51. (In Russ.).

https://doi.org/10.6060/tcct.2017609.7y

Панин С.В., Корниенко Л.А., Алексенко В.О., Нгуен Дык Ань, Иванова Л.Р. Влияние углеродных нановолокон/нанотрубок на формирование физико-механических и триботехнических характеристик полимерных композитов на основе термопластичных матриц СВМПЭ и ПЭЭК. *Известия высших учебных заведений. Серия: Химия и химическая технология*. 2017;60(9): 45–51. https://doi.org/10.6060/tcct.2017609.7y

7. Ozolin A.V., Sokolov E.G., Golius D.A. Obtaining of tungsten nanopowders by high energy ball milling. *IOP Conference Series: Materials Science and Engineering*. 2020;862(2):022057.
https://doi.org/10.1088/1757-899X/862/2/022057

8. Nelyub V.A. Quantitative assessment of the adhesive interaction of carbon fiber and epoxy binder. *Izvestiya vuzov. Aviacionnaya tekhnika*. 2016;2:97–100. (In Russ.).

Нелюб В.А. Количественная оценка адгезионного взаимодействия углеродного волокна и эпоксидного связующего. *Известия вузов. Авиационная техника*. 2016;(2):97–100.

9. Lipatov Yu.S. Physico-chemistry of filled polymers. Kyiv: Naukova Dumka, 1991. 256 p. (In Russ.).

Липатов Ю.С. Физико-химия наполненных полимеров. Киев: Наук. Думка, 1991. 256 с.

10. Starokadomsky D.L. Some features of swelling of photopolymer composites with different content of highly dispersed silica. *Plasticheskie massy*. 2008;(2):33–36. (In Russ.).

Старокадомский Д.Л. Некоторые особенности набухания фотополимерных композитов с различным содержанием высокодисперсного кремнезёма. *Пластические массы*. 2008;2:33–36.

11. Emelina O.Yu. Composite polymer materials modified with dispersed fillers used in construction and repair of machinery. *Vestnik Kazanskogo tehnologicheskogo universiteta*. 2014;17(3):128–130. (In Russ.).

Емелина О.Ю. Композиционные полимерные материалы, модифицированные дисперсными наполнителями, применяемые в строительстве и при ремонте техники. *Вестник Казанского технологического университета*. 2014;17(3):128–130.

12. Starokadomsky D., Golovan S., Sigareva N., Tkachenko O., Moshkovska N., Kokhtych L., Garashchenko I. Possibilities of enhancement of the strength and durability of epoxy composites by silicon carbide and titanium nitride filling. *Science Rise*. 2019;4:55–59. (In Russ.). https://doi.org/10.15587/2313-8416.2019.164289

Старокадомский Д.Л., Головань С.В., Сигарѐва Н.В., Ткаченко А.А., Мошковская Н.М., Кохтич Л.М., Гаращенко И.И. Возможности усиления прочности и стойкости эпокси-композитов путём наполнения карбидом кремния и нитридом титана. *Science Rise*. 2019;4:55–59. https://doi.org/10.15587/2313-8416.2019.164289

13. Milyutin V.A., Gervasyeva I.V. Thermally activated transformations in alloys with different type of magnetic ordering under high magnetic field. *Journal of Magnetism and Magnetic Materials*. 2019;492:165654.
https://doi.org/10.1016/j.jmmm.2019.165654

14. Zuo X., Zhang L., Wang E. Influence of external static magnetic fields on properties of metallic functional materials. *Crystals*. 2017;7(12):374.
https://doi.org/10.3390/cryst7120374

15. Zhao J., Yu J.H., Han K., Zhong H.G., Li R.X., Zhai Q.J. Effect of coil configuration design on Al solidified structure refinement. *Metals*. 2020;10(1):153.
https://doi.org/10.3390/met10010153

16. Shorstkii I.A., Yakovlev N. Method of absorbing material formation based on magnetically controlled particles of Fe_3O_4. *Inorganic Materials: Applied Research*. 2020;11(5):1236–1243.
https://doi.org/10.1134/S2075113320050317

Шорсткий И.А., Яковлев Н. Метод формирования материала-поглотителя электромагнитного излучения на основе магнитоуправляемых частиц Fe_3O_4. *Перспективные материалы*. 2020;3:70–79.

17. Shorstkii I.A., Sosnin M.D. Method of cladding of powdered magnetic material: Patent 2760847 (RF). 2021. (In Russ.).

Шорсткий И.А., Соснин М.Д. Способ плакирования порошкового магнитного материала: Патент 2760847 (РФ). 2021.

18. Shorstkii I. Dynamic arrays based on magnetically controlled particles: Synthesis and application. *Materials Research*. 2019;22(4):e20180317.
http://doi.org/10.1590/1980-5373-mr-2018-0317

19. Deng S., Ye L., Friedrich K. Fracture behaviours of epoxy nanocomposites with nano-silica at low and elevated temperatures. *Journal of Materials Science*. 2007;42(8): 2766–2774. https://doi.org/10.1007/s10853-006-1420-x

20. Gorbacheva S.N., Gorbunova I.Y., Kerber M.L., Antonov S.V. The properties of composite polymeric materials based on epoxy resins, modified with boron nitride. *Uspekhi v khimii i khimicheskoj tekhnologii*. 2017;31(11)(192):35–36. (In Russ.).

Горбачева С.Н., Горбунова И.Ю., Кербер М.Л., Антонов С.В. Свойства композиционных полимерных материалов на основе эпоксидной смолы, модифицированных нитридом бора. *Успехи в химии и химической технологии*. 2017;31(11(192)):35–36.

21. Chow T.S. Size-dependent adhesion of nanoparticles on rough substrates. *Journal of Physics: Condensed Matter*. 2003;15(2):L83. http://doi.org/10.1088/0953-8984/15/2/111

22. Vaganova T.A. Synthesis and characterization of epoxy-anhydride polymers modified by polyfluoroaromatic oligoimides. *Journal of Polymer Research*. 2014;21(11):588. http://doi.org/10.1007/s10965-014-0588-z

Information about the Authors

Maxim D. Sosnin – Graduate Student of the Department of Technological Equipment and Life-Support Systems, Kuban State Technological University (KubSTU)
ORCID: 0000-0001-6275-6274
E-mail: maksim-sosnin7@mail.ru

Ivan A. Shorstkii – Cand. Sci. (Eng.), Associate Professor of the Department of Technological Equipment and Life-Support Systems, KubSTU
ORCID: 0000-0001-5804-7950
E-mail: i-shorstky@mail.ru

Contribution of the Authors

M. D. Sosnin – formation of the main concept, goal and objectives of the study; writing the text, conducting the calculations, testing the samples, formulation of the conclusions.
I. A. Shorstkii – provision of the resources, preparation and management of the experiments, conducting the experiments, formation of the main concept, goal and objectives of the study; writing the text, formulation of the conclusions.

Received 05.05.2022
Revised 27.10.2022
Accepted 31.10.2022

Сведения об авторах

Максим Дмитриевич Соснин – аспирант кафедры технологического оборудования и систем жизнеобеспечения, Кубанский государственный технологический университет (КубГТУ)
ORCID: 0000-0001-6275-6274
E-mail: maksim-sosnin7@mail.ru

Иван Александрович Шорсткий – к.т.н., доцент кафедры технологического оборудования и систем жизнеобеспечения, КубГТУ
ORCID: 0000-0001-5804-7950
E-mail: i-shorstky@mail.ru

Вклад авторов

М. Д. Соснин – формирование основной концепции, постановка цели и задачи исследования, подготовка текста, проведение расчетов, испытаний образцов, формулировка выводов.
И. А. Шорсткий – обеспечение ресурсами, подготовка эксперимента, проведение экспериментов, формирование основной концепции, постановка цели и задачи исследования, подготовка текста, формулировка выводов.

Статья поступила 05.05.2022 г.
Доработана 27.10.2022 г.
Принята к публикации 31.10.2022 г.

Зарегистрирован Федеральной службой по надзору
в сфере связи, информационных технологий
и массовых коммуникаций.
Свидетельство о регистрации **ПИ № ФС77-79230**

Журнал распространяется агентством «Урал-Пресс»
Подписной индекс: 80752 (печатная версия)
05108 (электронная версия)